



Search for Galactic and Extra-Galactic Neutrino Emission with IceCube

Kai Michael Krings

Vollständiger Abdruck der von der Fakultät für Physik der Technischen Universität München zur Erlangung des akademischen Grades eines

Doktors der Naturwissenschaften (Dr. rer. nat.)

genehmigten Dissertation.

Vorsitzender:

Prof. Dr. Alejandro Ibarra

Prüfende der Dissertation:

1. Prof. Dr. Elisa Resconi
2. Priv.-Doz. Dr. Jochen Greiner

Die Dissertation wurde am 27.03.2018 bei der Technischen Universität München eingereicht und durch die Fakultät für Physik am 16.04.2018 angenommen.

Abstract

Two analyses with the IceCube Neutrino Telescope are presented. A search for cosmic-ray induced neutrino emission in the Galactic plane is performed. The sensitivity of this analysis for the KRA_γ model is about a factor two better than the one of the latest published IceCube analysis. Furthermore, a search for muon neutrinos from the direction of the extra-galactic object 1ES 1959+650 is presented. The source was very active in gamma rays in spring 2016. No evidence for neutrino emission is found.

Zusammenfassung

Zwei Analysen mit dem IceCube-Neutrinooteleskop werden präsentiert. Eine Suche nach durch kosmische Strahlen induzierte Neutrinoemission in der Galaktischen Ebene wurde durchgeführt. Die Sensitivität dieser Analyse für das KRA_γ -Model ist ungefähr um einen Faktor zwei besser als die der neusten veröffentlichten IceCube-Analyse. Desweiteren wird eine Suche nach Myonenneutrinos aus der Richtung des extragalaktischen Objekts 1ES 1959+650 präsentiert. Die Quelle wies eine erhöhte Aktivität in Gammastrahlung im Frühling 2016 auf. Kein Hinweis auf Neutrinoemission wurde gefunden.

Contents

Abstract	iii
List of Figures	vii
List of Tables	ix
1 Introduction	1
2 Leptons from the Atmosphere at TeV Energies	5
2.1 Cosmic Rays	5
2.2 Production of Mesons in Cosmic-Ray Air Showers	10
2.3 Atmospheric Leptons from Meson Decays	14
3 Extra-Terrestrial Neutrinos above TeV Energies	19
3.1 Current Interpretation of the IceCube Neutrino Flux	19
3.2 Cosmic-Ray Induced Neutrinos from the Galaxy	22
3.3 Extra-Galactic Source Candidate 1ES 1959+650	27
4 The IceCube Neutrino Observatory	31
4.1 In-Ice Neutrino Detection	32
4.2 Event Topologies	36
4.3 Data Acquisition, Processing, and Filtering	38
4.4 Calibration	41
5 Event Reconstructions	43
5.1 First-Guess Algorithms	43
5.2 Directional Reconstructions	44
5.3 Energy Reconstructions	47
5.4 Gulliver Framework	49
6 Event Selections	51
6.1 Medium-Energy Starting Events	51
6.1.1 Clean-Up Cuts	53
6.1.2 Outer-Layer Veto	53

6.1.3	Inner Track Veto	54
6.1.4	Fiducial Volume Scaling	55
6.1.5	Event Topology Discrimination	56
6.2	Through-Going Muon Tracks	57
6.2.1	Muon Level 3	57
6.2.2	Neutrino Level Selection	59
6.3	Vetoing Atmospheric Neutrinos	60
6.3.1	Correlated Atmospheric Neutrino Self-Veto	60
6.3.2	Uncorrelated Atmospheric Neutrino Self-Veto	61
7	Search for Neutrino Emission in the Galactic Plane	63
7.1	Fit Method	63
7.1.1	Lepton Flux Templates	65
7.1.2	Re-Sampling in Right Ascension	69
7.1.3	Fit Parameters	69
7.2	Likelihood-Ratio Test	73
7.3	Sensitivity and Discovery Potential	73
7.4	Additional Tests based on the Goodness-of-Fit	80
7.5	Unblinding Status	82
8	Search for Neutrino Emission from 1ES 1959+650	87
8.1	Analysis Method	87
8.2	Angular Uncertainty Estimation	89
8.3	Sensitivity and Discovery Potential	91
8.4	Unblinding Results	94
9	Conclusion	97
	Acknowledgments	99
	A Expected Number of Events	101
	B POCAM Simulation	103
	Glossary	107
	Bibliography	113

List of Figures

2.1	Cosmic-ray proton and all-particle energy spectra	6
2.2	Cosmic-ray elemental energy spectra	8
2.3	H3a and H4a models	9
2.4	Cosmic-ray air shower	11
2.5	Slant depth	12
2.6	Atmospheric lepton fluxes versus energy	16
2.7	Atmospheric neutrino fluxes versus cosine zenith angle	17
2.8	Uncertainties in atmospheric neutrino fluxes	18
3.1	Astrophysical neutrino flux measurements with IceCube	20
3.2	IceCube energy and sine declination distribution	21
3.3	Galactic neutrino flux in Galactic coordinates	25
3.4	Galactic neutrino flux versus energy	27
3.5	Spectral energy distribution of 1ES 1959+650	28
3.6	Flaring phase of 1ES 1959+650 in spring 2016	29
4.1	IceCube Neutrino Observatory	31
4.2	Neutrino cross sections	33
4.3	Cherenkov effect	34
4.4	Optical properties of South Pole ice	35
4.5	Event topologies	37
4.6	Trigger rate	39
5.1	Time residual	45
5.2	Median angular resolution	46
5.3	Median energy resolution	48
5.4	Gulliver components	49
6.1	Neutrino effective area of MESE selection	52
6.2	MESE outer-layer veto	54
6.3	MESE fiducial volume scaling	56
6.4	Neutrino effective area of through-going muon track selection	59
6.5	Atmospheric neutrino self-veto	60

6.6	Passing fraction of atmospheric neutrino self-veto	62
7.1	Energy distributions of lepton flux templates	67
7.2	Arrival direction distributions of lepton flux templates	68
7.3	Fit parameter primary cosmic-ray spectral index	70
7.4	Fit parameter kaon fraction	71
7.5	Fit parameter hole ice model	72
7.6	Test statistic distribution	74
7.7	Sensitivity and discovery potential	75
7.8	Effect of hole ice	76
7.9	Comparison to published IceCube results	77
7.10	Test statistic distribution along analysis bins	78
7.11	Asimov sensitivity and discovery potential	79
7.12	Expected correlation between fit parameters	81
7.13	Expected data/MC agreement under the null-hypothesis	83
7.14	Unblinding status, open questions	85
8.1	Spatial PDF and energy weighting	88
8.2	Pull correction	91
8.3	Test statistic distribution	92
8.4	Sensitivity and discovery potential	93
8.5	Comparison to other follow-up analyses	95
8.6	Unblinding results	96
B.1	POCAM light emission	105

List of Tables

6.1	MESE event topology discrimination efficiency	57
7.1	Lepton flux templates	64
7.2	Sensitivity and discovery potential	75
8.1	Sensitivity and discovery potential	94
A.1	Expected number of events for the H2 model	102
A.2	Expected number of events for the H3 model	102
B.1	POCAM configurations	104

1 Introduction

With the discovery of the first high-energy neutrinos of extra-terrestrial origin with the IceCube Neutrino Telescope, a new window to the Universe was opened. The main questions are: at which sites in the Universe are they produced; and do they tell us something about the origin of cosmic rays?

One would expect to measure a growing deviation from isotropy in the arrival direction of astrophysical neutrinos with increasing statistics, before distinct neutrino sources start to emerge. One of the most promising reasons for such an anisotropy is the Galaxy. It is already known that cosmic rays interact with the gas contained in the interstellar medium and produce neutral pions that decay into gamma rays, which are subsequently detected by gamma-ray telescopes. Consequently, there should also be charged pions that decay into neutrinos. This diffuse neutrino flux is often referred to in the literature as the *guaranteed* neutrino flux of Galactic origin [1]. On the other hand, there was a consensus that this neutrino flux is probably too small to be detected by existing neutrino telescopes, which are mostly sensitive above TeV energies. However, new charged cosmic-ray and gamma-ray data and new developments in the models of cosmic-ray propagation suggest that the diffuse neutrino emission could be much stronger than previously expected, especially in the inner Galaxy [2].

In this thesis, two analyses used to search for Galactic and extra-galactic neutrino emission with the IceCube neutrino detector are presented. The first analysis is a binned forward-folding likelihood fit using templates. It tries to answer the question if the astrophysical neutrino flux measured by IceCube is partly of Galactic origin. It searches for cosmic-ray induced neutrino emission in the Galactic plane with seven years of all-sky all-favors neutrino events that interact inside the detector. The second analysis searches for neutrino emission from the extra-galactic neutrino source candidate 1ES 1959+650,

while the source showed strongly increased activity in gamma rays in spring 2016, which lasted for about three months. For this analysis, neutrino-induced muons are used, which pass the entire detector volume. In the following, the structure of this thesis is outlined.

Chapter 2 In this chapter, the main backgrounds for the search of neutrinos of extra-terrestrial origin are introduced. These are neutrinos and muons produced in particle showers evolving in the Earth's atmosphere. Such air showers are induced by cosmic rays interacting with the nucleons of the Earth's atmosphere.

Chapter 3 This chapter is dedicated to neutrinos of extra-terrestrial origin with energies above 1 TeV. The latest IceCube measurements and interpretations of the astrophysical neutrino flux are presented. Moreover, cosmic-ray propagation in the Galaxy is briefly discussed in the context of cosmic-ray induced neutrino emission in the Galactic plane, and the Galactic neutrino flux models are introduced that are used in this thesis. The last part of this chapter focuses on the extra-galactic neutrino point source candidate 1ES 1959+650.

Chapter 4 In this chapter, the IceCube Neutrino Telescope is introduced. It is explained how neutrino detection in the deep ice at the Geographic South Pole works; how data is acquired, processed, and transferred from the South Pole; and how the detector is calibrated.

Chapter 5 In this chapter, it is explained how the events' direction and energy are reconstructed. Furthermore, the software framework for reconstructions in IceCube is presented and the author's work inside the software group is emphasized.

Chapter 6 In this chapter, the selections of neutrino events with interaction vertices inside the fiducial volume of the detector and of neutrino-induced muon events that pass the entire detector are presented, which are used for the search for cosmic-ray induced neutrino emission in the Galactic plane and for neutrino emission from 1ES 1959+650 during its spring

2016 flaring phase, respectively. Close attention is given to the atmospheric neutrino self-veto capabilities of the first selection, which is of particular importance for the search of astrophysical neutrinos in the southern sky with IceCube.

Chapter 7 This chapter is dedicated to the search for cosmic-ray induced neutrino emission in the Galactic plane. The analysis method is discussed; sensitivities and discovery potentials for the used Galactic neutrino flux models are presented; and the unblinding status is outlined.

Chapter 8 This chapter focuses on the second analysis presented in this thesis. The search method for neutrino emission from 1ES 1959+650 is explained; the sensitivity and discovery potential are discussed; and the unblinding results are presented.

The thesis is concluded in Chapter 9. Supplementary information are given in the appendix, e.g. the index of frequently used abbreviations and terms on page 107.

2 Leptons from the Atmosphere at TeV Energies

Before focusing on the searches for neutrinos of extra-terrestrial origin, atmospheric neutrinos and muons, produced in cosmic-ray air showers, are introduced, which are the dominant backgrounds in these searches.

2.1 Cosmic Rays

Cosmic rays are ionized particles that are accelerated at yet unknown sites in and outside of the Galaxy; most cosmic rays have to be of Galactic origin [3]. Protons are the most abundant nuclei in cosmic rays, followed by helium; the rest are heavier nuclei. Due to deflection in astrophysical magnetic fields, cosmic rays reach Earth almost isotropically [4].

Fig. 2.1 shows the cosmic-ray proton spectrum, measured by the spaceborne experiment AMS-02 and the balloon experiment CREAM up to energies of about 100 TeV, and the cosmic-ray all-particle spectrum, measured by surface detectors like IceTop or the Pierre Auger Observatory [5–8]. The energy spectrum spans from roughly 1 GeV to 10^{11} GeV. Above this energy, the cosmic-ray flux cuts off. The energy spectrum is almost featureless and up to PeV energies well-described by a single power law,

$$\Phi \equiv \frac{d^4N}{dE dA d\Omega dt} \propto E^{-\gamma}, \quad (2.1)$$

with a spectral index of $\gamma = 2.7$ [4]. Eq. (2.1) gives the differential cosmic-ray flux Φ , defined as the number of particles N per energy interval dE , area dA , solid angle $d\Omega$, and time interval dt . There are two transition regions in the cosmic-ray energy spectrum where the spectral slope changes: it steepens above the *knee* at about 3 PeV and softens again above the *ankle* at about 3 EeV; see the bottom plots shown in Fig. 2.1. It is assumed that Galactic cosmic-ray acceleration approaches its limit in the knee region, which is sup-

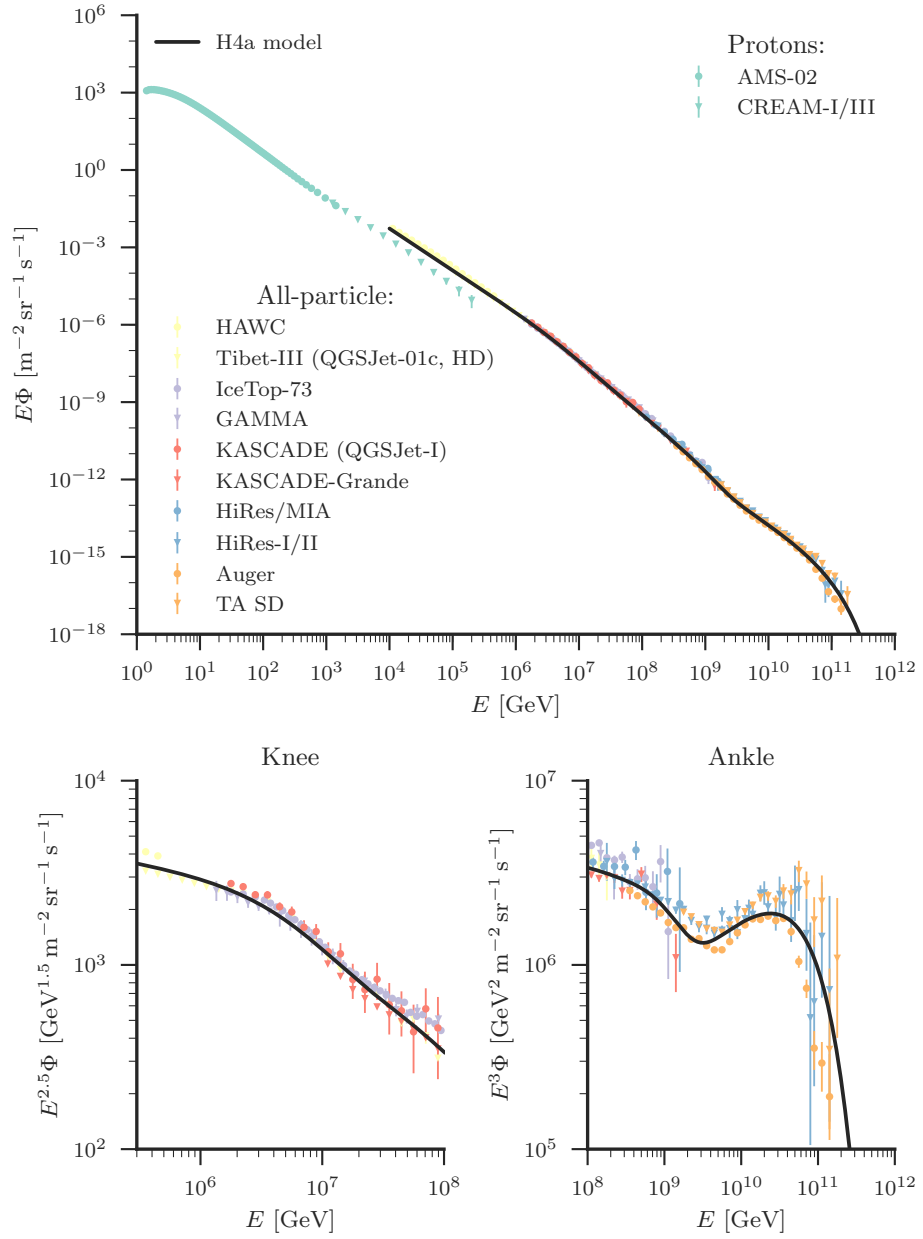


Figure 2.1: Cosmic-ray proton and all-particle energy spectra. Only statistical uncertainties are shown. Data is taken from [5–7, 9–16]. The solid black line shows the prediction of the H4a model [17].

ported by measurements with the KASCADE detector [12]; the data indicates that the transition is associated to a *Peter cycle*,

$$E_c = A \times E_{N,c} = Ze \times \rho_c, \quad (2.2)$$

meaning that, if there is a characteristic rigidity ρ_c above which the acceleration approaches its limit, the transition energy per nucleus E_c should depend linearly on its mass number A , where E_N is the energy per nucleon [18]. The magnetic rigidity $\rho = pc/Ze$ is the ratio of total energy $E = pc$ over charge $q = Ze$; it is the relevant quantity for describing both acceleration and propagation of charged relativistic particles in magnetic fields. The ankle is often associated to the emergence of a cosmic-ray population of extra-galactic origin. Recently, the Pierre Auger Collaboration reported on the discovery of an anisotropy in the arrival direction of cosmic rays with energies above 8 EeV, which indicates that these are of extra-galactic origin [19]. The cut-off at 10^{20} eV is usually either explained by the GZK effect: energy loss due to photo-pion production in cosmic-ray proton interactions with photons of the cosmic microwave background during propagation [20, 21]; or due to the maximum acceleration efficiency of extra-galactic sources [22]. Measurements of the cosmic-ray composition at these energies are needed to understand the origin of the cutoff. In order to observe the GZK cutoff, a light composition dominated by protons is required.

The composition of cosmic rays is measured directly up to PeV energies with space-borne and balloon experiments; Fig. 2.2 shows the energy spectra of several primary cosmic-ray elements. Primary cosmic-ray elements are presumably produced at the acceleration site; secondary elements are created during propagation due to spallation. The energy spectra of the heavier elements C, O, Ne, Mg, Si, and Fe follow power laws with similar spectral slopes and the flux ratios between the elements stay rather constant [32]. For proton and helium, the PAMELA experiment observes a hardening of the proton and helium spectra above 250 GeV per nucleon [23]; see the top plots shown in Fig. 2.2. The CREAM experiment has also reported evidence for a similar hardening of the heavier elements above 200 GeV per nucleon [34].

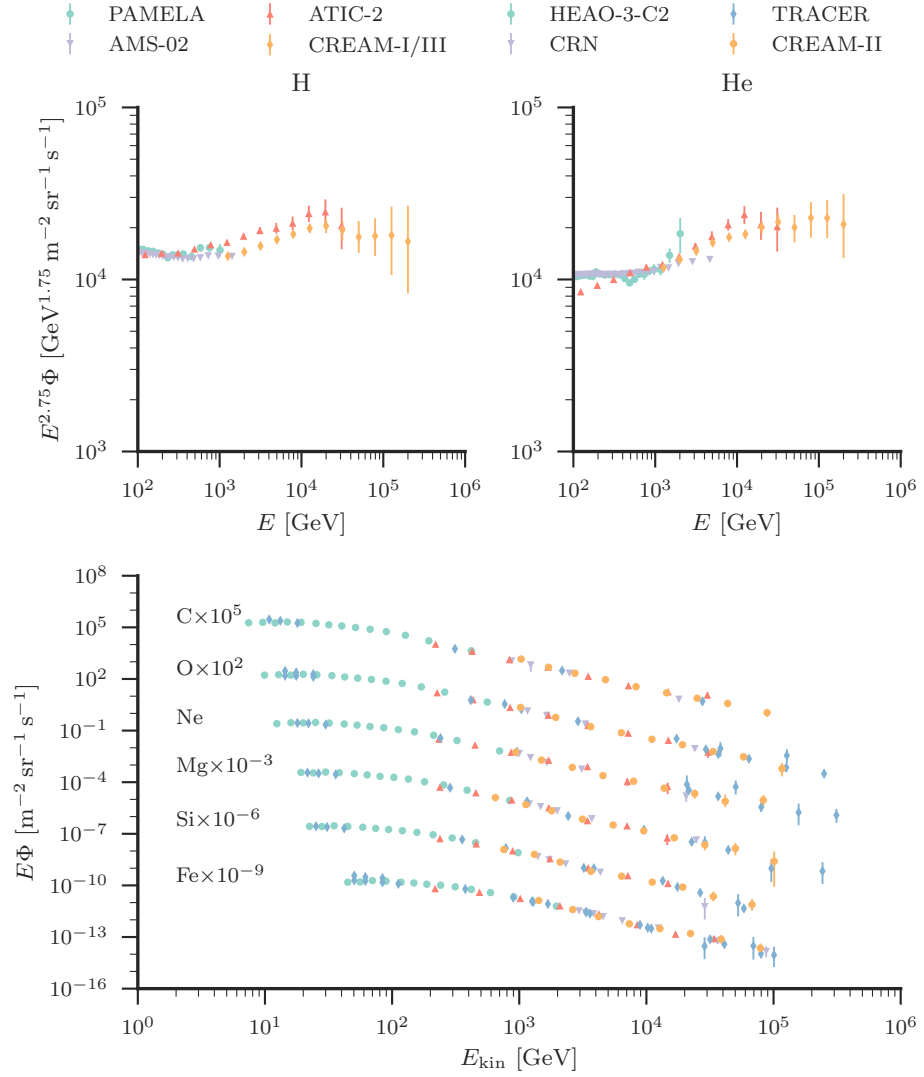


Figure 2.2: Cosmic-ray energy spectra of the primary elements H, He, C, O, Ne, Mg, Si, and Fe. Only statistical uncertainties are shown. Data is taken from [5, 6, 23–32]; data access via the Cosmic-Ray Database [33].

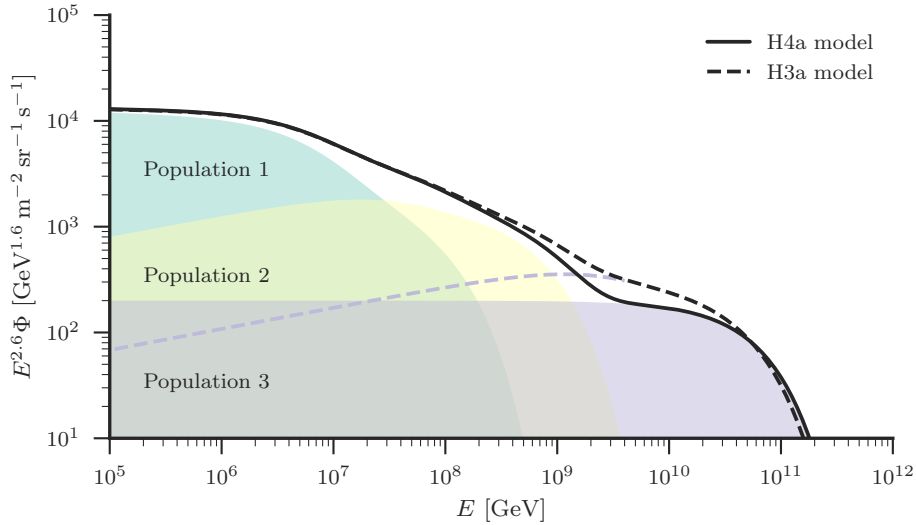


Figure 2.3: Cosmic-ray all-particle energy spectrum predicted by the H3a model (dashed line) and the H4a model (solid line) [17]. More explanations can be found in the text.

The spectral hardening is not described by the standard model of cosmic-ray acceleration and propagation in the Galaxy; see Chapter 3 for more details. The steep-falling cosmic-ray flux and the limited detection area of space-borne and balloon experiments prohibit direct measurements of the cosmic-ray composition at higher energies. Surface detectors on the other hand detect the secondary particles produced in interactions of cosmic rays with the Earth’s atmosphere, which carry only limited information about the primary incoming particle. They rely on Monte Carlo (MC) simulations and composition models to unfold the measured cosmic-ray flux.

Models of the cosmic-ray energy spectrum that are used throughout this thesis are the H3a and H4a models [17]; see Fig. 2.3. These models follow the assumption of Hillas that there are three cosmic-ray populations: cosmic rays accelerated in supernova remnants, a high-energy Galactic population of unknown origin, and a population of extra-galactic origin [35]. The cosmic-ray energy spectrum is parameterized as the sum of three power laws with

exponential cutoffs at characteristic rigidities. Each power law corresponds to one of the three cosmic-ray populations. The normalizations, spectral indices, and characteristic rigidities of the parametrization are obtained from the measurements of CREAM, grouped into the five components H, He, CNO, Mg-Si, and Mn-Fe, and extrapolated to higher energies in a way that is consistent with the surface detector measurements of the cosmic-ray all-particle energy spectrum. The composition of the third cosmic-ray population is assumed to be mixed or protons only for H3a and H4a, respectively.

2.2 Production of Mesons in Cosmic-Ray Air Showers

A cosmic-ray air shower describes a cascade of secondary particles evolving in the Earth's atmosphere, initialized by the primary interaction of a cosmic ray with an air nucleus. A cosmic-ray air shower consists of three components: the hadronic component, the muonic component, and the electromagnetic component. The primary nucleons and secondary hadrons drive the cosmic-ray air shower. Decays of low-energy hadrons like pions and kaons feed the muonic component. Electromagnetic sub-showers are induced by the decay of neutral pions and eta particles into photons, followed by the alternating production of electron-positron pairs and bremsstrahlung. A simplified view on the evolution of a cosmic-ray air shower in the atmosphere is depicted in Fig. 2.4. Detailed simulations of the evolution are obtained with COsmic Ray SIMulations for KAscade (CORSIKA), which tracks particles through the atmosphere until they undergo interactions with the air nuclei, decay, or reach the ground [36]. Hadronic interactions are simulated based on phenomenological particle production models that were fitted to accelerator data and extrapolated up to high energy, e.g. SIBYLL 2.3c [37]. Alternatively, the evolution can be described by coupled cascade equations. The cascade equations are of the form

$$\frac{d\Phi_i(E_i, X)}{dX} = -\frac{\Phi_i(E_i, X)}{\lambda_i} - \frac{\Phi_i(E_i, X)}{d_i} + \sum_{j=i}^J \int_E^{\infty} \frac{Y_{ji}(E_i, E_j)}{E_i} \frac{\Phi_j(E_j, X)}{\lambda_j} dE_j, \quad (2.3)$$

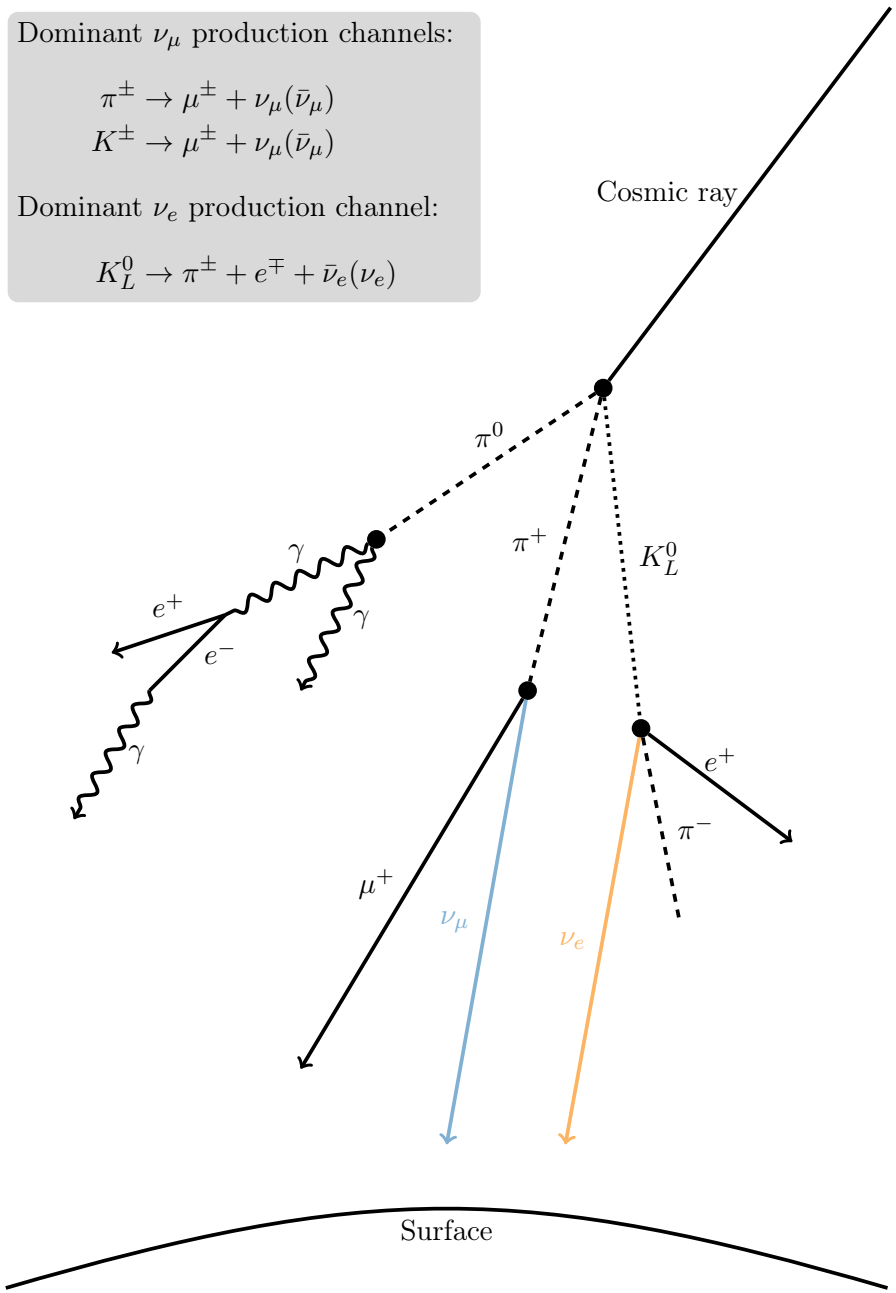


Figure 2.4: Simplified sketch of the evolution of a cosmic-ray air shower in the atmosphere and muon and neutrino production at TeV energies due to the decay of light mesons.

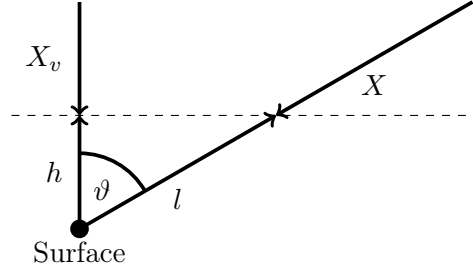


Figure 2.5: Definition of slant depth X and vertical slant depth X_v at an altitude h and a distance l along the shown trajectory. The Earth's curvature is ignored, which is a valid approximation for $\vartheta < 65^\circ$.

neglecting energy losses [4]; $\Phi_i(E_i, X) dE_i$ is the flux of particles of type i with energies between E and $E + dE$ at slant depth

$$X = \int_l^\infty \rho(h(l')) dl'. \quad (2.4)$$

The slant depth depends on the density ρ of the Earth's atmosphere, as illustrated in Fig. 2.5. For an isothermal atmosphere, the density is given by

$$\rho = -\frac{dX_v}{dh} = \frac{X_v}{h_0} = \frac{X \cos(\vartheta)}{h_0}, \quad (2.5)$$

with a scale height of $h_0 \approx 6.4$ km [4]. The probabilities that a particle of type j interacts or decays while traversing the slant depth interval dX are given by dX/λ_j and dX/d_j , respectively. They depend on the interaction length

$$\lambda_j = \frac{Am_p}{\sigma_j^{\text{air}}}, \quad (2.6)$$

and the decay length

$$d_j = \rho \gamma c \tau_j. \quad (2.7)$$

The interaction length depends on the mean mass number A of nuclei in the atmosphere, the proton mass m_p , and the particle-air cross section σ_j^{air} . The decay length depends on the atmosphere's density ρ , the Lorentz factor γ , the vacuum speed of light c , and the particle's rest lifetime τ_j . The term

$$Y_{ji}(E_i, E_j) \equiv E_i \frac{1}{\sigma_j^{\text{air}}} \frac{d\sigma_{j \text{ air} \rightarrow i}}{dE_i} = E_i \frac{dn_i(E_i, E_j)}{dE_i} \quad (2.8)$$

gives the dimensionless particle yield from the collision of a particle of type j and energy E_j with an air nucleus producing a particle of type i and energy $E_i < E_j$. It depends on the differential inclusive cross section $d\sigma_{j \text{ air} \rightarrow i}/dE_i$, integrated over transverse momentum, which can be expressed as the number of particles dn_i produced on average per collision in the energy bin of width dE_i around E_i . For a basic understanding of the production of muons and neutrinos in cosmic-ray air showers, which is described in Section 2.3, it is sufficient to study the pion-nucleon and kaon-nucleon sectors, ignoring nucleon-anti-nucleon production, pion-kaon coupling, and the coupling to other channels [4]. The solutions are of the same form for charged pions and kaons and thus only exemplary shown for charged pions ($\pi^- + \pi^+$). At high energy, pion decay can be neglected and Eq. (2.3) is solved by

$$\Phi_\pi(E, X) = \Phi_0(E) \frac{Z_{N\pi}}{1 - Z_{NN}} \frac{\Lambda_\pi}{\Lambda_\pi - \Lambda_N} \left(e^{-X/\Lambda_\pi} - e^{-X/\Lambda_N} \right), \quad (2.9)$$

where the attenuation length

$$\Lambda_i \equiv \lambda_i / (1 - Z_{ii}) \quad (2.10)$$

and the spectrum-weighted moments

$$Z_{ji} \equiv \int_0^1 x_L^{\alpha-1} Y_{ji}(x_L) dx_L \quad (2.11)$$

are introduced [4]. The primary cosmic-ray spectrum $\Phi_0(E) \equiv \Phi(E, X = 0)$ is assumed to follow a power law with a spectral index of $\gamma = \alpha + 1$. The

interaction length and the particle yields are approximated to be constant and to scale, respectively. Scaling means that the particle yields depend only on the energy ratio x_L of the outgoing and incoming particle. At low energy, where pion decay matters, the solution of Eq. (2.3) is given by

$$\Phi_\pi(E, X) = \Phi_0(E) \frac{Z_{N\pi}}{\lambda_N} \frac{EX \cos(\vartheta)}{\epsilon_\pi} e^{-X/\Lambda_N}, \quad (2.12)$$

where the decay length enters as

$$d_\pi = \frac{EX \cos(\vartheta)}{\epsilon_\pi}, \quad (2.13)$$

which depends on the characteristic energy for charged pions ϵ_π [4]. For a fixed zenith angle ϑ , the characteristic energy describes the energy below which decay dominates. The values for charged pions and kaons are $\epsilon_\pi \approx 115$ GeV and $\epsilon_K \approx 850$ GeV, respectively [4].

2.3 Atmospheric Leptons from Meson Decays

Atmospheric lepton fluxes are divided into a *conventional* and a *prompt* component. The conventional component refers to the leptons from the decays of kaons and charged pions. Prompt leptons are produced in the decays of both mesons containing charm quarks and unflavored mesons. This component has not been observed yet. The differential flux of atmospheric leptons at slant depth X can be calculated from

$$\Phi_i(E_i, X) = \int_0^X \mathcal{P}_i(E_i, X') dX', \quad (2.14)$$

where

$$\mathcal{P}_i(E, X) = \sum_j \int_{E_{\min}}^{E_{\max}} \frac{dn_i(E, E')}{dE} \mathcal{D}_j(E', X) dE' \quad (2.15)$$

is the production spectrum of secondaries of type i [4]. The production spectrum depends on the inclusive spectrum dn_i/dE of secondaries i from the decay of particles j with energy E' and on the decaying particles' spectrum \mathcal{D}_j , e.g., $\mathcal{D}_\pi = \Phi_\pi(E, X)/d_\pi$ for charged pions. Conventional atmospheric muon neutrinos are produced in two-body decays of charged pions and kaons with branching ratios of $\text{BR}_{\pi\nu} \approx 100.0\%$ and $\text{BR}_{K\nu} \approx 64\%$, respectively [38]. For a relativistic unpolarized meson, which decays via $j \rightarrow \nu\mu$, follows

$$\frac{dn_\nu}{dE_\nu} = \frac{dn_\mu}{dE_\mu} = \frac{1}{1-r_j} \frac{1}{E'} \quad (2.16)$$

and

$$0 \leq E_\nu \leq (1-r_j)E', \quad (2.17)$$

where r_j is the ratio of muon mass squared over meson mass squared [4]. The interpolation of the high and low-energy approximation of Eq. (2.14), obtained from Eq. (2.9) and Eq. (2.12), respectively, and the corresponding equations for charged kaons, yields the conventional muon plus anti-muon neutrino flux at ground [4]

$$\Phi_{\nu_\mu+\bar{\nu}_\mu}(E_\nu) \simeq \Phi_0(E_\nu) \sum_{j \in \{\pi, K\}} \frac{A_{j\nu}}{1 + B_{j\nu} \cos(\vartheta) E_\nu / \epsilon_j}, \quad (2.18)$$

where

$$A_{j\nu} \equiv \frac{Z_{Nj} \text{BR}_{j\nu} Z_{j\nu}}{1 - Z_{NN}} = \frac{Z_{Nj} \text{BR}_{j\nu}}{1 - Z_{NN}} \frac{(1-r_j)^{\alpha+1}}{(1-r_j)(\alpha+1)}, \quad (2.19)$$

and

$$B_{j\nu} \equiv \frac{\alpha+2}{\alpha+1} \frac{1}{1-r_j} \frac{\Lambda_j - \Lambda_N}{\Lambda_j \log(\Lambda_j/\Lambda_N)}. \quad (2.20)$$

The equivalent solution for the conventional atmospheric muons from the decay $j \rightarrow \nu\mu$ is obtained from Eq. (2.14) by using the integration limits $E_{\min} = E_\mu$ and $E_{\max} = E_\mu/r_j$. The solution for conventional electron neutrinos is of the

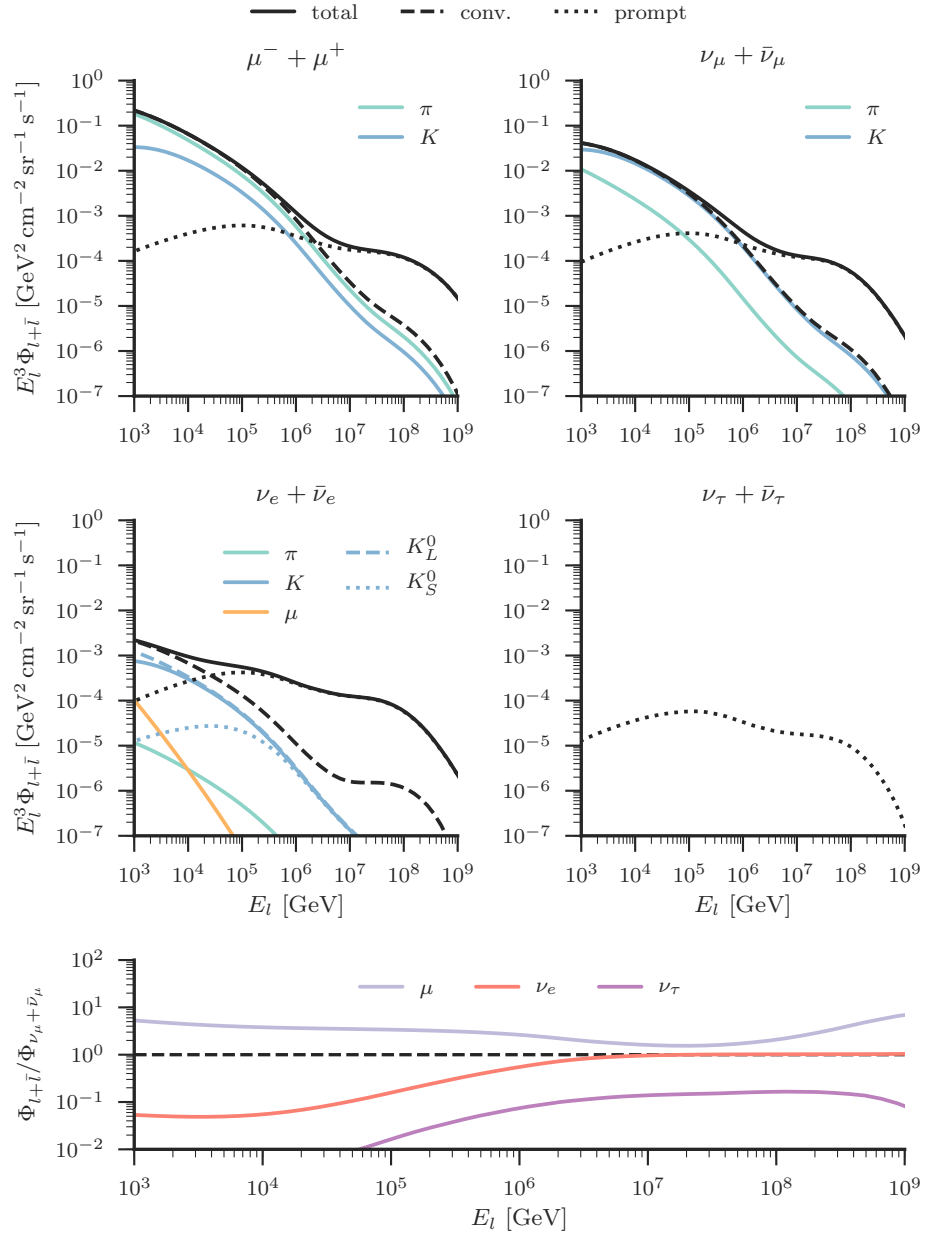


Figure 2.6: Atmospheric lepton fluxes versus energy for a zenith angle of 60° . The fluxes in the bottom plot are normalized to the muon plus anti-muon neutrino flux.

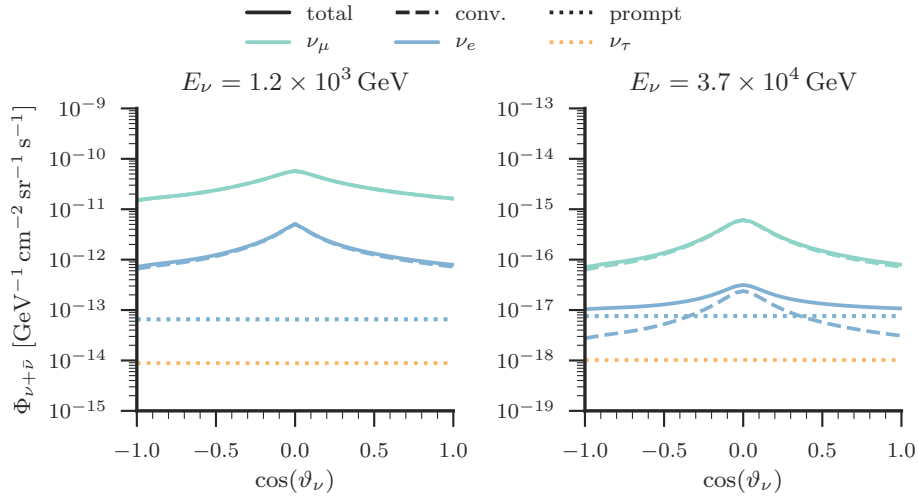


Figure 2.7: Atmospheric neutrino fluxes versus cosine zenith angle for two different neutrino energies.

same form as Eq. (2.18). Fig. 2.6 and Fig. 2.7 show the atmospheric lepton fluxes versus energy for a zenith angle of 60° and versus cosine zenith angle for two reference energies between 1 TeV and 100 TeV, respectively. Here, the coordinate system is centered at the Geographic South Pole. The fluxes are estimated with Matrix Cascade Equation (MCEq), which numerically solves Eq. (2.3) in a matrix form [39]; H3a and SIBYLL 2.3c are used as the primary cosmic-ray spectrum and the hadronic interaction model, respectively. The Earth's atmosphere is modeled empirically based on [40]. At TeV energies, π^\pm , K^\pm and K_L^0 decays are the dominant sources of atmospheric muons, atmospheric muon neutrinos, and atmospheric electron neutrinos, respectively; the decay channels are listed in Fig. 2.4. The energy spectra of conventional atmospheric leptons are steeper than the primary cosmic-ray spectrum; the decay length is proportional to E^{-1} while the interaction length changes only slowly with energy. The conventional atmospheric lepton fluxes peak at the horizon, which is reflected by the $\cos^{-1}(\vartheta)$ dependence in Eq. (2.18); horizontal mesons have longer path lengths and thus more time to decay. The conventional atmospheric electron neutrino flux is about one order of magni-

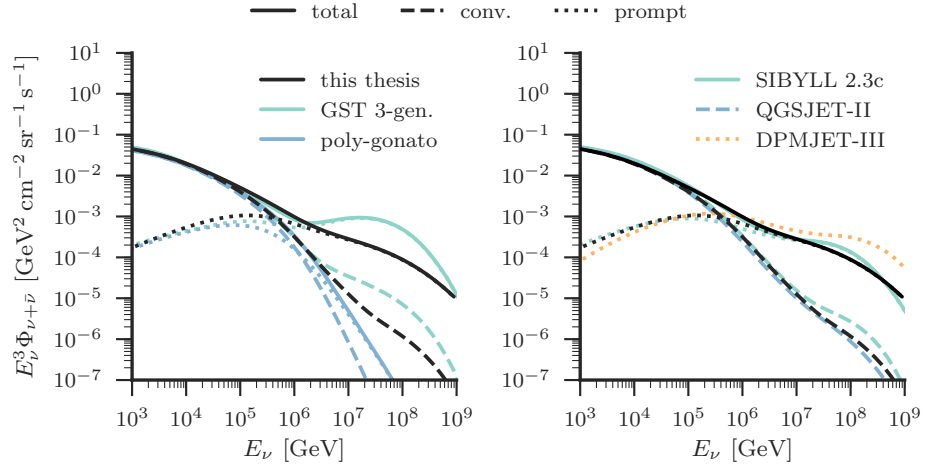


Figure 2.8: Dependency of the all-flavor atmospheric neutrino fluxes on the primary cosmic-ray spectrum and the hadronic interaction model [17, 37, 43–46]. The fluxes are averaged over the entire sky.

tude lower than the conventional atmospheric muon neutrino flux. Prompt leptons on the other hand have energy spectra that are closer to the primary cosmic-ray energy spectrum and a flat cosine zenith angle distribution due to the short lifetimes of charmed mesons; they decay quasi-instantaneous. Consequently, prompt atmospheric leptons should dominate the total atmospheric lepton fluxes at higher energies and for near-vertical directions. Moreover, prompt atmospheric electron and muon neutrino fluxes are almost equal and the prompt component is the only atmospheric source of tau neutrinos.

In this thesis, the conventional and prompt atmospheric neutrino flux models HKKMS06 and ERS are used, respectively [41, 42]. The conventional neutrino flux model is extended to higher energies based on the analytic approximation described before. Additionally, both models are re-weighted with respect to the primary cosmic-ray model H3a in order to account for the cosmic-ray knee. The final energy spectrum is shown in Fig 2.8, compared to the fluxes obtained from MCEq, using different primary cosmic-ray flux and hadronic interaction models, which illustrates the main sources of uncertainties in the flux determination.

3 Extra-Terrestrial Neutrinos above TeV Energies

This chapter gives an overview of the different measurements of neutrinos of extra-terrestrial origin with IceCube and introduces the potential astrophysical sources of neutrino emission that motivate the analyses presented in this thesis.

3.1 Current Interpretation of the IceCube Neutrino Flux

IceCube is a deep in-ice neutrino telescope located at the Geographic South Pole; a detailed introduction is given in Chapter 4. IceCube observes neutrinos of both atmospheric and extra-terrestrial origin using different event topologies in the detector. The first discovery of a diffuse astrophysical neutrino flux was made with high-energy events whose interaction vertices are well-contained within the detector's fiducial volume: high-energy starting events (HESE) [47, 48]. An isotropic unbroken power-law fit to six years of data yields a differential per-flavor neutrino plus anti-neutrino flux of

$$\Phi_{\nu+\bar{\nu}}(E_\nu) = c_0 \times 10^{-18} \text{ GeV}^{-1} \text{ cm}^{-2} \text{ sr}^{-1} \text{ s}^{-1} \left(\frac{E_\nu}{100 \text{ TeV}} \right)^{-\gamma} \quad (3.1)$$

between 60 TeV and 10 PeV, where

$$c_0 = 2.46 \pm 0.08 \quad (3.2)$$

and

$$\gamma = 2.92^{+0.29}_{-0.33}, \quad (3.3)$$

assuming a neutrino flavor ratio of 1:1:1 [49]. The discovery is confirmed by an independent analysis that selects through-going muon tracks arriving from the northern sky and thus observed as up-going events [50]. The analysis

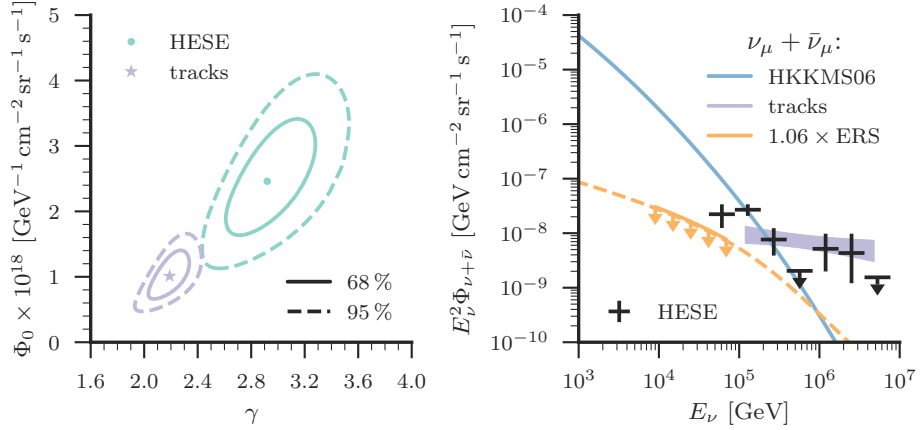


Figure 3.1: Left: confidence level contours in astrophysical per-flavor neutrino flux normalization Φ_0 and power-law index γ based on isotropic unbroken power-law fits to six years of HESE and to eight years of through-going muon tracks, respectively [49, 51]. Right: unfolded astrophysical per-flavor neutrino flux based on HESE compared to the best-fit astrophysical muon neutrino flux obtained with tracks and to the atmospheric muon neutrino flux predictions described in Section 2.3. The shown fluxes are neutrino plus anti-neutrino fluxes.

is sensitive to astrophysical muon neutrinos with energies above 100 TeV. A best-fit differential muon plus anti-muon neutrino flux normalization of

$$c_0 = 1.01^{+0.26}_{-0.23} \quad (3.4)$$

and a spectral index of

$$\gamma = 2.19 \pm 0.10 \quad (3.5)$$

are obtained between 120 TeV and 4.8 PeV, based on eight years of data [51]. Moreover, an upper limit on the not-yet observed prompt atmospheric neutrino flux of 1.06 times ERS is reported [50]. Fig. 3.1 shows a comparison of the two independent astrophysical neutrino flux measurements. They are

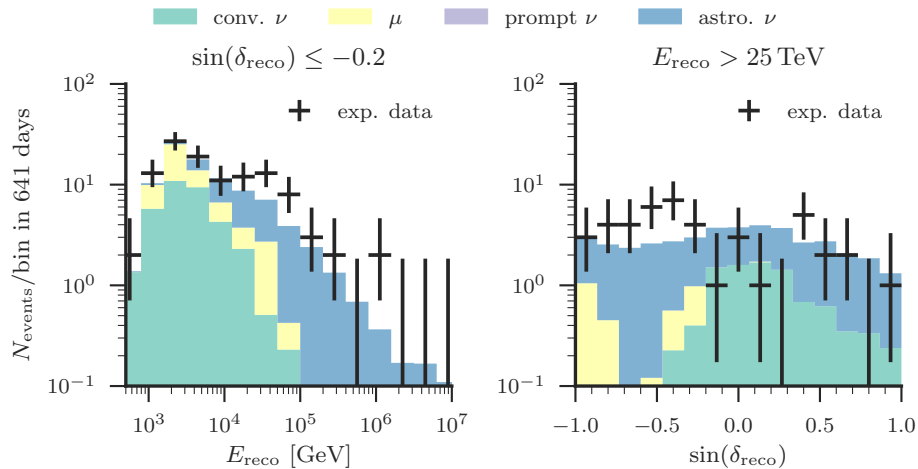


Figure 3.2: Measured energy spectrum in the southern sky and sine declination distribution above 25 TeV with two years of MESE [52]. The best-fit MC flux templates for atmospheric leptons and astrophysical neutrinos (isotropic unbroken power law) of the performed binned forward-folding likelihood fit are shown color-coded and stacked; the prompt atmospheric neutrino flux is fitted to zero. The fit method is described in Chapter 7.

consistent above 200 TeV; a tension is however visible if both event samples are tried to be described with a single isotropic unbroken power law over the entire energy range. The tension's cause is not-yet resolved; partly because the astrophysical neutrino flux at lower energies is difficult to measure with through-going muon tracks due to the overwhelming atmospheric neutrino background. Analyses based on starting events do not suffer this limitation because of their atmospheric neutrino veto capabilities; more details are given in Chapter 6, where the aforementioned event selections and the atmospheric neutrino veto are introduced. Fig. 3.2 shows the energy spectrum in the southern sky and the sine declination distribution above 25 TeV measured with two years of medium-energy starting events (MESE); this sample is based on an extension of the high-energy selection to neutrino energies between 1 TeV to 10 TeV [52]. There is an excess of experimental data observed around 30 TeV

and a declination of 30° (Galactic Center region) that is not well-described by the performed binned forward-folding likelihood fit, including only a single astrophysical neutrino flux template based on an isotropic unbroken power law. The excess is still consistent with a statistical fluctuation [52], but could indicate the emergence of a second astrophysical neutrino flux component, which could help to explain the tension between the starting event and through-going muon track results. In this thesis, neutrino emission in the Galactic plane is discussed as a candidate for a second astrophysical neutrino flux component; see Section 3.2. However, neither a clustering in the neutrino arrival directions nor a correlation with the Galactic plane has been observed so far, neither with starting events nor with through-going muon tracks [49, 53–55].

3.2 Cosmic-Ray Induced Neutrinos from the Galaxy

Gamma rays and neutrinos are produced in the Galaxy via the decay of neutral and charged pions, respectively, which are created in interactions of cosmic rays with the gas in the interstellar medium. Diffuse gamma-ray emission in the Galactic plane accounts for instance for the majority of all gamma rays detected by the *Fermi* Large Area Telescope (*Fermi*-LAT) [56, 57]. Cosmic-ray induced gamma-ray and neutrino emission depends on the cosmic-ray transport in the Galaxy, which is of the form

$$\begin{aligned} \frac{\partial \psi_i(\vec{\mathbf{r}}, p, t)}{\partial t} &= q(\vec{\mathbf{r}}, p, t) - \frac{1}{\tau_f} \psi_i - \frac{1}{\tau_r} \psi_i + \nabla \cdot \left(D_{xx} \nabla \psi_i - \vec{\mathbf{V}} \psi_i \right) \\ &+ \frac{\partial}{\partial p} p^2 D_{pp} \frac{\partial}{\partial p} \frac{1}{p^2} \psi_i - \frac{\partial}{\partial p} \left[\dot{p} \psi_i - \frac{p}{3} (\nabla \cdot \vec{\mathbf{V}}) \psi_i \right], \end{aligned} \quad (3.6)$$

where $\psi_i(\vec{\mathbf{r}}, p, t)$ is the density per total momentum p at position $\vec{\mathbf{r}}$ of cosmic-ray particles of type i [58]. Sources of cosmic rays are described by $q(\vec{\mathbf{r}}, p, t)$, including the distribution and energy spectra of accelerators of primary cosmic rays and the production of secondary cosmic rays due to spallation and decay; τ_f and τ_r are the time scales for loss by fragmentation and decay, respectively. The spallation part depends on the corresponding cross sections and the density of gas in the Galaxy. Cosmic rays diffuse in the magneto-hydrodynamic

fluid that is formed by the ionized gas in the Galaxy and the Galactic magnetic field due to scattering on random magneto-hydrodynamic waves and discontinuities; the diffusion is described by the spatial diffusion coefficient D_{xx} . In addition, the scattering leads to stochastic re-acceleration of the cosmic-ray particles, which is incorporated via diffusion in momentum space with a diffusion coefficient D_{pp} . Besides diffusion, the transport of cosmic rays via convection in Galactic winds with velocity \vec{V} , which can be cosmic-ray driven, could be important [59, 60]. The momentum loss rate is given by $\dot{p} \equiv dp/dt$ and adiabatic momentum loss via convection, as the wind velocity increases away from the Galactic disk, is described by the term $\nabla \cdot \vec{V}$. In this thesis, two different models for neutrino emission in the Galactic plane are used, which are described in the following.

Fermi-LAT Model

In [61], *Fermi-LAT* observations of diffuse gamma-ray emission are modeled with GALPROP¹, which numerically solves Eq. (3.6) on a spatial grid and a grid in momentum; the equation's time dependence is followed until a steady state is reached. The spatial diffusion coefficient is approximated as

$$D_{xx}(\rho) = \beta D_0 \left(\frac{\rho}{\rho_0} \right)^\delta, \quad (3.7)$$

where $\beta = v/c$ is the particle velocity v in units of vacuum speed of light c [62]; the factor results from the random walk the cosmic rays perform during propagation. In case of re-acceleration, the spatial and momentum diffusion coefficients are related via

$$D_{pp} D_{xx} = \frac{4p^2 v_A^2}{3\delta(4 - \delta^2)(4 - \delta)}, \quad (3.8)$$

where v_A is the Alfvén velocity magneto-hydrodynamic waves travel with [63]. For the *Fermi-LAT* reference model ^SS ^ZZ4 ^RR20 ^TT150 ^CC5, a cylindrical geometry is configured with a radius of $R = 20$ kpc and a height of $z = \pm 4$ kpc; the

¹<https://galprop.stanford.edu/>

coordinate system's origin coincides with the Galactic Center. The diffusion coefficient D_0 at the reference rigidity ρ_0 and the Alfvén velocity are constrained by the locally observed cosmic-ray boron-to-carbon ratio, assuming a scaling of $\delta = 1/3$, which refers to a so-called Kolmogorov spectrum [58, 64]; cosmic-ray transport via convection is neglected. Supernova remnants are assumed to be the sources of primary cosmic rays and the source distribution S is taken from the parametrization described in [65]. The remaining two parameters, T and C , are related to the methods for obtaining the distribution of interstellar gas; only hydrogen and helium are taken into account and the helium distribution is assumed to follow the hydrogen distribution [61].

For this thesis, a model for Galactic neutrino emission is constructed by the author of this thesis by taking the neutral pion decay gamma-ray component, based on [66], from the *Fermi*-LAT reference model as a tracer for charged pion decays. Instead of estimating the neutrino flux from the given gamma-ray flux, a more model-independent approach is chosen: the differential gamma-ray flux is integrated over energy and normalized along solid angle in order to obtain a spatial probability density function (PDF), which is convolved with an unbroken power law in neutrino energy, with the neutrino plus anti-neutrino flux normalization and the spectral index as free parameters. The expected neutrino flux at 30 TeV in Galactic coordinates for a spectral index of 2.5 is shown in the top plot of Fig. 3.3.

KRA Model Tuned on Gamma-Ray Data

The gamma-ray flux predictions obtained in [61] underestimate the observed gamma-ray flux above a few GeV in the Galactic plane region, especially towards the inner Galaxy. Motivated by this discrepancy, the assumption of homogeneous diffusion is relaxed in [67] by introducing a phenomenological radial dependency,

$$\delta(R) = AR + B, \tag{3.9}$$

of the scaling parameter δ in Eq. (3.7), which is implemented in the numerically cosmic-ray propagation solver DRAGON [68]. The free parameter $A = 0.035 \text{ kpc}^{-1}$ is obtained from fits to the *Fermi*-LAT data between 5 GeV

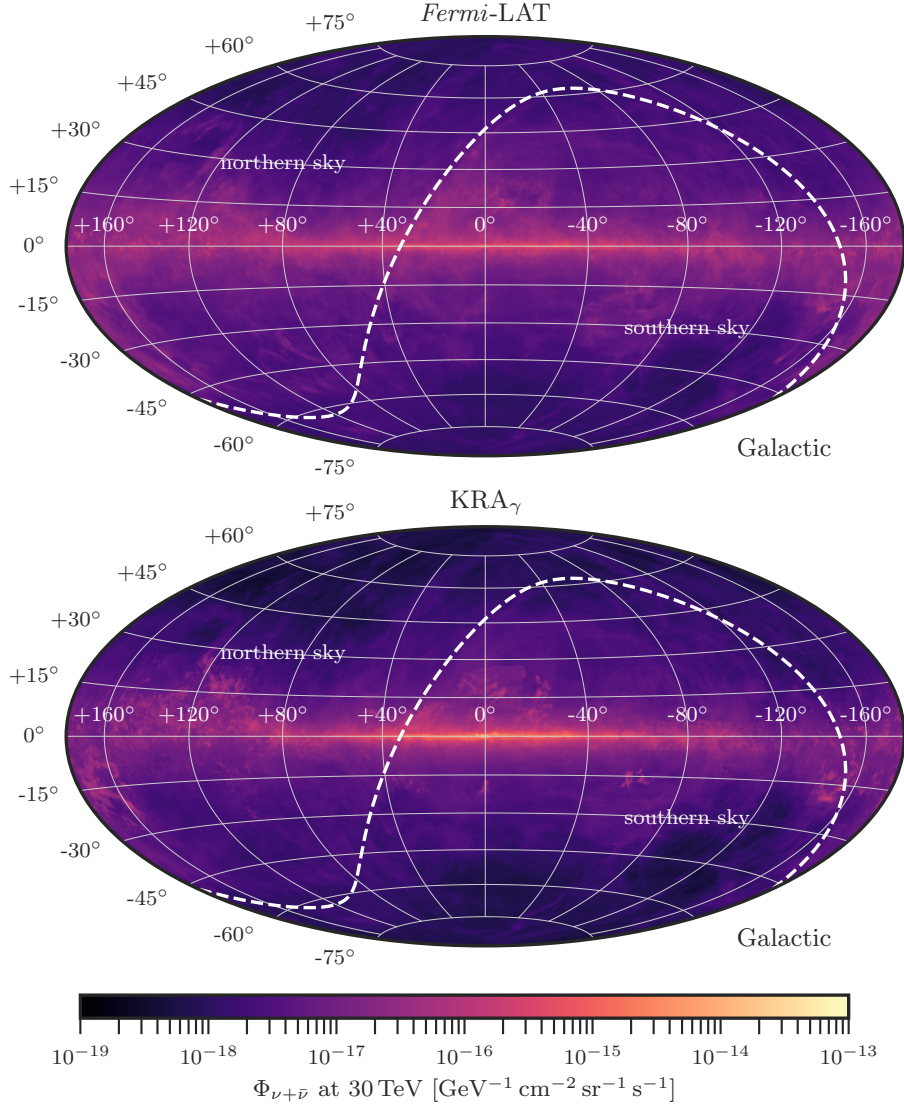


Figure 3.3: Galactic all-flavor neutrino flux at 30 TeV in Galactic coordinates. Shown are the *Fermi-LAT* model for a reference spectral index of 2.5 and the *KRA_γ* model with a cosmic-ray cutoff at 50 PeV. The *Fermi-LAT* model is normalized with respect to the *KRA_γ* model, integrated over energy and solid angle. More explanations can be found in the text.

to 50 GeV; $B = 0.21$ is chosen in order to reflect a so-called Kraichnan (KRA) spectrum of $\delta(R_\odot) = 0.5$ at the location of the sun, $R_\odot \approx 8.5$ kpc [64, 69]. Additionally, convection is allowed along the z -direction in the inner region of the Galaxy, $R < 6.5$ kpc, vanishing at $z = 0$ and growing with $100 \text{ km s}^{-1} \text{ kpc}^{-1}$, and vertical diffusion is implemented as

$$D_{xx}(z) \propto \exp\left(\frac{|z|}{z_t}\right), \quad (3.10)$$

where $z_t = 4$ kpc; the model is labeled as KRA_γ . In [2], the gamma-ray predictions are extended to TeV energies and the spectral hardening of the cosmic-ray proton and helium spectra observed by PAMELA above 250 GeV per nucleon, see Chapter 2, are taken into account via extrapolation up to an exponential cutoff of either 5 PeV or 50 PeV. Moreover, neutrino flux predictions are provided based on [66, 70], taking the effect of long-baseline neutrino oscillations into account [71]. In this thesis, the focus is on the model representation that assumes the spectral hardening of the cosmic-ray proton and helium spectra to originate from a global spectral feature in the rigidity dependence of the cosmic-ray source spectra, which gives a consistent interpretation of the *Fermi*-LAT data and the gamma-ray flux measured by Milagro from the inner Galactic plane at 15 TeV [2, 72]. The expected neutrino flux at 30 TeV in Galactic coordinates for a cosmic-ray cutoff at 50 PeV is shown in the bottom plot of Fig. 3.3. In contrast to the *Fermi*-LAT model, strong neutrino emission is expected from the Galactic Center region due to the inhomogeneous spatial diffusion coefficient. In equatorial coordinates, this region lies in the southern sky, which makes it interesting to test this model with IceCube's all-sky MESE selection, which is introduced in Chapter 6. The expected neutrino spectrum is shown in Fig. 3.4, illustrating how the modifications for KRA_γ lead to a much stronger neutrino flux prediction in comparison to a conventional KRA model, which assumes homogeneous cosmic-ray diffusion.

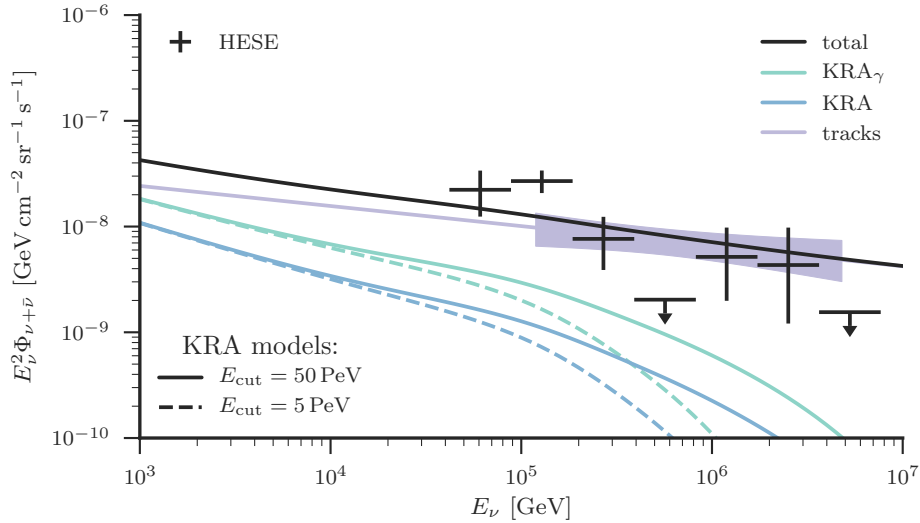


Figure 3.4: Galactic per-flavor neutrino flux versus energy. Shown are a conventional KRA and the KRA_γ model for two different cosmic-ray cutoff energies, averaged over the entire sky and assuming a neutrino flavor ratio of 1:1:1. The black line shows the sum of the KRA_γ model with $E_{\text{cut}} = 50$ PeV and IceCube’s best-fit astrophysical muon plus anti-muon neutrino flux obtained with tracks in comparison to the unfolded IceCube HESE flux. The plot is reproduced from [2].

3.3 Extra-Galactic Source Candidate 1ES 1959+650

Blazars are a class of active galactic nuclei that host a jet oriented at a small angle with respect to the line of sight. Relativistic particles moving within the jet in the presence of a magnetic field emit radiation at various frequencies. If the blazar’s optical spectrum is lacking strong emission or absorption features it is classified as a BL Lacertae (BL Lac) [73]. The BL Lac object 1ES 1959+650 is located at right ascension $\alpha \approx 19^{\text{h}}59^{\text{m}}59.8^{\text{s}}$ and declination $\delta \approx +65^\circ 8' 55.0''$ in the J2000.0 epoch [74]; it has a small redshift of $z = 0.047$ [75]. Gamma-ray emission at TeV energies from 1ES 1959+650 was first detected by the Telescope Array experiment in 1999 [76]. The spectral energy distribution

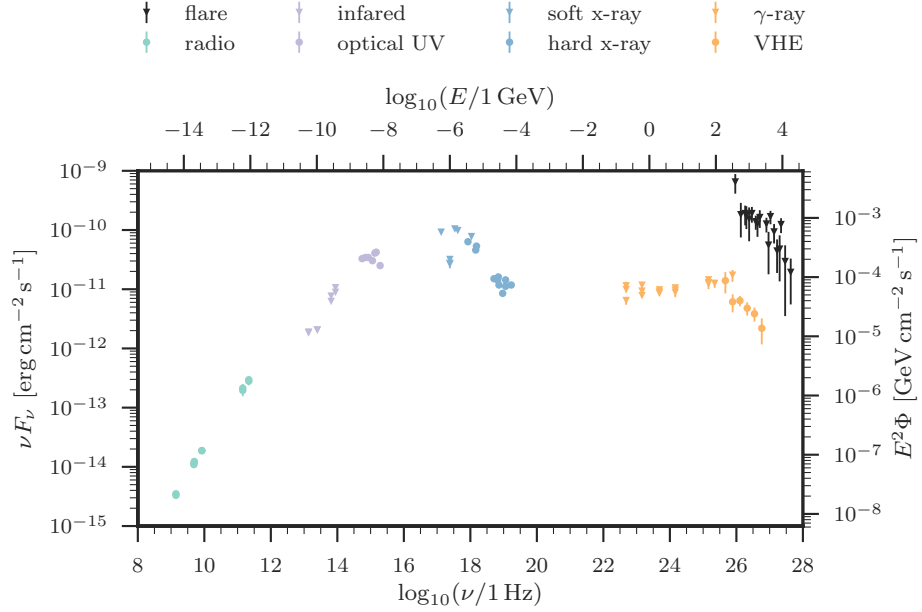


Figure 3.5: Spectral energy distribution of the BL Lac object 1ES 1959+650, while in quiescent state. The VHE gamma-ray flux measured by Whipple during the strong flare in 2002 is shown in black [77].

(SED) of 1ES 1959+650², shown in Fig. 3.5, shows two characteristic humps in the x-ray and gamma-ray frequency range, respectively. The frequency of the first peak further classifies the object as a high-energy peaked BL Lac (HBL) [78]. This peak is usually associated to the maximum energy electrons in the jet can be accelerated to [79]; these electrons emit synchrotron radiation. Among others, the second peak can be explained by inverse-Compton emission, a photo-hadronic component, or the combination of both [80, 81]: energy is transferred from the electrons to the synchrotron or external photons via multi-scattering; high-energy photon pairs are produced in proton-proton and proton-photon interactions via the decay of neutral pions. In the model of synchrotron self-Compton (SSC), the synchrotron photons are the targets for the inverse-Compton emission. A strong *orphan* flare from 1ES 1959+650

²Data from <https://tools.asdc.asi.it/>

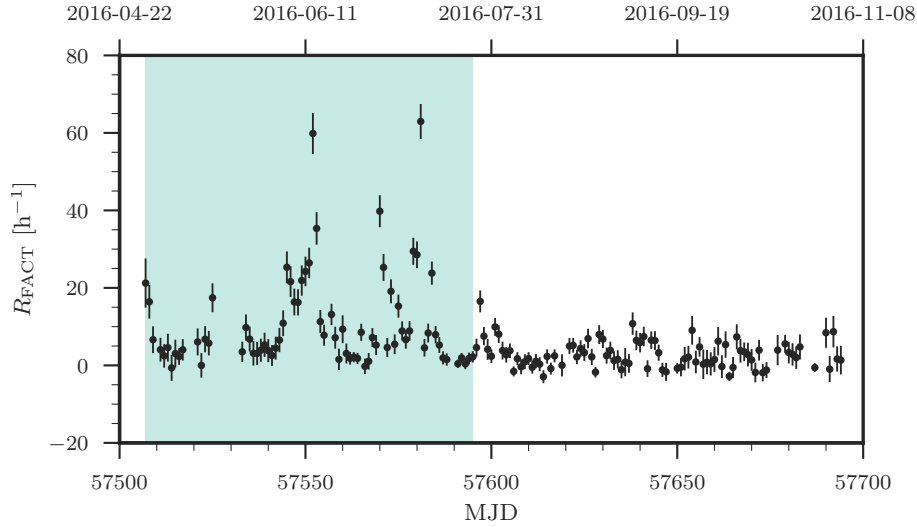


Figure 3.6: Excess rate measured with the FACT telescope. Several flares from 1ES 1959+650 were reported between the 29th of April and the 26th of July 2016 [82–86].

was detected in 2002 with the Whipple telescope [87]. An orphan flare is characterized by an increased source activity in very high energy (VHE) gamma rays without increased x-ray emission. A SSC model fit to the flare’s SED was found to be in contradiction with the observed radio and optical radiation [87]; this makes 1ES 1959+650 an interesting candidate for photo-hadronic emission and thus a potential source of neutrino emission via the decay of charged pions, also produced in proton-proton and proton-photon interactions. This is further supported by the detection of high-energy neutrinos spatially and temporally coincident with the flare with the AMANDA telescope [88]; the detection’s statistical significance is not accessible because the corresponding analysis was not blind. In this thesis, the focus is on a recent flaring phase of 1ES 1959+650 in spring 2016; Fig. 3.6 shows the excess rate³ versus time in Modified Julian Date (MJD) measured with the FACT telescope [89]. The search for neutrino emission from the flaring phase is presented in Chapter 8.

³FACT quick look analysis: <http://www.fact-project.org/monitoring/>

4 The IceCube Neutrino Observatory

The IceCube Neutrino Observatory is located at the Geographic South Pole; it consists of the air shower surface array IceTop and the in-ice neutrino detector

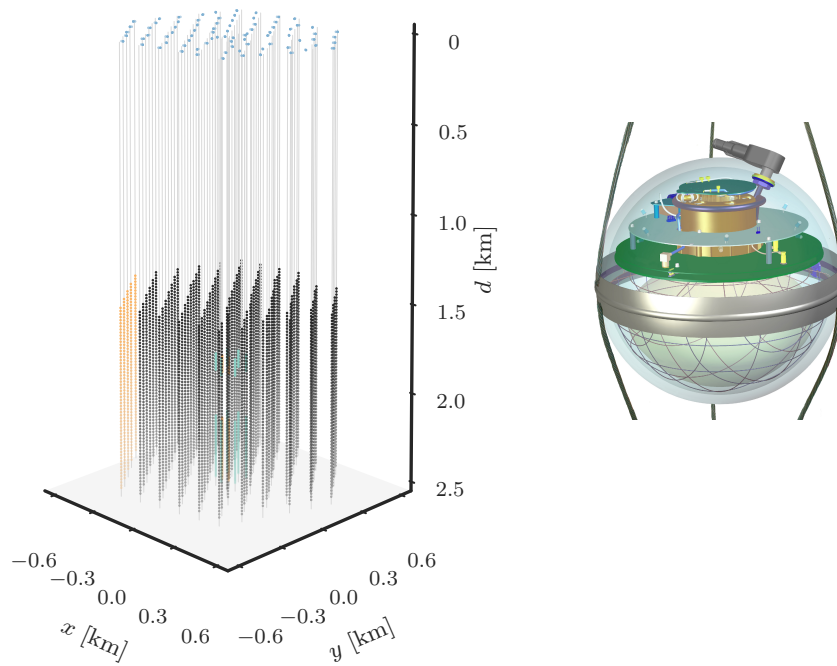


Figure 4.1: Left: positions of the IceCube and DeepCore DOMs along the strings, and of the IceTop surface tanks. Right: IceCube DOM [90]. More details are given in the text.

IceCube [91, 92]. The neutrino detector is a 1 km^3 hexagonal array of digital optical modules (DOMs) in depths of about 1450 m to 2450 m; 60 DOMs each are attached along 86 vertical strings [93]. The detector geometry is illustrated in Fig. 4.1. The deployment of the detector is based on hot-water drilling [93, 94]. A DOM consists of a spherical glass housing that contains a downward-facing 25 cm diameter photomultiplier tube (PMT) and circuit boards for data acquisition, calibration, high-voltage generation, etc. [93, 95]; see the following sections. The PMT is optically coupled to the glass sphere via a silicone gel and shielded from the ambient South Pole magnetic field by a mu-metal cage. The DOM is surrounded by an aluminium waistband and attached to the string via a harness of steel rope; the electronics are connected via a penetrator. The horizontal spacing between the primary IceCube strings is 125 m and the vertical spacing between two neighboring DOMs along a string is 17 m [93]. Of less interest for this thesis is the denser instrumented central DeepCore volume [96, 97]. The detector was constructed over a period of six Antarctic summer seasons from 2004 to 2010; data was also taken during construction. Besides the completed IceCube detector (IC86), IceCube in its 79-string configuration (IC79) is relevant for this thesis; DOMs missing in this configuration are shown in orange in Fig. 4.1.

4.1 In-Ice Neutrino Detection

IceCube can detect neutrinos with energies above 100 GeV that interact with the ice molecules in or close to the instrumented volume. In this energy regime, the underlying neutrino-nucleus scattering is deeply inelastic [98]. Neutrinos of all flavors interact either via the exchange of a W-boson, charged current (CC),

$$\nu_l + X \rightarrow l + Y, \quad (4.1)$$

or via the exchange of a Z-boson, neutral current (NC),

$$\nu_l + X \rightarrow \nu_l + Y. \quad (4.2)$$

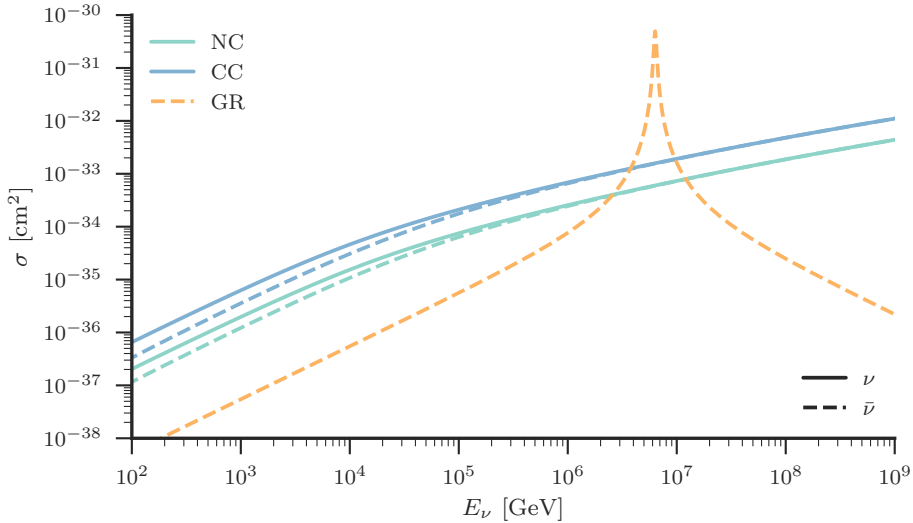


Figure 4.2: Cross sections for deep-inelastic neutrino-nucleon scattering via CC and NC interactions on an isoscalar target and for neutrino-electron scattering via CC interactions of electron anti-neutrinos with energies around the GR [100, 101].

In both cases, the initial ice nucleus X fragments into a hadronic cascade Y . In case of CC interactions, the incoming neutrino ν_l is transformed into an outgoing charged lepton of corresponding flavor l . For electron anti-neutrinos, interactions with the electrons bound in the ice atoms,

$$\bar{\nu}_e + e^- \rightarrow W^-, \quad (4.3)$$

should dominate at the Glashow resonance (GR) [99],

$$E_\nu \simeq \frac{m_W^2}{2m_e} \approx 6.3 \text{ PeV}, \quad (4.4)$$

where m_W and m_e are the W-boson and electron mass, respectively; the W-boson decays either into a lepton pair or into hadrons. Fig. 4.2 shows the cross sections that correspond to the aforementioned neutrino interactions. The deep-inelastic scattering cross sections grow linearly with neutrino energy at

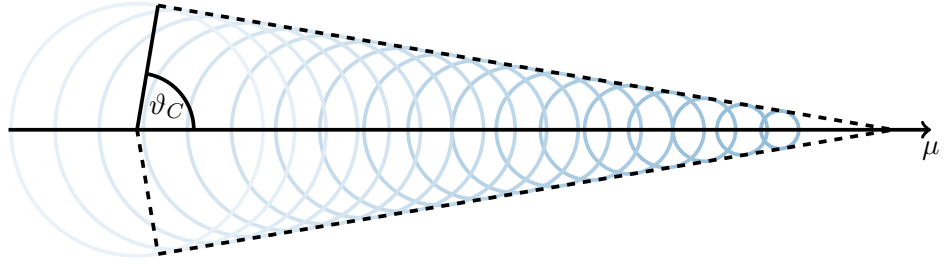


Figure 4.3: Cherenkov light emitted along the path of a charged particle traveling with vacuum speed of light, $\beta = 1$, through a medium with a refractive index of $n = 6$.

lower energies. Above 10 TeV, the momentum transfer starts to dominate over the mass of the exchanged boson and thus the cross sections get suppressed by the propagator term [98]. Above 100 TeV, neutrino scattering on sea quarks starts to dominate and the cross sections of neutrinos and anti-neutrinos become equal [101]. The interaction length of neutrinos, $\lambda_{\text{int}} \propto 1/\sigma$, decreases with neutrino energy. Above TeV energies, the Earth's column density is large enough that neutrinos traversing the Earth can interact before reaching the detector [101]. They get absorbed if they undergo CC interactions. The only exception are tau neutrinos, which are regenerated in CC interactions in the decay of the outgoing tau lepton [102]. In case of NC interactions, a neutrino with reduced energy $(1-y)E_\nu$ is produced, where y is the energy fraction that is transferred from the initial neutrino to the hadronic cascade.

The detection of neutrinos in IceCube is based on the Cherenkov radiation emitted along the path of secondary relativistic particles produced in the neutrino interactions described before. The emitted photons are recorded with the DOMs. Based on the amount of recorded photons and the photons' arrival times, the neutrino energy and direction are reconstructed; see Chapter 5. As illustrated in Fig. 4.3, the emission wavefront forms a cone with an opening angle

$$\cos(\vartheta_C) = \frac{1}{n\beta}, \quad (4.5)$$

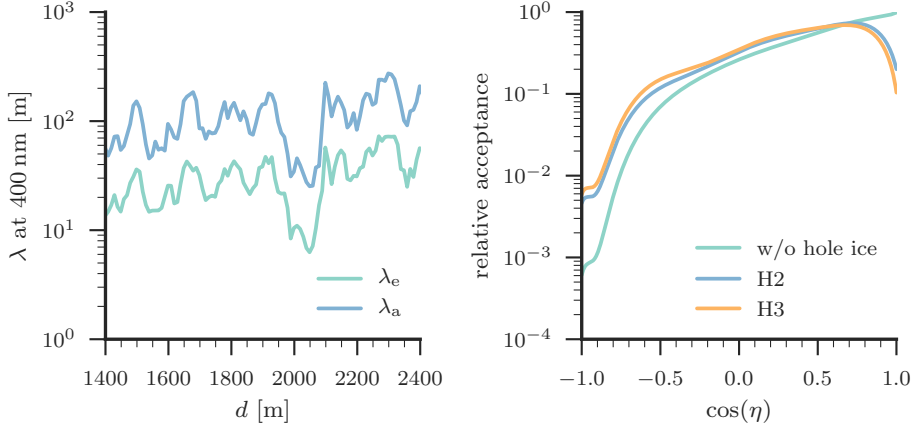


Figure 4.4: Optical properties of South Pole ice. Left: effective scattering and absorption length, λ_e and λ_a , versus depth d [105]. Right: angular sensitivity of the IceCube DOM as measured in the lab and for the hole ice models H2 and H3; $\cos(\eta)$ is the photon arrival angle with respect to the PMT axis. More details are given in the text.

where $n \approx 1.32$ is the refractive index of ice and β the particle's velocity in units of vacuum speed of light; $\vartheta_C \approx 41^\circ$ for $\beta = 1$. The number N of photons emitted in the wavelength range $d\lambda$ along the path dx of a particle with charge Ze is given by

$$\frac{d^2N}{d\lambda dx} = \frac{2\pi\alpha Z^2}{\lambda^2} \sin^2(\vartheta_C), \quad (4.6)$$

where $\alpha = e^2/4\pi$ is the fine-structure constant [103]. Due to the $1/\lambda^2$ dependency, Cherenkov radiation in water/ice appears blue in the optical regime. Before being recorded, the emitted photons can scatter multiple times or get absorbed due to dust embedded in the ice. In this thesis, the South Pole ice (SPICE) model is used [104]; absorption and effective scattering length versus depth are shown in Fig. 4.4. Effective and mean geometrical scattering length, λ_e and λ_s , are related via

$$\lambda_e = \frac{\lambda_s}{1 - \langle \cos(\vartheta) \rangle}, \quad (4.7)$$

where ϑ is the deflection angle at each scatter point; its distribution is approximated with a linear combination of Henyey-Greenstein and simplified Liu scattering [104, 106, 107]. The average absorption length and the horizontal spacing between two neighboring strings are of the same order of magnitude; the average effective scattering length is about a factor four smaller. Hence, scattering is much more important than absorption, except at a depth of about 2 km where both absorption and effective scattering length drop almost by an order of magnitude due to a very high concentration of dust in this ice layer. Moreover, the optical ice properties show an azimuthal dependency [105]. Versions of SPICE with and without this anisotropy incorporated are used in this thesis. Less understood than the bulk ice are the optical properties of the refrozen ice in the drill holes; an ice column filled with air bubbles, drastically reducing the scattering length, is formed around the string during refreezing. The effect of hole ice is modeled into the DOMs' angular acceptance [104]. As shown in Fig. 4.4, less light is expected from up-going events while more photons from downward and horizontal directions can scatter onto the PMT's photocathode. For this thesis, two different acceptance models are considered, which are obtained from simulations. For the H2 and H3 model, a hole ice column with an effective scattering length of 50 cm and 30 cm is assumed, respectively.

4.2 Event Topologies

Two event topologies are used in this thesis, which result from different neutrino interactions.

Cascade-Like Events

Particle showers are produced in NC interactions of neutrinos of all flavors and in CC interactions of electron and tau neutrinos. The outgoing electron or the tau decay induce an electromagnetic cascade, which overlaps with the hadronic cascade at the interaction vertex. The path lengths of charged particles in the cascade are short relative to the horizontal inter-string spacing; together with the scattering of emitted Cherenkov photons, this leads to a more spherical

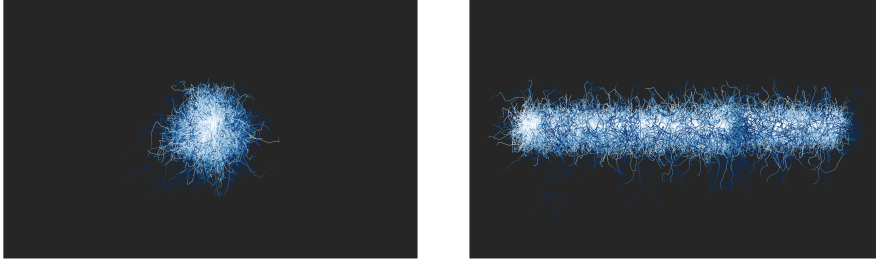


Figure 4.5: Event topologies in IceCube; shown are the paths of photons produced in a 1 TeV electromagnetic cascade (left) and along the path of a 1 TeV muon (right). Color-coded from light to dark blue is the time difference between photon production and absorption.

looking light emission starting from the interaction vertex; see Fig. 4.5. The light yield of hadronic cascades is smaller than for electromagnetic cascades because of neutral particles produced in the shower; nevertheless, it is in general not possible to differentiate CC electron neutrino interactions from NC interactions in IceCube [108]. For well-contained CC electron neutrino events, the entire neutrino energy is deposited in the detector; part of the energy is taken away by the outgoing neutrino in NC interactions. Typical median resolutions on deposited energy and neutrino direction are 10 % to 15 % and 10° to 15° , respectively [47].

Track-Like Events

Tracks are mainly produced in CC muon neutrino interactions. Characteristic for this event topology is the elongated light pattern along the path of the outgoing muon, which can travel through ice for several kilometers. Above TeV energies, the light dominantly originates from showers along the muon track, which are produced via bremsstrahlung, electron-positron pair production, and photo-nuclear effects; these muon energy losses are of stochastic nature [108]. Depending on if the neutrino interaction happens inside or outside of the detector volume, one differentiates between *starting* and *through-going* track

events, respectively. The latter is also the typical signature of atmospheric muons that enter the detector from above. Muon tracks give a long lever arm, which leads to a median angular resolution on the muon track of better than 1° at TeV energies [109]. The muon energy resolution is limited to the deposited energy in the detector and most reconstructions are based on the differential energy loss dE/dx [108].

4.3 Data Acquisition, Processing, and Filtering

Data acquisition, processing, and filtering are described in great detail in [93]. The main aspects are these here summarized. Photons induce an electric current in the PMT. If the signal exceeds a threshold of 0.25 pe, the PMT waveform is recorded for 6.4 μ s, defining a *hit*; 1 pe is a measure of collected charge and defined as the most likely charge deposited from a single photon at a typical PMT gain of 10^7 [108]. An Analog Transient Waveform Digitizer (ATWD) on the DOM Main Bord samples the waveform for 427 ns in 128 bins at a sampling rate of 3×10^8 samples per second. The ATWD has three channels with amplifier gains of $\times 16$, $\times 2$, and $\times 0.25$, respectively; if the first channel saturates, the second one is used, and so on. Each DOM is equipped with two ATWDs, which are operated alternately, in order to reduce dead time. Additionally, a fast analog-to-digital converter (FADC) samples the waveform in 256 bins at a sampling rate of 4×10^7 samples per second. The threshold condition is frequently met due to noise; a typical source of noise is Cherenkov light from ^{40}K decays in the glass sphere. In order to reduce the noise rate, the DOMs are operated in coincidence to their nearest and next-to-nearest neighbors on the same string. If two DOMs signal a launch within $\pm 1 \mu$ s, the hits are flagged as a hard local coincidence (HLC); hits without local coincidence are called soft local coincidence (SLC) hits. All hits are transmitted to the IceCube Laboratory at the surface; HLC hits contain the full ATWD and FADC waveforms; for SLC hits, only three samples of the FADC waveform centered around the peak value are transmitted. At the surface, the HLC hits are searched for multiplicity criteria; relevant for this thesis is the simple multiplicity trigger (SMT) that requires at least eight HLC hits within a sliding

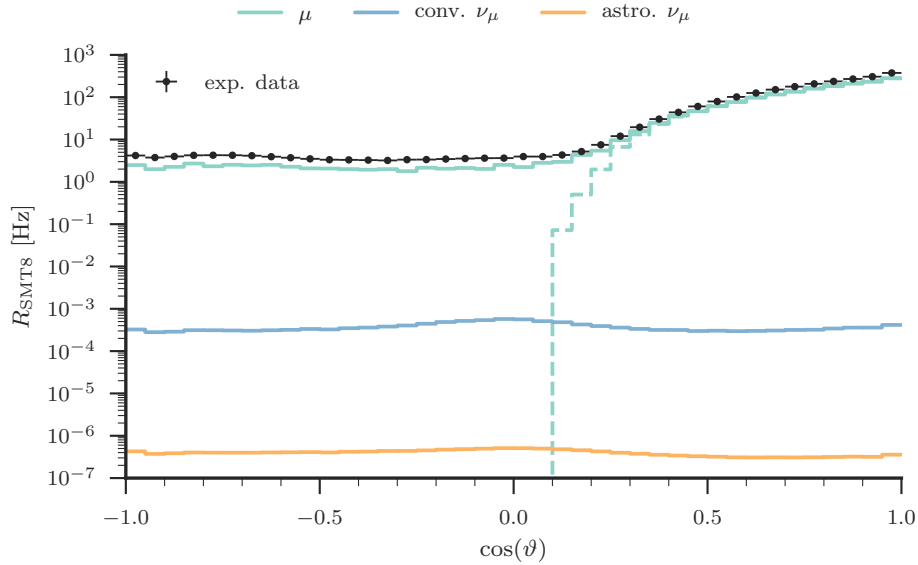


Figure 4.6: SMT8 rate versus cosine zenith angle in detector coordinates; events with cosine zenith angles smaller than zero originate from the northern sky and are observed in the detector as up-going. The event rate from atmospheric muons is several orders of magnitude above the one from conventional atmospheric and astrophysical neutrinos; mis-reconstructed muon events also dominate the trigger rate below the horizon. The dashed line shows the true cosine zenith angle of the simulated muon events.

time window of $5 \mu\text{s}$ (SMT8). All hits within a readout window of $-4 \mu\text{s}$ to $6 \mu\text{s}$ around the trigger window form an *event*; overlapping trigger windows are merged. The event rate at trigger level caused by atmospheric muons is several orders of magnitude above the atmospheric neutrino rate and thus dominates. Muons cannot traverse the Earth; nevertheless, mis-reconstructed muon events also dominate the trigger rate below the horizon; see Fig. 4.6. Due to seasonal variations of the atmospheric muon flux, the trigger rate typically varies from 2.5 kHz to 3 kHz : during Antarctic summer, the atmosphere is warmer and thus less dense; consequently pions more likely decay than interact [4]. Before transmitting the data to the North via satellite, the data

rate has to be drastically reduced in order to meet the satellite's bandwidth. The events are processed and filtered *online*, using fast and computationally inexpensive reconstructions; see Chapter 5. The digitized waveforms are calibrated and deconvolved into series of *pulses*: a pulse has a charge amplitude, pulse width, and leading edge time; its definition is more or less arbitrary and not connected to a single photon [93, 108]. The reconstructions run on cleaned pulses; the cleaning removes isolated pulses that are not causally connected to others. Only three event filters are relevant for this thesis:

Muon Filter This filter divides the sky at a zenith angle of about 78.5° into an up and down-going region, based on a likelihood reconstruction under the hypothesis of an infinite muon track. In the up-going region, the filter cuts on the reconstruction quality, which is given by the minimum negative log-likelihood of the reconstruction scaled with a more or less arbitrary factor that depends on the number of hit DOMs; see Chapter 6. In the down-going region, the event rate is adjusted to the up-going region by cutting on the total collected charge; the charge threshold increases with cosine zenith angle as the muon background gets larger; see Fig. 4.6. By applying this filter, the trigger rate is reduced to about 34 Hz on average.

Cascade Filter This filter discards all events with hit DOMs on less than two strings. Passing events are further filtered by cutting on the quality of a likelihood reconstruction under the hypothesis of a cascade-like photon emission; different thresholds are chosen for up and down-going events, which are classified as before. In the down-going region, additional cuts are made on the line fit speed and the minimum tensor of inertia eigenvalue ratio; see Chapter 5. Both variables are used to separate cascade from track-like events. By applying this filter, the trigger rate is reduced to about 30 Hz on average.

EHE Filter This filter selects extremely high-energy events (EHE) by requiring a total collected charge of more than 1000 pe. The data rate is about 1 Hz.

All events that pass at least one filter are transferred north and further processed and stored *offline*; they can be accessed by all analyzers within the IceCube Collaboration and used as the starting point for high-level event selections.

4.4 Calibration

The main *in-situ* calibration source in IceCube is the LED flasher board each DOM is equipped with; 12 LEDs with wavelengths of (405 ± 5) nm are arranged in six pairs, evenly spaced around the board with a 60° separation between adjacent pairs; one LED per pair points downward at an angle that leads to a horizontal emission of light into the ice after refraction through the glass of the DOM housing; the other LED emits light upward into the ice at an angle of 48° after refraction, which is close to the Cherenkov angle [93]. The DOMs can generate flashes from 10^6 to 1.4×10^{11} photons, which correspond to cascades with energies between 7 GeV and 1 PeV [93].

The detector calibration includes verification of the DOM timing response, measurement of the DOM positions, verification of the performance of cascade reconstructions, and measurement of the optical ice properties, which enters the SPICE model [93, 104]. The uncertainties on the optical ice properties are estimated to be less than 10% [104]. Several dust loggers were used during deployment to measure the structure of the horizontal ice layers, providing a *tilt map*, which is also implemented in the SPICE model [104, 110]. The energy scale of the detector is given by the optical DOM efficiency, which gives the mean number of photoelectrons per GeV of deposited energy. The optical DOM efficiency is an effective quantity that depends on the quantum efficiency of the PMT and includes effects like photon absorption in the DOM glass and gel, cable shadowing, and hole ice. It is calibrated based on minimum-ionizing muons with energies around 100 GeV in the detector; they act as a standard candle because their light emission is very well known [108]. The linearity of the DOM response above PeV energies is verified with two 337 nm pulsed nitrogen lasers in the detector [108].

New calibration sources are currently developed for the proposed IceCube-Gen2 detector [111]. The Precision Optical CALibration Module (POCAM) inverts the principle of an integrating sphere [112]: the light from a matrix of LEDs is diffused inside the sphere after multiple reflections on a diffusing layer, which leads to an almost homogeneous light emission. The LED output is monitored *in-situ* to high precision by photosensors. The goal is to reduce the uncertainties on the optical ice properties down to the few percent level. The author of this thesis developed the first simulation of an early version of the POCAM design [113]. A first prototype with a new design was successfully tested in the Baikal-GVD neutrino detector [112]. More details can be found in Chapter B.

5 Event Reconstructions

In this chapter, the energy and directional reconstructions are introduced that are used in this thesis. Because the author of this thesis notably contributed to the work of IceCube’s software group, the core project Gulliver for likelihood-based reconstructions within IceCube’s software framework IceTray is emphasized; the project is currently maintained by the author of this thesis.

5.1 First-Guess Algorithms

First-guess algorithms usually ignore scattering and absorption of photons in the ice; hence, they are fast and computationally inexpensive to compute. In this section, the first-guess algorithms for cascade and track-like events are introduced that are used to seed sophisticated likelihood reconstructions. Moreover, the reconstructions provide variables that are sensitive to the event topology.

Line Fit

The hit pattern is treated as a plane wave moving through the detector. The arrival time t_k of the first pulse detected in DOM k is related to its position \vec{x}_k via

$$\vec{x}_k = \vec{x}_0 + t_k \vec{v}, \quad (5.1)$$

where \vec{x}_0 and \vec{v} are some position and velocity vectors, respectively. This linear problem is solved analytically using the least-square method. The overall reconstruction performance is improved by modifying the standard χ^2 -statistics as described in [114]; the motivation is to minimize the bias due to obvious noise hits. The line fit speed $\|\vec{v}\|$ is sensitive to the event topology; it should be close to zero for perfectly spherical cascades and close to $c \approx 0.3 \text{ m ns}^{-1}$ for minimum-ionizing muon tracks.

Tensor of Inertia

This directional reconstruction for cascade-like events treats the hit pattern as a rigid body respect the collected charge q_k in each DOM k . The center of gravity (COG) is defined as

$$\vec{\mathbf{x}}_{\text{COG}} \equiv \frac{\sum_k q_k \vec{\mathbf{x}}_k}{\sum_k q_k}, \quad (5.2)$$

and the tensor of inertia (TOI) as

$$I^{ij} \equiv \frac{\sum_k q_k \left(\delta^{ij} (\vec{\mathbf{r}}_k)^2 - r_k^i r_k^j \right)}{\sum_k q_k}, \quad (5.3)$$

where $\vec{\mathbf{r}}_k$ is the vector from the COG to the position of DOM k . The TOI has three eigenvalues e_i , which correspond to its three main axes; the longest axis has the smallest eigenvalue. The ratio

$$R \equiv \frac{\min_i e_i}{e_1 + e_2 + e_3} \quad (5.4)$$

quantifies how spherical the hit pattern is; perfectly spherical cascades have ratios close to $R \sim 1/3$, whereas a value close to zero indicates that all hits fall on a single line.

5.2 Directional Reconstructions

The directional reconstruction for track-like events is based on the single-photoelectron (SPE) likelihood model

$$\mathcal{L}_{\text{SPE}} = \prod_k \left(\prod_l p(t_{\text{res}}^l; \xi, \vec{\mathbf{x}}_k) \right), \quad (5.5)$$

where $p(t_{\text{res}})$ is the probability density to observe a pulse l in DOM k under the hypothesis ξ of an infinite muon track (or a point-like cascade) [115]. The

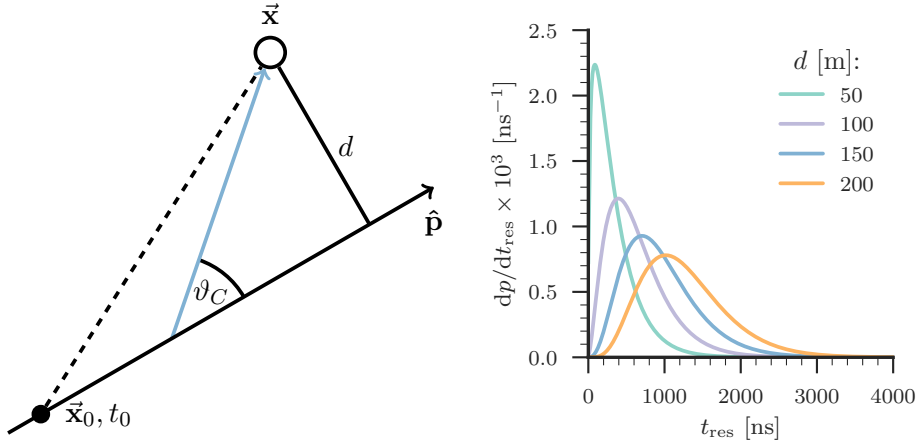


Figure 5.1: Left: sketch illustrating the time residual definition for a photon emitted under the Cherenkov angle ϑ_C along an infinite muon track with an arbitrary support vector \vec{x}_0 and a perpendicular distance d to a DOM at position \vec{x} ; see Eq. (5.6). Right: Gauss-convoluted analytic parametrization, based on Eq. (5.8), of the time residual PDF for different perpendicular distances between infinite muon track and receiving DOM; the standard deviation of the Gaussian distribution is 15 ns.

infinite track is described by an arbitrary point \vec{x}_0 on the track the muon passes at time t_0 and the muon's direction $\hat{\mathbf{p}}$. The PDF depends on the time residual

$$t_{\text{res}} \equiv t - \left(t_0 + \frac{\hat{\mathbf{p}} \cdot (\vec{\mathbf{x}} - \vec{\mathbf{x}}_0) + d \tan(\vartheta_C)}{c} \right), \quad (5.6)$$

which is defined as the time difference between the observed photon arrival time t and the expected arrival time of an unscattered Cherenkov photon; $\vec{\mathbf{x}}$ is the DOM position, d is the perpendicular distance between track and DOM, and c is the vacuum speed of light; see Fig. 5.1. The first pulse detected in a DOM should correspond to the least scattered photon and thus carries more directional information than latter arriving photons. This leads to the

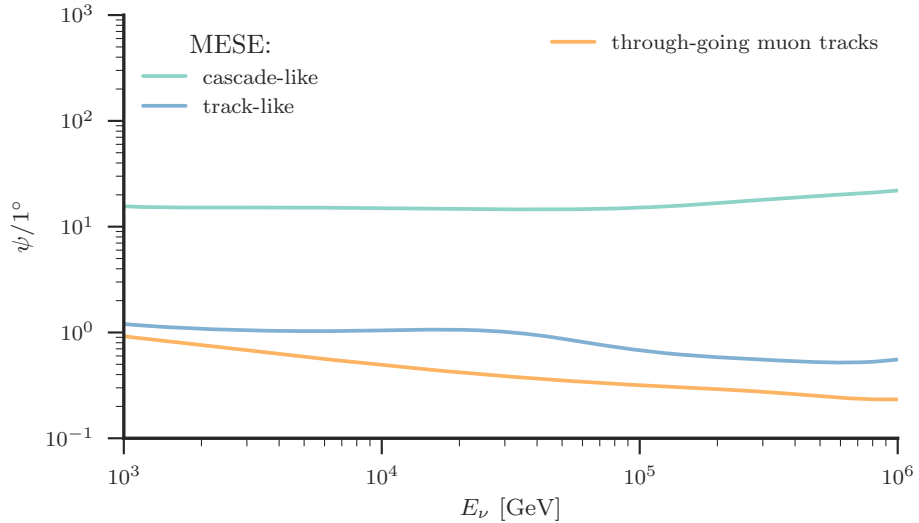


Figure 5.2: Median angular resolution with respect to the primary neutrino for simulated MESE neutrino events classified as cascade or track-like and for simulated muon neutrino events with reconstructed declinations larger than 30° passing the through-going muon track selection.

multi-photoelectron (MPE) likelihood [115]

$$\mathcal{L}_{\text{MPE}} = \prod_k [q_k] p(t_{\text{res}}^0; \xi, \vec{x}_k) \left(\int_{t_{\text{res}}^0}^{\infty} p(t; \xi, \vec{x}_k) dt \right)^{1-[q_k]}. \quad (5.7)$$

For a fast likelihood evaluation, the analytic parametrization

$$p(t_{\text{res}}) \propto \frac{\tau^{-d/\lambda} t_{\text{res}}^{d/\lambda-1}}{\Gamma(d/\lambda)} \exp\left(-\left(t_{\text{res}} \left(\frac{1}{\tau} + \frac{c/n}{\lambda_a}\right) + \frac{d}{\lambda_a}\right)\right) \quad (5.8)$$

can be used, where λ_a is the absorption length and n the refractive index of ice; the free parameters τ and λ are obtained from MC simulations [115]. The parametrization is convolved with a Gaussian, which accounts for the finite time resolution of the PMT [116]. It is shown in Fig. 5.1 for different perpendicular distances between infinite muon track and receiving DOM.

The best angular resolution is obtained with the spline-MPE algorithm, which uses the MPE likelihood and so-called photon tables: spline-interpolated tabulated probability densities $p(t_{\text{res}})$ that are obtained from photon propagation MC simulations, using the SPICE model introduced in Chapter 4 [117, 118]. This reconstruction is used for track-like events, both starting and through-going, in the analyses presented in this thesis. The directional reconstruction for cascade-like events is described in the next section. The median angular resolution for all three event topologies is shown in Fig. 5.2.

5.3 Energy Reconstructions

The energy reconstructions applied to cascade and track-like MESE events are based on the same likelihood model and implemented in the Millipede¹ framework. For the simpler case of cascade-like events, the light yield of a simulated 1 GeV electromagnetic cascade is taken as a template Λ . Because of the linear scaling of the light yield with deposited energy, the template can be scaled up and down to match the collected charge [108]. The likelihood to observe n_k photons per DOM k given the energy deposition E is given by

$$\mathcal{L} = \prod_k \frac{(\Lambda_k E + \rho_k)^{n_k}}{n_k!} \exp(-(\Lambda_k E + \rho_k)), \quad (5.9)$$

where $\lambda_k = \Lambda_k E + \rho_k$ is the expected number of photons in DOM k , including the noise contribution ρ_k [108]. Timing information can be incorporated in the likelihood function by binning the photon arrival time distributions and interpreting n and Λ as the light per time bin [108]. Note that the actual likelihood implementation in Millipede is based on pulses instead of single photons. For this thesis, the likelihood function is also maximized with respect to vertex position and direction through the dependency of Λ on these quantities. The deposited energy of starting track-like events is estimated by extending Eq. (5.9) to multiple photon sources, e.g. stochastic energy losses, placed along the segmented muon track [108]. For through-going muon tracks, a deposited energy per DOM is computed based on the ratio of collected charge

¹ <http://code.icecube.wisc.edu/svn/projects/millipede/>

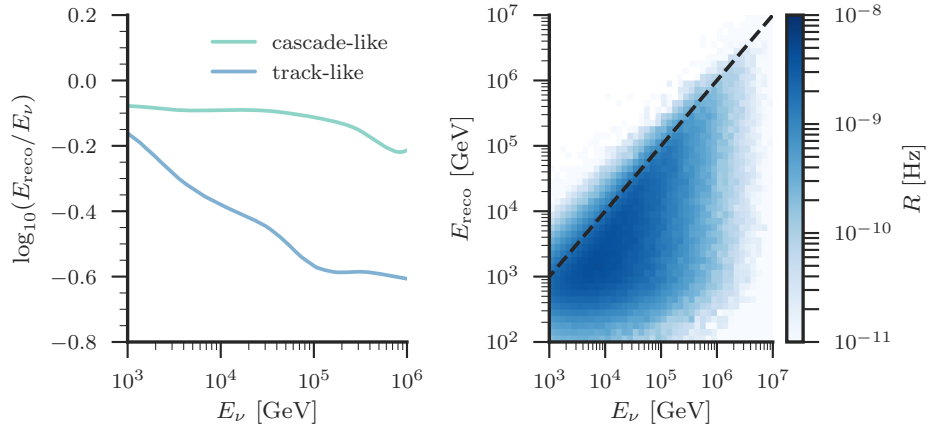


Figure 5.3: Left: median energy resolution relative to the primary neutrino for simulated MESE neutrino events classified as cascade or track-like. Right: correlation between true neutrino and reconstructed energy for simulated muon neutrino events with reconstructed declinations larger than 30° , weighted to an isotropic unbroken power-law flux with a benchmark spectral index of $\gamma = 2$, passing the through-going muon track selection.

and expected charge from a muon template; the highest energy depositions are truncated. The average of the remaining energy depositions is used to obtain the muon energy from the parametrization described in [119]. Fig. 5.3 shows the median energy resolution (logarithmic) of MESE relative to the primary neutrino. The overall median energy resolution for events classified as cascade-like is about 20% and stays rather flat with increasing neutrino energy. The median energy resolution for events classified as track-like is of the same order of magnitude at lower energies but worsens with increasing neutrino energy because the outgoing muon is able to leave the detector before losing all its energy. Fig. 5.3 also shows the correlation between true neutrino and reconstructed energy for simulated muon neutrino events with declinations larger than 30° passing the through-going muon track selection; the correlation is about 60%.

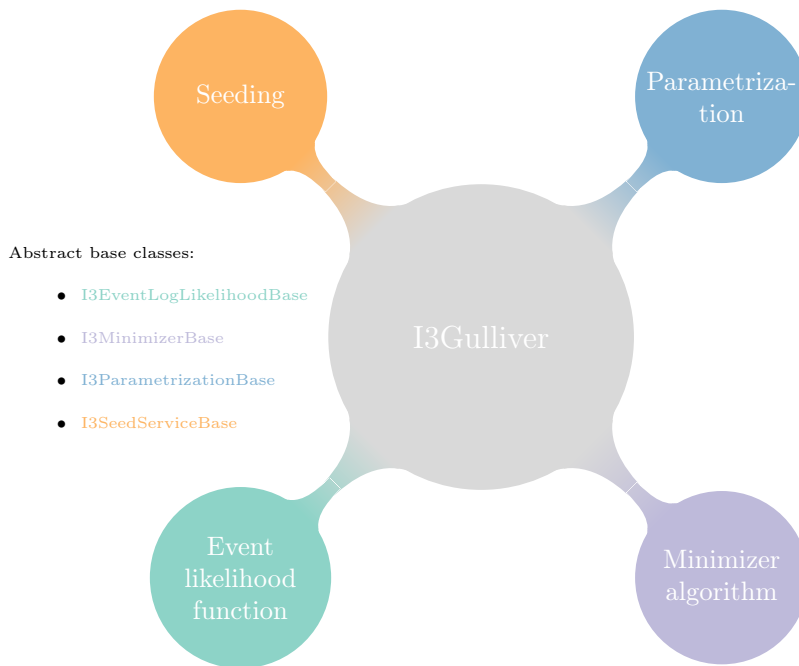


Figure 5.4: Overview of Gulliver components.

5.4 Gulliver Framework

The likelihood-based reconstructions introduced in the previous sections are implemented in IceCube’s software framework IceTray² based on the Generic Utility for Log-Likelihood-based (Ice, $\nu = V$, and Everything else) Reconstructions (Gulliver)³. The I3Gulliver main class takes a likelihood function and services for the likelihood minimization, parametrization, and seeding as member variables; the services are derived from the abstract base classes that are part of Gulliver; see Fig. 5.4. The likelihood function is evaluated based on an event hypothesis object and returns a negative log-likelihood value. The event hypothesis consists at least of an I3Particle, which represents both, simulated and reconstructed particles in the detector. At the beginning of the likelihood minimization, a seed event hypothesis, e.g. the result of a first-

² <http://code.icecube.wisc.edu/icetray/>

³ <http://code.icecube.wisc.edu/svn/projects/gulliver/>

guess reconstruction, is passed from the seeding service to the minimizer via the parametrization service. The parametrization service extracts an array of physics parameter values (doubles) from the event hypothesis, e.g. the components of the particle's position vector and the azimuth and zenith angle of the particle's direction vector. Moreover, the parametrization service specifies step sizes, bounds, and optional transformations for each parameter, e.g. $E \rightarrow \log_{10}(E)$. In each minimization step, the likelihood function is evaluated based on a new event hypothesis given the current set of parameter values. The final event hypothesis is returned together with diagnostics like the minimum negative log-likelihood value and the degree of freedom. The Gulliver framework also provides modules that iteratively repeat the minimization, by seeding the next minimization with the previous result, but randomly changing the direction of the seed hypothesis. This iterative approach can help to avoid false reconstruction results due to local minima of the negative log-likelihood function.

IceCube's software group encourages IceCube analyzers to take over the maintenance of orphaned software projects; the author of this thesis maintains Gulliver and other related projects. The work of a project maintainer includes improving the project's documentation, improving the project's code coverage by implementing new unit tests, fixing bugs in the code, and implementing new or improving existing features, if requested. Bugs and feature requests are reported based on a ticket system. All unit tests are executed on several *build bots* with different setups whenever a new commit is made to the software repository. The main contributions of the author of this thesis to the Gulliver framework are an improved documentation and structure of the code as well as Python bindings for the standard derived minimizer classes, which are written in C++.

In 2015, the so-called *strike team* was formed; the author of this thesis is a member of this team. Every month, the strike team focuses on a specific task for one week in the framework of so-called *code sprints*. Common tasks are code reviews, which are a requirement for new software projects to be declared as official IceCube software projects.

6 Event Selections

In this chapter, the MESE and the through-going muon track selection are introduced, which are used for the analyses presented in this thesis [50, 52, 120, 121]. Moreover, the atmospheric neutrino self-veto is discussed, which is of particular importance for the search for neutrino emission in the Galactic plane [120, 122, 123]. The following sections give only an overview. The event selections and the atmospheric neutrino self-veto were originally developed by other IceCube collaborators to analyze the isotropic/extra-galactic high-energy neutrino flux. More details can be found in the corresponding references.

6.1 Medium-Energy Starting Events

The MESE selection is optimized for neutrino events of all flavors with energies above 1 TeV and selects events from all directions with interaction vertices that are well-contained inside the fiducial volume of the detector. It is an extension of the HESE selection to lower energies [47, 48]. The background of atmospheric muons is suppressed based on straight veto-driven cuts. Presented is an improved version of the original MESE selection described in [120] with superior efficiency, especially with respect to track-like events [124]. The author of this thesis contributed to this selection by processing and analyzing MC systematic datasets. This selection is applied to seven years of data, starting from May 2010 (IC79). Its effective area is shown in Fig. 6.1; see Eq. (B.1). Starting point for the improved MESE selection are the cascade, muon, and EHE event streams introduced in Chapter 4. The original MESE selection was only applied to events that passed an additional pre-selection optimized for cascade events, because atmospheric muon simulations were not available at previous selection levels at the time the event selection was developed [120]. This limitation has been resolved by now. Hence, only the selection steps to reach the neutrino level are described in more detail in the following.

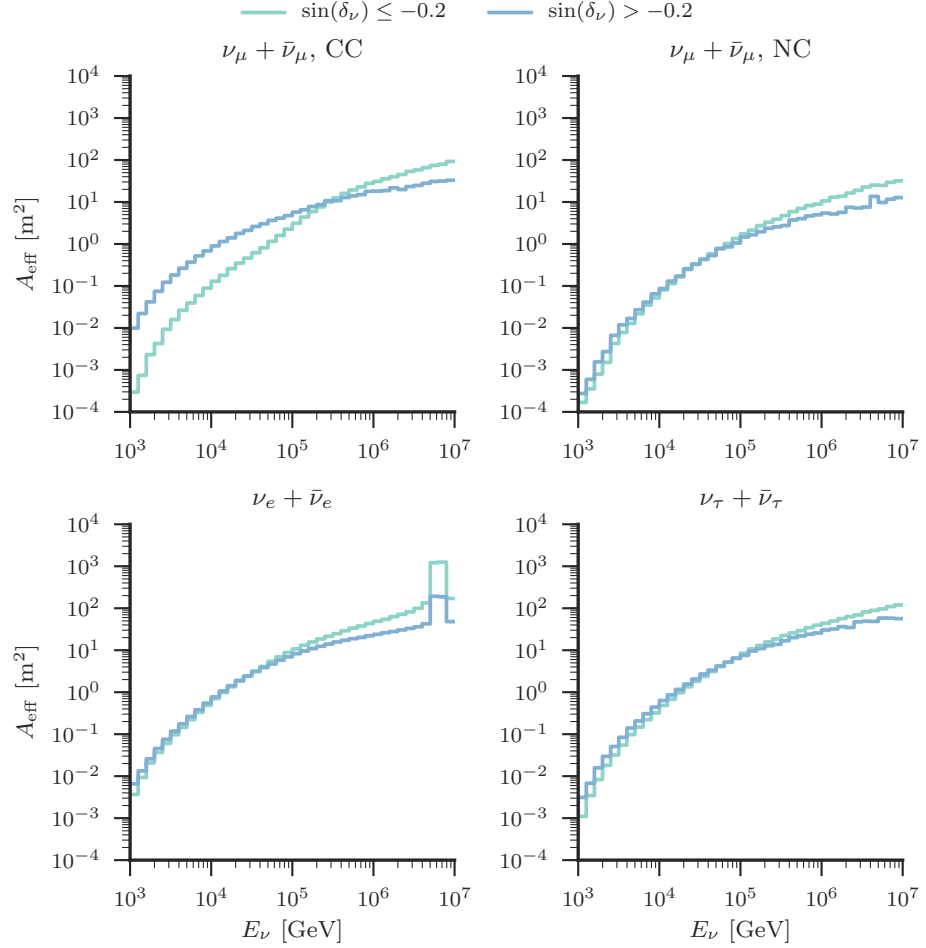


Figure 6.1: Neutrino effective area of MESE selection for IC86 2013. The effective area is shown for all three neutrino flavors and separately for up and down-going events. For muon neutrinos, the effective area is separated into CC and NC, illustrating the different selection efficiencies for track and cascade events.

6.1.1 Clean-Up Cuts

The data still contains coincident events, which mostly arise from muons induced by multiple independent air showers that are detected in a single detector readout. The applied reconstruction algorithms work under the hypothesis of a single track or cascade in the detector and get easily confused by coincident events. That is why a topological splitting algorithm is applied that is able to efficiently split coincident into single events by identifying clusters of casually connected pulses. The selection described in [120] is more stringent and removes all events with more than one identified cluster. Furthermore, badly reconstructed events are removed by requiring at least four hit strings and a homogenized total charge of more than 100 pe; the homogenized total charge is the sum of charges of all HLC pulses detected on non-DeepCore DOMs that do not contribute more than 50% of the total charge.

6.1.2 Outer-Layer Veto

The outer part of IceCube is used as an active veto against atmospheric muons, similar to the one developed for the HESE analysis [47]. The veto region is shown in Fig. 6.2. It consists of the DOMs on the outer strings of the detector, the top¹ 90 m of the detector, the bottommost active DOM on each string, and all DOMs between vertical depths of 2050 m and 2170 m. Events that deposit charge in the veto region before a particular start time are removed. The start time is determined by sliding a time window of 3 μ s through all time-ordered HLC pulses detected on non-DeepCore DOMs until it contains a charge of

$$q = \begin{cases} 3 \text{ pe} & q_{\text{tot}} < 72 \text{ pe} \\ q_{\text{tot}}/24 & 72 \text{ pe} \leq q_{\text{tot}} < 6000 \text{ pe} , \\ 250 \text{ pe} & q_{\text{tot}} \geq 6000 \text{ pe} \end{cases} \quad (6.1)$$

depending on the total charge q_{tot} contained in this pulse series [120]. For events with a homogenized total charge of more or less than 6000 pe, the veto charge threshold is 3 pe and 0 pe, respectively. The veto is thicker at the

¹The top of the detector is measured from the first DOM on the deepest string.

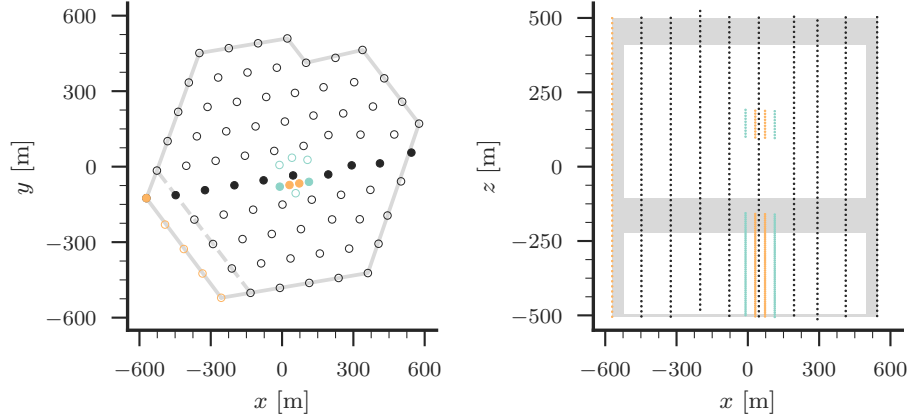


Figure 6.2: Left: top view on the IceCube geometry. Right: side view along the filled strings shown in the left plot. DeepCore strings are shown in turquoise. Strings colored in orange were not yet deployed in the IC79 configuration. The outer-layer veto is shown in gray. The plot is reproduced from [47].

top than at the sides because the muon background from vertical down-going directions is larger; see Fig. 4.6. The only background expected from below are very inclined muons that suffer a stochastic energy loss below the detector. One layer of DOMs is sufficient to remove this background. The veto region between vertical depths of 2050 m and 2170 m prevents inclined muons to sneak in through the ice layer with a high concentration of dust at a vertical depth of 2050 m. The dust concentration leads to short scattering and absorptions lengths, as shown in Fig. 4.4, and thus increases the effective DOM detection threshold. Events with a homogenized total charge of more than 6000 pe that are not vetoed are classified as HESE and kept to final level; all following cuts are not applied.

6.1.3 Inner Track Veto

The remaining background is dominated by dim muons that pass the outer-layer veto undetected before suffering a large stochastic energy loss. This back-

ground is efficiently removed by the inner down-going track veto, which counts the HLC and SLC pulses that are not consistent with cascade-like emission at the reconstructed vertex position, but can be associated to a down-going muon track, going through the reconstructed vertex position. The direction of this track is determined in a scan of 104 equally spaced down-going directions, based on a HEALPix grid [125]. The vertex position is taken from the energy reconstructions for cascade and starting track-like events described in Chapter 5. For starting track-like events, the first energy loss larger than 1 GeV inside the detector along the track is defined as the vertex. The discrimination of cascade and track-like events is presented in Section 6.1.5. Pulses that have a time residual smaller than -50 ns under the cascade hypothesis and between -15 ns and 500 ns under the track hypothesis are counted as veto pulses if their distance to the track is smaller than 100 m. Events with a veto charge of 2 pe or more are removed.

6.1.4 Fiducial Volume Scaling

As the total collected charge in the detector decreases, the incoming muon has to pass more DOMs in order to be rejected by the inner track veto. An efficient rejection is assured by requiring a minimum distance to the edges of the fiducial volume of the detector, which scales with the homogenized total charge. The scaling relations between the homogenized total charge \tilde{q}_{tot} and the distances of the vertex position to the side and top margins of the fiducial volume, d_{side} and d_{top} , are given by [120]

$$\begin{aligned} \log_{10}(\tilde{q}_{\text{tot}}/1 \text{ pe}) &> 3.41 - \frac{(d_{\text{side}}/1 \text{ m})^{1.74}}{17266} \\ \log_{10}(\tilde{q}_{\text{tot}}/1 \text{ pe}) &> 3.40 - \frac{(d_{\text{top}}/1 \text{ m} - 100)^{1.88}}{23710}. \end{aligned} \quad (6.2)$$

The fiducial volume is shown in Fig. 6.3 for four different \tilde{q}_{tot} values. For the dimmest events, the fiducial volume is reduced to the DeepCore volume; the veto volume decreases as the homogenized total charge increases until it coincides with the outer-layer veto.

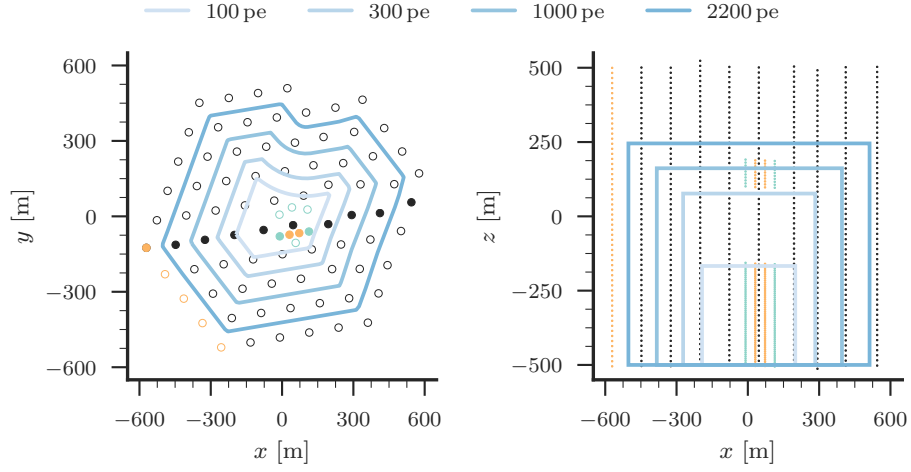


Figure 6.3: Left: top view on the IceCube geometry. Right: side view along the filled strings shown in the left plot. The edges of the fiducial volume for four different homogenized total charge thresholds are shown color-coded. The plot is reproduced from [52].

6.1.5 Event Topology Discrimination

By inverting the logic of the inner track veto, a sub-sample of neutrino-induced up-going muon tracks is defined, which is kept to final level; the fiducial volume scaling is not applied. An event is classified as an up-going muon track if more than 10 pe can be associated to an outgoing muon track starting at the reconstructed vertex position and if the spline-MPE reconstruction yields an up-going muon track. Other events at final level that have a much larger average charge-weighted minimum distance,

$$d \equiv \frac{\sum_k q_k \|\vec{x}_k - \vec{\mathbf{p}}\|_{\min}}{\sum_k q_k}, \quad (6.3)$$

of all hit DOMs k to the best-fit cascade than to the best-fit track hypothesis, each described by $\vec{\mathbf{p}}$, are classified as track-like events. The best-fit hypotheses correspond to the directional reconstruction for cascade-like events described

Cascades	Tracks	Up-going tracks
93 %	93 %	99 %
96 %	89 %	77 %

Table 6.1: Efficiency of event topology discrimination, assuming an isotropic unbroken power-law flux with a spectral index of $\gamma = 2.46$, as reported in [52]. The first and second row are with respect to the reconstructed and true event topology, respectively. Tau neutrino CC events and GR events are not taken into account for the efficiency estimation.

in Chapter 5 and the spline-MPE reconstruction, respectively. The remaining events are further separated into cascade and track-like events based on the inversion of the inner track veto, but taking only HLC pulses into account. Because of their brightness, a more stringent charge threshold is used for the inner track veto for events classified as HESE than for events with lower energies. Additionally, all HESE events that have a track length larger than 500 m are also classified as track-like events. The track length is defined as the distance between the first and the last energy loss larger than 1 GeV along the track. The efficiency of the event topology discrimination is shown in Table 6.1.

6.2 Through-Going Muon Tracks

This event selection is optimized for high-energy CC muon neutrinos, arriving from directions with declinations larger than -5° and interacting outside of the detector volume, which lead to long up-going muon tracks inside the detector. Relevant for this thesis is the version of this selection that is applied to four years of data, starting from May 2012 until the end of July 2016.

6.2.1 Muon Level 3

Starting point for this selection are the muon and EHE event streams introduced in Chapter 4. Prior to the actual neutrino level selection, the Muon Level 3 selection is applied. This pre-selection consists of a pre-cut and the actual Muon Level 3 cut. The pre-cut removes events with a total collected charge

smaller than 100 pe and an average charge-weighted minimum distance larger than 90 m; see Eq. (6.3). Moreover, the Muon Filter is reapplied based on the latest successful best-track reconstruction in the seeding chain: line fit, SPE fit, SPE fit with two iterations, and MPE fit; using the analytic parametrization Eq. (5.8) for the likelihood reconstructions. The average charged-weighted minimum distance is calculated with respect to the same best-track reconstruction and all hit non-DeepCore DOMs. The precut is applied before and after the splitting of coincident events, because all previously performed reconstructions are repeated after the splitting. The used splitting algorithm is an improved version of the one used for the MESE selection [126]. It takes the hexagonal geometry of the detector into account and performs several tests after splitting to decide if the event was falsely split and has to be recombined, e.g. due to the ice layer with a high concentration of dust at a depth of about 2 km. The Muon Level 3 cut keeps events with a good reconstruction quality,

$$\frac{(-\log(\mathcal{L}))_{\min}}{n_{\text{ch}} - 5} < 9 \quad \vee \quad \frac{(-\log(\mathcal{L}))_{\min}}{n_{\text{ch}} - 3} < 7.5, \quad (6.4)$$

which is usually given by the minimum negative log-likelihood, here with respect to the likelihood function \mathcal{L} of the best-track reconstruction, scaled by the degree of freedom $n_{\text{ch}} - 5$, where n_{ch} is the number of hit DOMs [121]. Empirically it was found that the scale $n_{\text{ch}} - 3$ can give a better identification of well-reconstructed events. For the events failing this cut, direct pulses due to unscattered photons are exploited as an additional measure for the reconstruction quality:

$$\left(\frac{l_{\text{dir}}}{180 \text{ m}}\right)^2 + \left(\frac{n_{\text{dir}}}{10}\right)^2 > 2 \quad \wedge \quad n_{\text{dir}} > 6, \quad (6.5)$$

where n_{dir} is the number of hit DOMs with direct pulses and l_{dir} the distance along the track from the first to the last hit DOM with direct pulses [121]. The event rate in the northern sky is reduced to below 1 Hz, but still dominated by mis-reconstructed atmospheric muons.

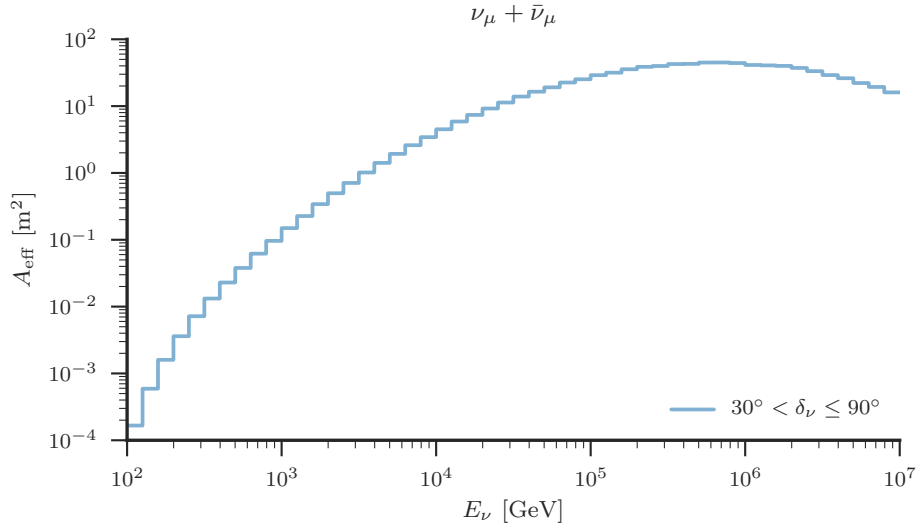


Figure 6.4: Muon neutrino effective area in the declination band used for the search for neutrinos from the 2016 flaring phase of 1ES 1959+650 of the IC86 2012 to 2016 through-going muon track selection.

6.2.2 Neutrino Level Selection

The final neutrino level selection is based on supervised learning with boosted decision trees (BDT) from scikit-learn [127]. The background of atmospheric muons is modeled based on CORSIKA simulations. The signal are simulated CC muon neutrino events with a spline-MPE reconstruction better than 5° , weighted to an isotropic unbroken power-law flux with a benchmark spectral index of $\gamma = 2$. The input variables for the BDT are topological variables like the COG and reconstruction quality parameters like the ones described previously; a complete list of all variables can be found in [121]. A second BDT is trained to separate NC events that would otherwise bias the final energy spectrum; they tend to be reconstructed to very high energies due to the wrong underlying track hypothesis. This background is modeled with simulated electron neutrino events. With this event selection, a neutrino purity of 99.7% is achieved [50]. The effective area of this selection is shown in Fig. 6.4. Relevant for this thesis is the declination band ($30^\circ, 90^\circ$].

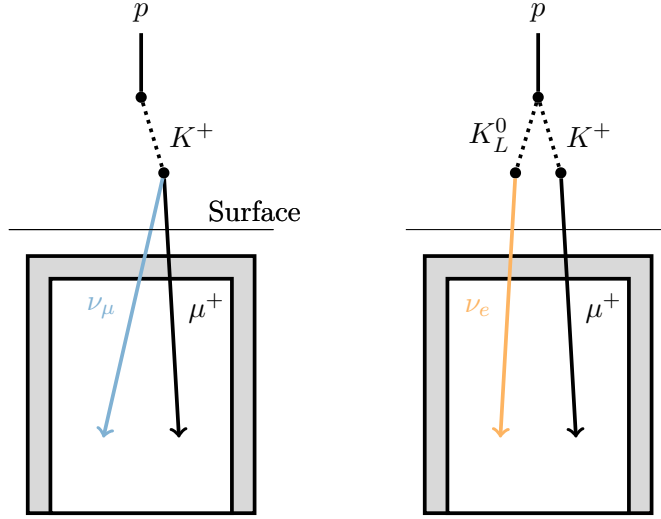


Figure 6.5: Sketch illustrating the correlated (left) and uncorrelated (right) atmospheric neutrino self-veto. Reproduced from [120].

6.3 Vetoing Atmospheric Neutrinos

The active atmospheric muon veto described in Section 6.1 functions also as a veto against atmospheric neutrinos if the down-going neutrino is accompanied by a muon from the same cosmic-ray air shower, which triggers the veto. Whether the muon originates from the same interaction vertex in the cosmic-ray air shower as the neutrino or not, one differentiates between the correlated and uncorrelated atmospheric neutrino self-veto, respectively. The former is only realized for atmospheric muon neutrinos. The veto principle is illustrated in Fig. 6.5.

6.3.1 Correlated Atmospheric Neutrino Self-Veto

The energies of a neutrino-muon pair, E_ν and E_μ , produced in the two-body decay of a meson of type j are related to the parent meson energy E_j via

$$E_j = E_\nu + E_\mu = E_\nu \left(1 + \frac{E_\mu}{E_\nu} \right). \quad (6.6)$$

The active atmospheric muon veto puts a threshold $E_{\mu,\min}$ on the muon energy at production. The differential flux of conventional atmospheric muon neutrinos accompanied by a muon above this threshold is obtained from Eq. (2.14) by replacing the lower energy integration limit with

$$E_{j,\min} = E_\nu \max \left\{ \frac{1}{1 - r_j}, 1 + \frac{E_{\mu,\min}}{E_\nu} \right\}, \quad (6.7)$$

where r_j is the ratio of muon mass squared over meson mass squared. This yields the solution $\tilde{\Phi}_{\nu_\mu + \bar{\nu}_\mu}(E_\nu, E_{\mu,\min})$, which is of the same form as Eq. (2.18), but with the modified factors $A_{j\nu}(E_{\mu,\min})$ and $B_{j\nu}(E_{\mu,\min})$ that can be found in [122]. The passing rate of the correlated atmospheric neutrino self-veto is given by

$$P_{\text{correlated}} = 1 - \frac{\tilde{\Phi}_{\nu_\mu + \bar{\nu}_\mu}(E_\nu, E_{\mu,\min})}{\Phi_{\nu_\mu + \bar{\nu}_\mu}(E_\nu)}. \quad (6.8)$$

The threshold muon energy $E_{\mu,\min}$ is obtained from the parametrization described in [120]. The parametrization is a function of ice overburden X in meters and depends on the median energy $\bar{E}_{\mu,\text{veto}}$ the muon is required to have after penetrating X in order to trigger the veto. The ice overburden in turn depends on the zenith angle and vertical depth. In [120], it is verified that Eq. (6.8) can also be used to describe the passing rate for prompt atmospheric muon neutrinos, produced in the three-body decay of charmed mesons, e.g. $D^+ \rightarrow \bar{K}^0 \mu^+ \nu_\mu$.

6.3.2 Uncorrelated Atmospheric Neutrino Self-Veto

The passing rate of the uncorrelated atmospheric neutrino self-veto is given by

$$P_{\text{uncorrelated}} = \frac{\sum_A \int R_\nu P(N_\mu = 0) dE}{\sum_A \int R_\nu dE}, \quad (6.9)$$

where $P(N_\mu = 0) = \exp(-N_\mu)$ is the Poisson probability that no muons from a cosmic-ray air shower initiated by a primary nucleus of mass A , energy E , and zenith angle ϑ penetrate to the depth of the detector without dropping below

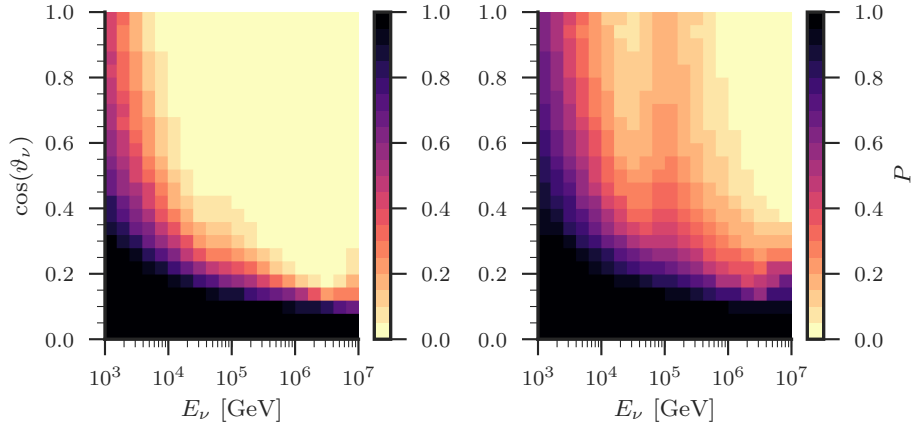


Figure 6.6: Passing fraction of atmospheric neutrino self-veto for simulated MESE events (IC86 2013), weighted to the HKKMS06 (left) and ERS (right) model.

the veto threshold $\bar{E}_{\mu,\text{veto}}$ [123]. The probability depends on the cumulative muon yield N_{μ} evaluated at $E_{\mu,\text{min}}$. The response function

$$R_l(E_l, A, E, \vartheta) = \Phi(A, E) \times \frac{dN_l(E_l, A, E, \vartheta)}{dE_l} \quad (6.10)$$

gives the energy distribution of primary nuclei that produce leptons of type l with energies above E_l . The lepton yield N_l is obtained from the modified Elbert parametrization described in [123]. The primary cosmic-ray flux $\Phi(A, E)$ is taken from the H3a model. The total atmospheric neutrino self-veto passing rate is given by $P_{\text{correlated}} \times P_{\text{uncorrelated}}$, which is a function of neutrino flavor, energy, zenith angle, and depth. In this thesis, veto threshold energies of

$$\bar{E}_{\mu,\text{veto}} = \begin{cases} 100 \text{ GeV} & \tilde{q}_{\text{tot}} \leq 6000 \text{ pe} \\ 1250 \text{ GeV} & \tilde{q}_{\text{tot}} > 6000 \text{ pe} \end{cases} \quad (6.11)$$

are used, depending on the homogenized total charge \tilde{q}_{tot} [120]. The passing fraction is shown in Fig. 6.6.

7 Search for Neutrino Emission in the Galactic Plane

In this chapter, the search for neutrino emission in the Galactic plane is presented. The analysis method is applied to seven years of IceCube data, taken between May 2010 and May 2017, based on the improved MESE selection described in Chapter 6.

7.1 Fit Method

The search for neutrino emission in the Galactic plane is based on a binned forward-folding likelihood fit using templates. A Poisson likelihood,

$$\mathcal{L} = \prod_i \frac{(\mu_{\text{tot},i})^{d_i}}{d_i!} \exp(-\mu_{\text{tot},i}), \quad (7.1)$$

is used, which describes the probability density to observe d_i events in bin i given the expected number of events

$$\mu_{\text{tot},i} = \sum_k \mu_{k,i}(\mathbf{p}_k, \mathbf{n}_k), \quad (7.2)$$

which is the sum over all lepton flux templates k that are considered to describe the experimental data. The templates used for this analysis are listed in Table 7.1. Each template depends on a set of parameters, \mathbf{p}_k and \mathbf{n}_k , the likelihood function is maximized with respect to. Nuisance parameters, which have external constraints, are contained in \mathbf{n}_k . Note that the templates can share parameters. In this analysis, the negative log-likelihood function

$$-\log(\mathcal{L}) = -\sum_i (d_i \log(\mu_{\text{tot},i}) - \mu_{\text{tot},i} + \dots) + \sum_j f_j \quad (7.3)$$

Lepton flux template	Lepton flux model
Atm. muons μ	MuonGun
Conv. atm. neutrinos ν_{conv}	HKKMS06
Prompt atm. neutrinos ν_{prompt}	ERS
Extra-galactic neutrinos ν_{EG}	Isotropic unbroken power law
Galactic neutrinos ν_{gal}	<i>Fermi</i> -LAT, KRA_γ ($E_{\text{cut}} = 50 \text{ PeV}$)

Table 7.1: Lepton flux templates. The atmospheric and Galactic neutrino flux models are introduced in Chapter 2 and Chapter 3, respectively.

is numerically minimized with respect to global flux normalizations c_k for each lepton flux template k , the primary cosmic-ray spectral index $\Delta\gamma_{\text{CR}}$, the relative contribution R_K of kaon decays to the conventional atmospheric neutrino flux, the spectral index γ_{EG} of the extra-galactic neutrino flux, and optionally the spectral index γ_{gal} of the Galactic neutrino flux. More details are given in the following sub-section. The L-BFGS-B algorithm is used for the minimization [128]. The likelihood function can be penalized with prior functions f_j , which arbitrarily increase the negative log-likelihood value. The default choice are Gaussian prior functions,

$$f(n) = \frac{(n - \bar{n})^2}{2\sigma_n^2}, \quad (7.4)$$

which penalize the likelihood function if the nuisance parameter value n the likelihood function is evaluated for significantly differs from the expected value \bar{n} given the uncertainty σ_n on \bar{n} . In general, a prior function can also depend on more than one nuisance parameter if they are correlated. In order to disentangle the different lepton flux contributions, both experimental data and templates are binned along reconstructed energy, arrival direction in equatorial coordinates, and event topology, namely cascade or track-like; see Chapter 5 and Chapter 6 for more details. The directional binning is either rectangular in right ascension and sine declination or based on a HEALPix grid. The detector run seasons, 2010 to 2016, are treated separately and stacked in the likelihood evaluation.

7.1.1 Lepton Flux Templates

The lepton flux template construction is based on simulated neutrino and muon events, which are processed to the final MESE selection level. Primary neutrinos are generated with Neutrino Generator (NuGen)¹, which is based on [129]. The neutrino arrival directions and energies are drawn isotropically and between E_{\min} and E_{\max} from an unbroken power law, respectively. The neutrino flavor is pre-chosen and NuGen generates half neutrinos and half anti-neutrinos. A cylindrical detection volume is defined that encloses the detector. For each generated event, the cylinder is projected onto a plane whose normal is inclined with respect to the drawn zenith angle. The neutrino is propagated from the Earth's surface to a random intersection point that is sampled on this area. In each propagation step Δx , it is decided if the neutrino interacts with the nucleons or electrons in the Earth. The interaction probability is given by

$$P_{\text{int}} = 1 - \exp(-\Delta x \sigma n), \quad (7.5)$$

where σ is the total interaction cross section and n the number density of targets. For electron and muon neutrinos, CC interactions are suppressed, which would otherwise lead to absorption. A final neutrino is randomly chosen from all candidates, including the primary and all secondary neutrinos, that reach the detection volume. This neutrino is forced to interact inside the detection volume. The interaction point is drawn uniformly in column depth. A simulation weight is assigned that accounts for the described efficiency biases and contains the inverse of the differential fluence

$$\Phi^* \equiv \Phi \times \Delta t = \frac{d^3 N}{dE dA d\Omega}, \quad (7.6)$$

which gives the number of generated particles N per energy interval dE , area dA , and solid angle $d\Omega$. The simulation weight times a differential neutrino flux weight gives the contribution of this event to the expected event rate. For each neutrino flux template, the neutrino simulation is weighted to the corresponding neutrino flux model, as listed in Table 7.1. The con-

¹ <http://code.icecube.wisc.edu/svn/projects/neutrino-generator/>

ventional and prompt atmospheric neutrino flux weights are multiplied with the corresponding passing fraction of the atmospheric neutrino self-veto; see Chapter 6. In [120], it is shown that the background of atmospheric muons is dominated by single muons and that the contribution from muon bundles can be neglected. The background of single atmospheric muons is modeled with MuonGun², which draws events from parametrized atmospheric muon fluxes, as described in [120]. The parametrizations are obtained from full CORSIKA simulations. MuonGun allows one to re-weight the simulation to different primary cosmic-ray and hadronic interaction models. For this analysis, H4a and SIBYLL 2.1 are used, respectively. The event generation is followed by the lepton propagation and shower simulation, the photon propagation, the detector response simulation, and the online processing and filtering.

The weighted lepton simulations are binned along the observables described before and along true lepton energy, cosine zenith angle, and enumerated lepton flavor and type, following the particle numbering scheme from [38]. The last three axes are used for re-weighting, which is explained in Section 7.1.3. These weighted multi-dimensional histograms are referred to as lepton flux templates. They are shown in Fig. 7.1 and Fig. 7.2. The shown binning corresponds to the one used in the likelihood fit. The pixel resolutions in Fig. 7.2 are about 29.3° and 7.3° for cascade and track-like events, respectively. The binning is chosen according to the median resolutions shown in Fig. 5.2 and Fig. 5.3. For track-like events, a coarser directional binning than the median resolution is chosen in order to guarantee that the MC statistic in each declination band is high enough that the uncertainty on the number of MC events per bin can be neglected. The disentanglement of the Galactic neutrino flux component is based on the expected anisotropy in the neutrino arrival direction and the softer energy spectrum compared to the extra-galactic neutrino flux component. This analysis is mostly sensitive to cascade-like events from the direction of the Galactic plane in the southern sky. The strongest sensitivity is expected from the bins containing the Galactic Center region. The northern sky is mostly used to constrain the other neutrino flux components.

² <http://code.icecube.wisc.edu/svn/projects/MuonGun/>

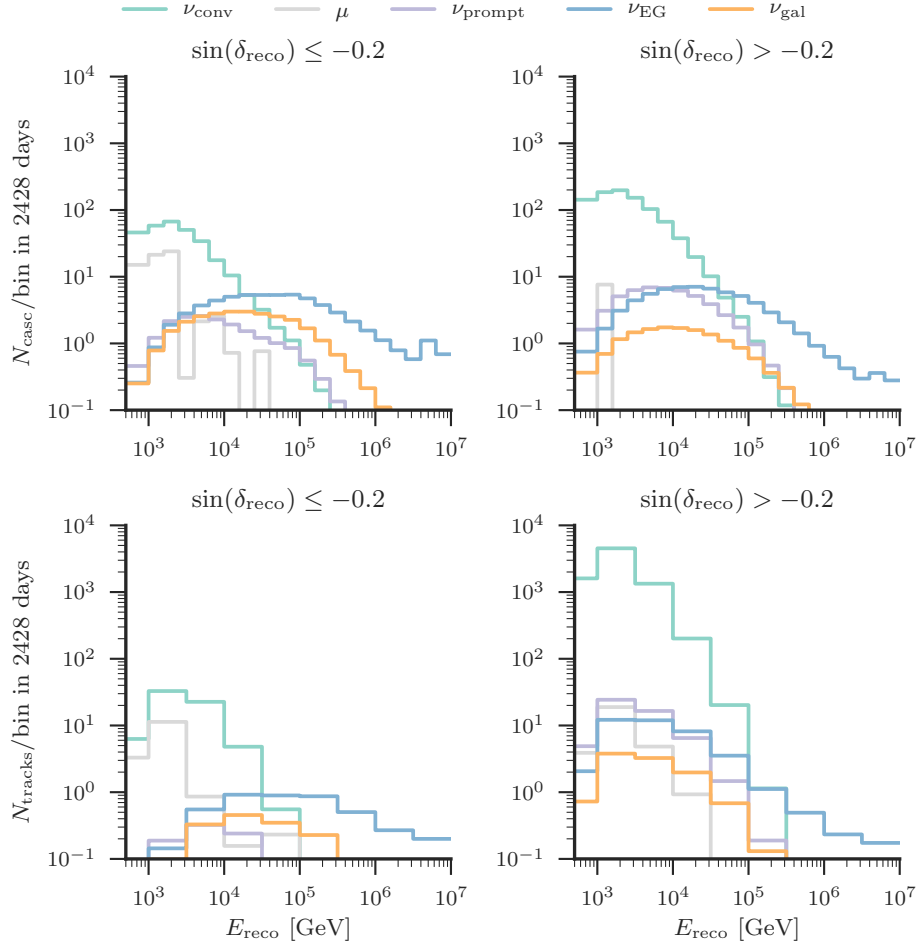


Figure 7.1: Lepton flux templates projected along reconstructed energy in the southern (left) and northern (right) sky, summed over reconstructed arrival direction and detector season. Top and bottom row show cascade and track-like events, respectively. The Galactic neutrino flux template is weighted to the KRA_γ model. The extra-galactic and atmospheric prompt neutrino flux templates are weighted to the best-fit astrophysical neutrino flux and upper limit on ERS reported in [50, 51], respectively; see Chapter 3.

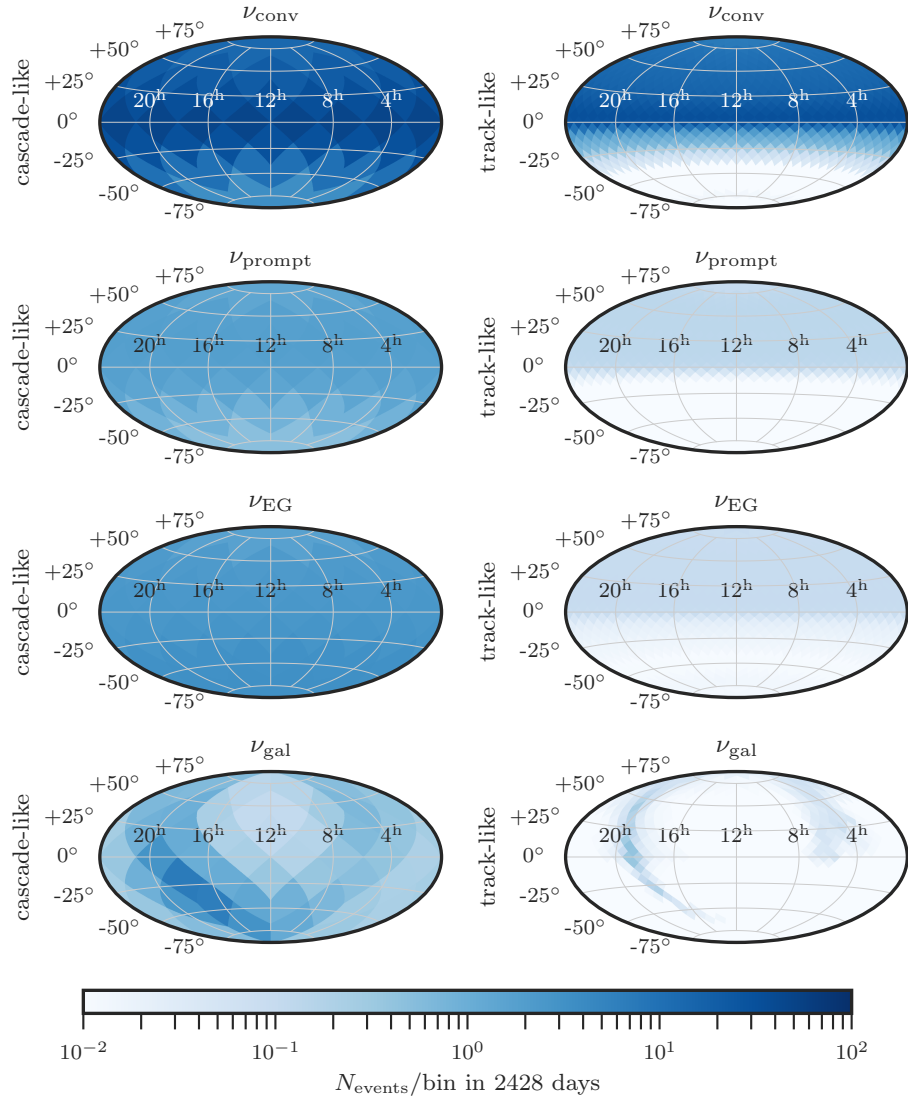


Figure 7.2: Neutrino flux templates projected along reconstructed arrival direction, summed over reconstructed energy and detector season. Same input as for Fig. 7.1.

7.1.2 Re-Sampling in Right Ascension

Because of the flat detector acceptance in right ascension, the simulated lepton events can be re-sampled in this observable. The Galactic neutrino flux template is averaged over 10^4 re-sampling trials. For each trial, the simulated lepton events are assigned random true right ascension values, which are used to calculate flux weights given the Galactic neutrino flux model. The position of the detector is approximated to be exactly at the Geographic South Pole. Under this assumption, the absolute value of the difference between true and reconstructed azimuth angle is invariant under the transformation from local to equatorial coordinates and used to assign reconstructed right ascension values to the simulated lepton events given the drawn true right ascension values. Using these reconstructed right ascension values and the flux weights, the Galactic neutrino flux template for this particular re-sampling trial is constructed. The Galactic neutrino flux template is summed over all re-sampling trials and divided by the number of trials. In case the binning in reconstructed arrival direction is based on a HEALPix grid, the same procedure is also applied to all other lepton flux templates. Because the corresponding lepton flux models do not depend on right ascension, the flux weights need only to be calculated once. In case of a rectangular binning, the simulated lepton events are not binned along reconstructed right ascension. Instead, the resulting histograms are copied along the bins in reconstructed right ascension and down-scaled by the number of bins.

7.1.3 Fit Parameters

The expectations $\mu_{k,i}$ per bin i from each lepton flux template k are scaled with a global flux normalization c_k . The extra-galactic and the *Fermi*-LAT neutrino flux templates depend on the spectral indices of the underlying power laws. The conventional and prompt atmospheric neutrino flux templates depend on the primary cosmic-ray flux and thus on the primary cosmic-ray spectral index; compare Eq. (2.18). This nuisance parameter is implemented as a residual $\Delta\gamma_{\text{CR}}$ relative to the model prediction. The expected value is $\Delta\gamma_{\text{CR}} = 0$ and an uncertainty of $\sigma_{\Delta\gamma_{\text{CR}}} = 0.05$ is used as a prior. The conventional

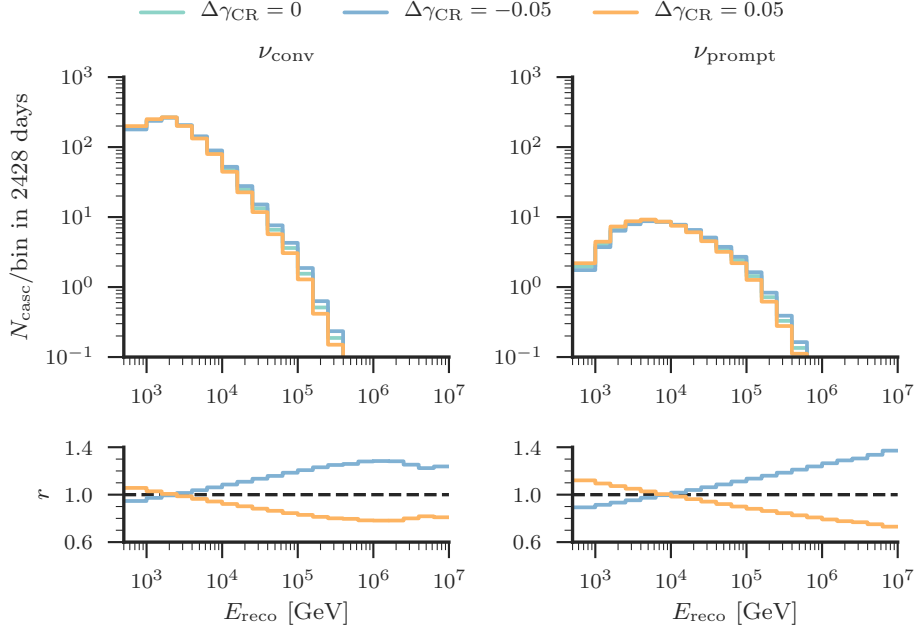


Figure 7.3: Effect of fit parameter primary cosmic-ray spectral index $\Delta\gamma_{\text{CR}}$ on the conventional (left) and prompt (right) atmospheric neutrino flux templates along reconstructed energy. The bottom plots show the ratio with respect to the baseline $\Delta\gamma_{\text{CR}} = 0$.

and prompt atmospheric neutrino flux templates are weighted to a different primary cosmic-ray spectral index by scaling it with

$$w_i^k(\Delta\gamma_{\text{CR}}) = \left(\frac{E_i}{\bar{E}_k} \right)^{-\Delta\gamma_{\text{CR}}}, \quad k \in \{\text{conv}, \text{prompt}\} \quad (7.7)$$

along the true neutrino energy E_i axis, normalized at the median neutrino energy \bar{E}_k . This way, the expected total number of events stays roughly constant and artificial degeneracies with the flux normalizations are reduced. The median neutrino energies are calculated before accounting for the atmospheric neutrino self-veto. Fig. 7.3 shows how the primary cosmic-ray spectral index affects the conventional and prompt atmospheric neutrino flux templates. Positive and negative $\Delta\gamma_{\text{CR}}$ values soften and harden the reconstructed energy

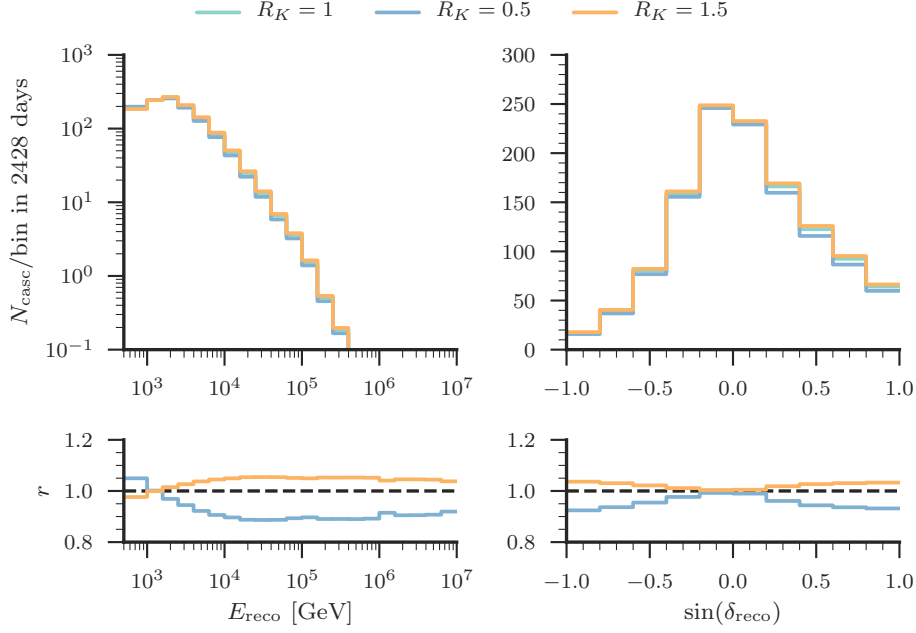


Figure 7.4: Effect of fit parameter relative contribution R_K of kaon decays to the conventional atmospheric neutrino flux on the conventional atmospheric neutrino flux template along reconstructed energy (left) and sine declination (right). The bottom plots show the ratio with respect to the baseline $R_K = 1$.

spectra, respectively. The implementation of the conventional atmospheric neutrino flux model described in Chapter 2 allows to independently rescale the pion and kaon terms; compare Eq. (2.18). As outlined, the latter dominates above TeV energies. The corresponding flux template is rescaled with

$$w_{ijl}^{\text{conv}}(R_K) = \frac{N_{\text{conv}}(R_K = 1)}{N_{\text{conv}}(R_K)} \frac{\Phi_{\nu_l}^{\text{conv}}(E_i, \cos(\vartheta)_j; R_K)}{\Phi_{\nu_l}^{\text{conv}}(E_i, \cos(\vartheta)_j; R_K = 1)} \quad (7.8)$$

along the true neutrino energy E_i , cosine zenith angle $\cos(\vartheta)_j$, and flavor and type l axes, where R_K is the relative contribution of kaon decays. The baseline is $R_K = 1$ and an uncertainty of $\sigma_{R_K} = 0.1$ is used as a prior. The

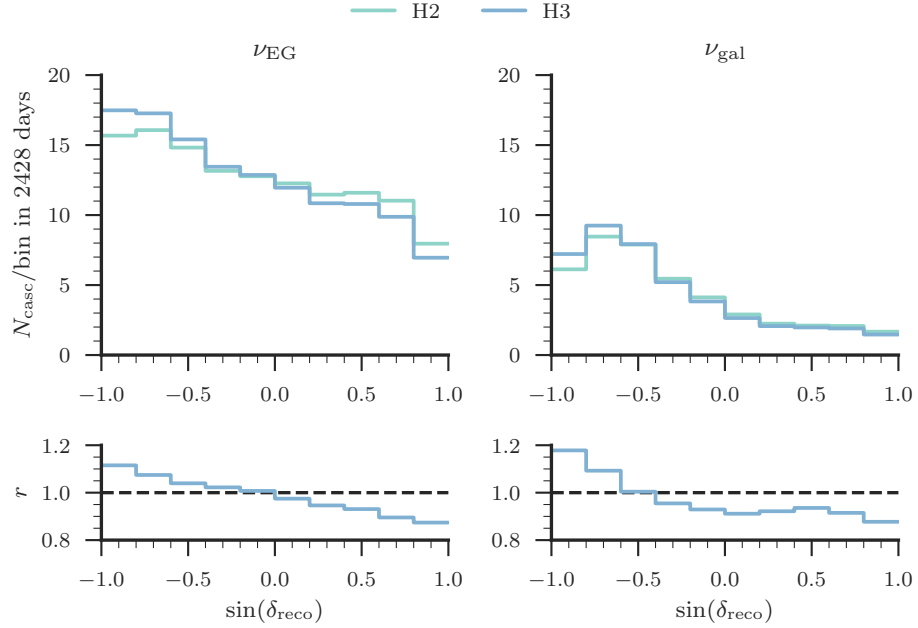


Figure 7.5: Effect of hole ice model on the extra-galactic (left) and Galactic (right) neutrino flux templates along reconstructed sine declination. The bottom plots show the ratio with respect to the baseline model H2.

expected total number N_{conv} of conventional atmospheric neutrino events is kept constant. As for the cosmic-ray spectral index, the motivation is to reduce an artificial degeneracy with the flux normalization. Fig. 7.4 shows that a smaller R_K value leads to more expected events at lower energies, where pion decays still contribute. In the kaon-decay-dominated energy range, a more or less constant reduction is expected. The expected decrease along the sine declination bins reflects the $\cos^{-1}(\vartheta)$ dependency in Eq. (2.18). The cascade to track-like ratio is also reduced because kaon decays are the dominant source of conventional atmospheric electron neutrinos. The hole ice model is treated as a discrete nuisance parameter. As illustrated in Fig. 7.5, more and less events are expected from the southern and northern sky for H3 with respect to the baseline model H2, respectively.

7.2 Likelihood-Ratio Test

The first goal of this analysis is to exclude the null-hypothesis of only one isotropic astrophysical neutrino flux component, which is the special case $c_{\text{gal}} = 0$ of the alternative hypothesis, which includes the contribution from neutrino emission in the Galactic plane. The test statistic

$$t \equiv 2 \log \left(\frac{\mathcal{L}(\hat{c}_{\text{gal}}, \hat{\gamma}_{\text{gal}}, \dots)}{\mathcal{L}(c_{\text{gal}} = 0, \dots)} \right) \quad (7.9)$$

is defined, where \hat{c}_{gal} and $\hat{\gamma}_{\text{gal}}$ are the Galactic flux normalization and spectral index that minimize the negative log-likelihood function, respectively; not shown are the other best-fit parameter values under each hypothesis. The compatibility of the observed test statistic value t_{obs} with the null-hypothesis is quantified via the p-value

$$P_0(t_{\text{obs}}) \equiv \int_{t_{\text{obs}}}^{\infty} p_0(t) dt, \quad (7.10)$$

where $p_0(t) = p(t; c_{\text{gal}} = 0, \dots)$ is the test statistic distribution under the null-hypothesis. For fixed Galactic spectral indices, this distribution is expected to be described by a mixture of half a χ^2 -distribution with a degree of freedom (ndf) of one and half a delta distribution at $t = 0$ [130]; see Fig. 7.6.

7.3 Sensitivity and Discovery Potential

The sensitivity and discovery potential of this analysis with respect to neutrino emission in the Galactic plane is quantified by quoting the Galactic neutrino flux normalizations c_{gal} that solve

$$\int_{t_\alpha}^{\infty} p(t; c_{\text{gal}}, \dots) dt \stackrel{!}{=} \beta, \quad (7.11)$$

where β values of 90% and 50% are chosen; the threshold test statistic values t_α correspond to $P_0(t_\alpha) = 0.5$ and $P_0(t_\alpha) \approx 1.35 \times 10^{-3}$ (3σ), re-

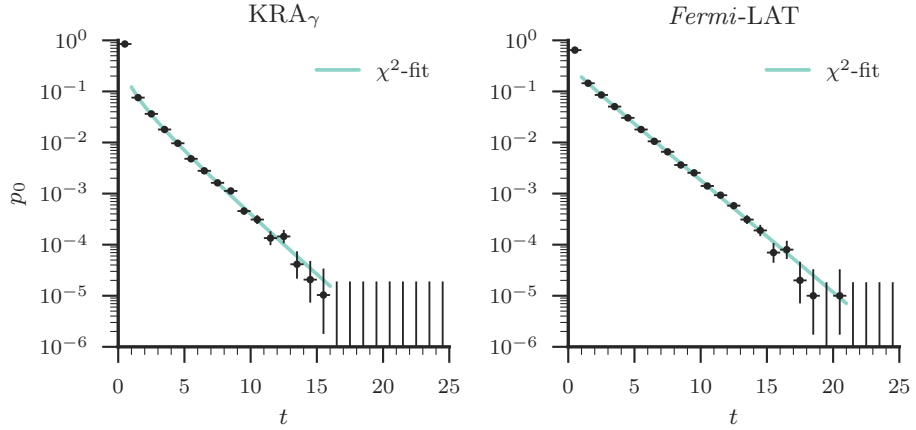


Figure 7.6: Test statistic distribution under the null-hypothesis, fitted with a χ^2 -distribution. More information can be found in the text.

spectively; see Table 7.2. The test statistic distributions are obtained from pseudo-experiments. The pseudo-experiments are created by drawing random bin entries from Poisson distributions with mean expected numbers $\mu_{\text{tot},i}$ of events per bin i . If not stated otherwise, the extra-galactic neutrino flux template is weighted to the best-fit differential muon plus anti-muon neutrino flux presented in Chapter 3, assuming a neutrino flavor ratio of 1:1:1. The through-going muon track sample is restricted to the northern sky and mostly sensitive to neutrinos of extra-terrestrial origin with energies above 100 TeV. Thus, the measured astrophysical neutrino flux should be dominantly of extra-galactic origin. Moreover, an atmospheric prompt neutrino flux normalization of $c_{\text{prompt}} = 1.06$ is assumed. For all other nuisance parameters, the baseline values are used. Fig. 7.6 shows the test statistic distribution under the null-hypothesis. As expected, the distribution of test statistic values larger than zero is compatible with half a χ^2 -distribution with a ndf of one for the KRA_γ template; a fit yields a scale of 0.52 ± 0.02 and a ndf of 0.94 ± 0.03 . The *Fermi*-LAT template depends also on the fitted Galactic spectral index, which is degenerated with the Galactic neutrino flux normalization. The distribution of test statistic values larger than zero is well-described by a χ^2 -distribution

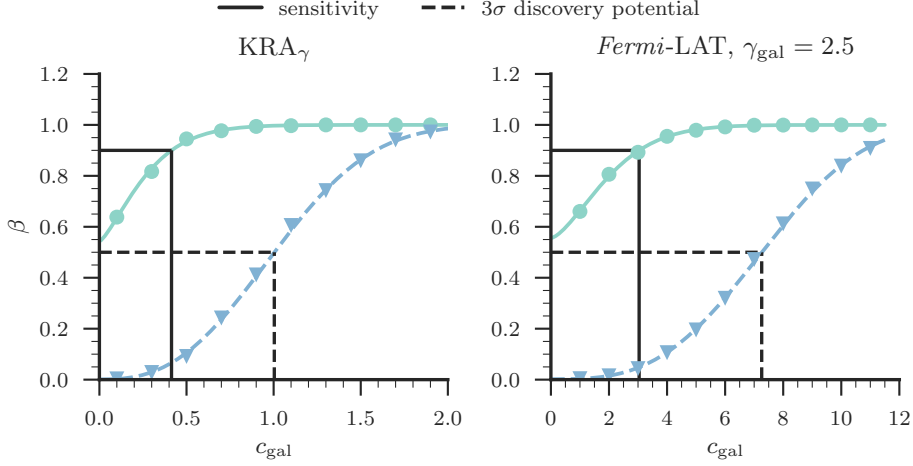


Figure 7.7: Sensitivity and discovery potential of this analysis to the KRA_γ model and to the *Fermi*-LAT model for a benchmark Galactic spectral index of $\gamma_{\text{gal}} = 2.5$, respectively. The interpolation between the points is based on the parametrization $1 - a \exp(-(bx)^c)$.

with a scale of 0.63 ± 0.01 and a ndf of 1.87 ± 0.02 . The threshold test statistic values are calculated from the generated trials instead of using the fitted χ^2 -distributions. For the sensitivity and discovery potential estimation, pseudo-experiments are created for a range of Galactic neutrino flux normalizations. For each scan point, the fractions of trials with fitted statistic values larger than t_α are determined. Scans for the KRA_γ model and the *Fermi*-LAT model with a reference spectral index of $\gamma_{\text{gal}} = 2.5$ are shown in Fig. 7.7. By following the solid and dashed black lines, one can read off the sensitivity and discovery

	KRA_γ	<i>Fermi</i>-LAT
$(t_\alpha)_{\text{sens}}$	1.96×10^{-5}	0.38
$(t_\alpha)_{\text{disc}}$	8.77	11.97
$(c_{\text{gal}})_{\text{sens}}$	0.41	3.04
$(c_{\text{gal}})_{\text{disc}}$	1.00	7.26

Table 7.2: Sensitivity and discovery potential obtained from Fig. 7.7.

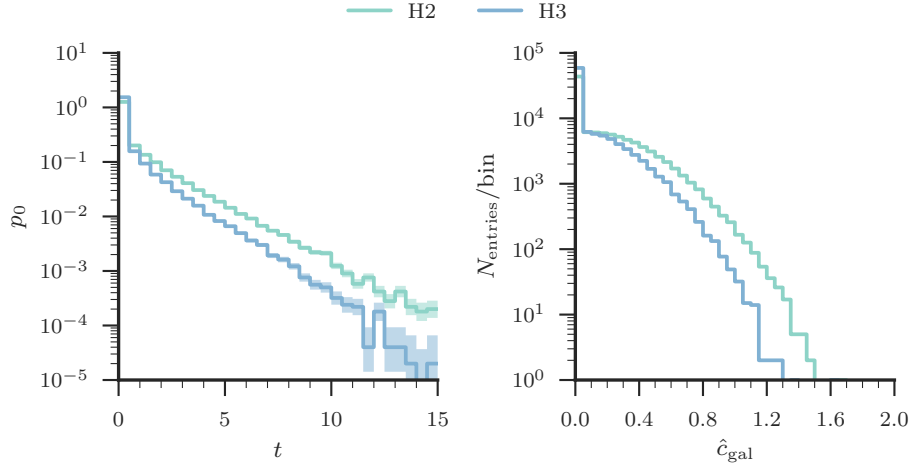


Figure 7.8: Test statistic distribution (left) and distribution of best-fit Galactic flux normalizations (right) under the null-hypothesis for the KRA_γ model. The pseudo-experiments are created using the H3 MC datasets. Likelihood fits are performed with the H2 and the H3 MC datasets, respectively.

potential Galactic neutrino flux normalizations from the x-axis, respectively. The values are shown in Table 7.2. The power-law energy spectrum that enters the *Fermi*-LAT model is normalized at 100 TeV,

$$\Phi_{\nu+\bar{\nu}}(E_\nu) = c_{\text{gal}} \times 10^{-18} \text{ GeV}^{-1} \text{ cm}^{-2} \text{ s}^{-1} \left(\frac{E_\nu}{100 \text{ TeV}} \right)^{-\gamma_{\text{gal}}}, \quad (7.12)$$

where $\Phi_{\nu+\bar{\nu}}$ is integrated over the entire sky. The KRA_γ sensitivity corresponds to about 17 cascade and 4 track-like events in total; 9 out of the 17 cascade-like events are expected to arrive from the southern sky, $\sin(\delta_{\text{reco}}) \leq -0.2$, while the track-like events are all up-going. Fig. 7.8 shows how both the test statistic distribution and the distribution of best-fit Galactic neutrino flux normalizations under the null-hypothesis are shifted to higher values if pseudo-experiments that are created using the H3 MC datasets are fitted with the H2 model. As shown in Fig. 7.5, more events are expected to arrive from the southern sky for the H3 model with respect to the H2 model. When using

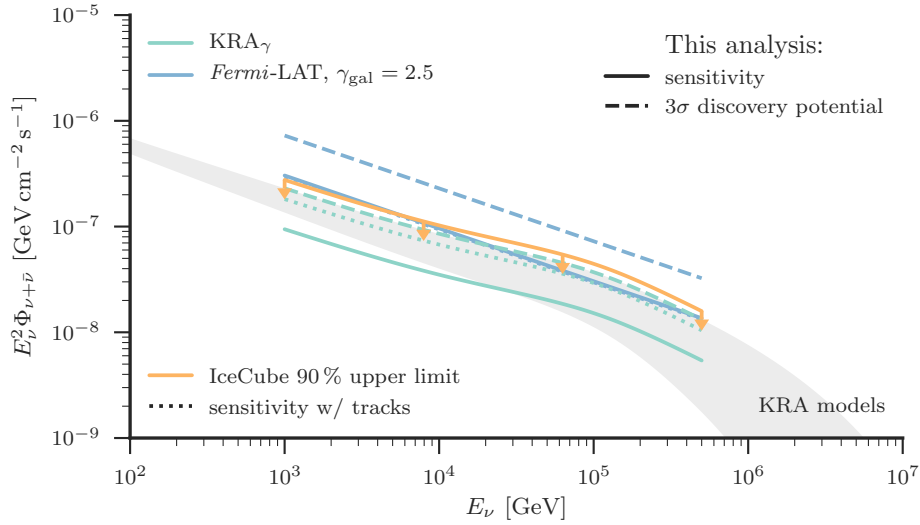


Figure 7.9: Comparison of the sensitivity of this analysis to the published IceCube results with seven years of through-going muon tracks [55]. The plot shows the predicted differential per-flavor neutrino plus anti-neutrino fluxes, multiplied with the sensitivity and discovery potential Galactic neutrino flux normalizations and integrated over the entire sky. The gray area shows the envelope between the minimum and maximum KRA prediction shown in Fig. 3.4.

the H2 model for the likelihood fit, the minimizer tries to compensate this mismatch by fitting a higher Galactic neutrino flux. The expected median test statistic value under the null-hypothesis is about 0.13. Hence, fitting the wrong hole ice model does not mimic a signal from the Galactic plane under the given assumptions. Similar sensitivity and discovery potential Galactic neutrino flux normalizations are obtained to the ones shown in Table 7.2; the deviations are within a few percent. Nevertheless, the test shows that the hole ice has a non-negligible impact on the final p-value estimation. In Fig. 7.9, the benchmark sensitivity of this analysis is compared to the latest published IceCube result with seven years of through-going muon tracks [55]. Given the assumptions made for this sensitivity study, the results for the *Fermi-LAT* model are almost the same. An improvement of about a factor of two is ex-

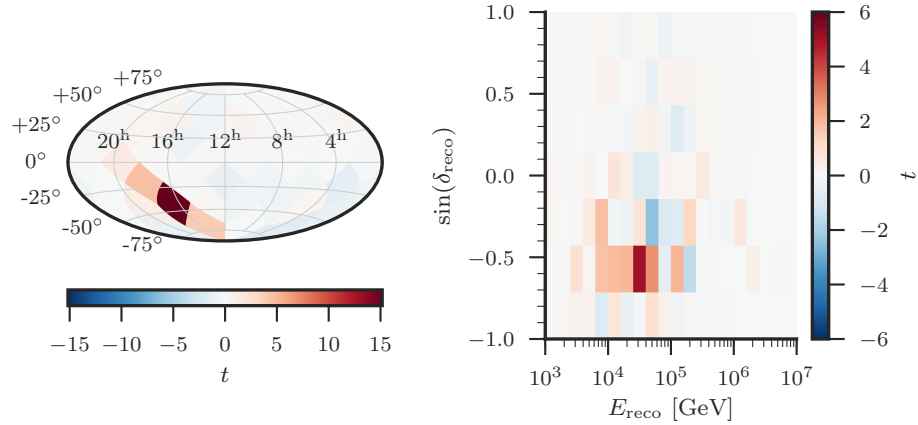


Figure 7.10: Expected test statistic distribution along the analysis bins for the KRA_γ template, projected along reconstructed direction (left) in equatorial coordinates and along reconstructed sine declination versus reconstructed energy (right). The likelihood fit is performed using an Asimov dataset with an injected Galactic neutrino flux normalization of $c_{\text{gal}} = 1$ [130]. For bins with positive test statistic values, the alternative hypothesis is preferred over the null-hypothesis and vice versa. Only cascade-like events are shown because their contribution to the significance dominates.

pected for the KRA_γ model. This finding reflects the stronger neutrino flux prediction of the KRA_γ model towards the inner Galaxy with respect to the *Fermi*-LAT model. This region in the sky is not covered by the through-going muon track analysis. It also shows how important the atmospheric neutrino self-veto is for this search and that a good understanding of the veto probabilities is necessary. Fig. 7.10 shows that the analysis bins along the Galactic plane close to the Galactic Center are expected to contribute the most to the sensitivity of the presented analysis. Moreover, the most sensitive bins in reconstructed energy are around 30 TeV. In conclusion, Galactic neutrino emission is expected to help explaining part of the mismatch between experimental data and MC shown in Fig. 3.2. In Fig. 7.11, it is shown how the sensitivity and discovery potential of this analysis change if the injected extra-galactic

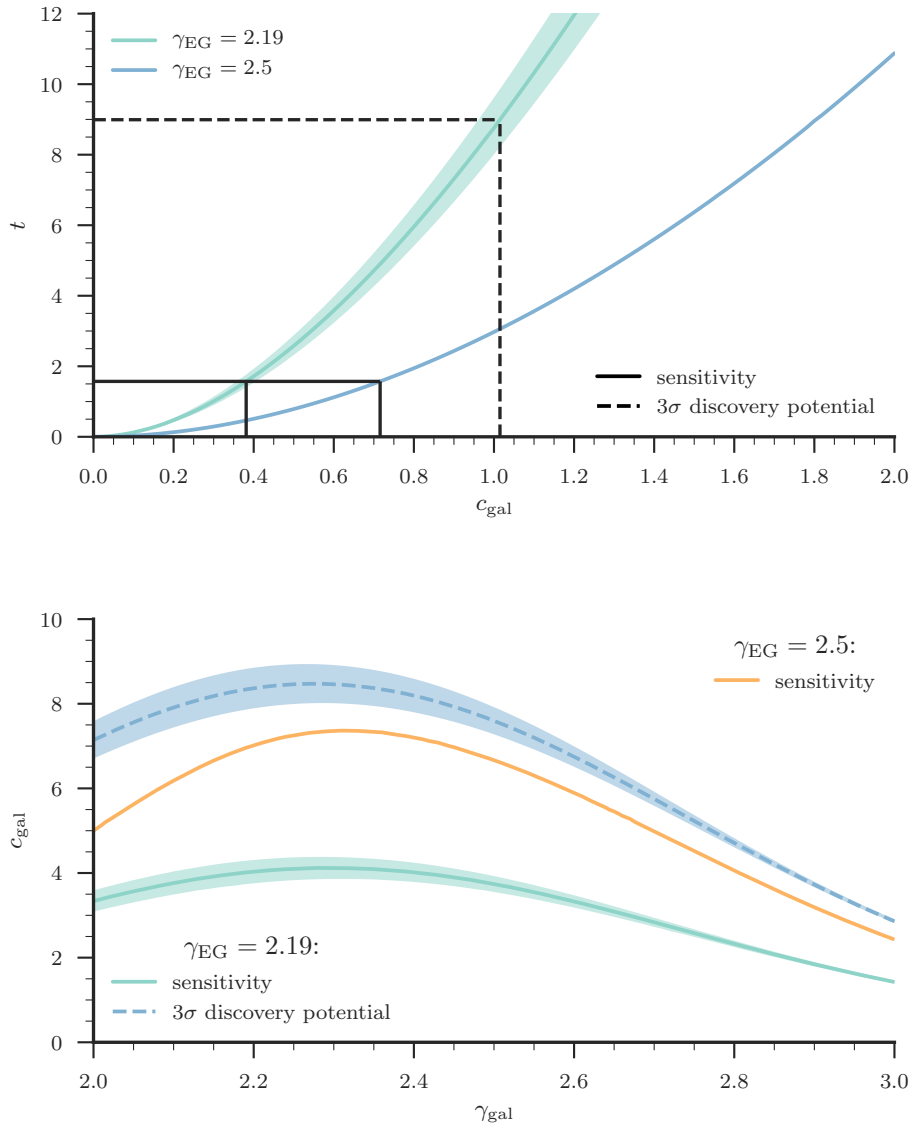


Figure 7.11: Top: fitted test statistic values versus injected Galactic neutrino flux normalization for the KRA_γ model. Bottom: sensitivity and discovery potential Galactic neutrino flux normalizations versus injected Galactic spectral index for the *Fermi*-LAT model. Extra-galactic neutrino fluxes with different spectral indices are injected. Asimov datasets are used. More details are given in the text.

neutrino flux normalization is varied within its uncertainties, see Eq. (3.4), or if a softer energy spectrum of $\gamma_{\text{EG}} = 2.5$ is assumed, which corresponds to the best-fit astrophysical neutrino flux obtained in [131]. For the latter case, the sensitivity is only shown. In the top plot, the sensitivity and discovery potential can be read off from the x-axis by following the solid and dashed lines, respectively. The bottom plot shows the sensitivity and discovery potential for the *Fermi*-LAT model as a function of the injected Galactic spectral index. For performance reasons, Asimov datasets are used for Fig. 7.11, which give an estimate of the median test statistic value without the need to create pseudo-experiments [130]. Hence, a different definition of sensitivity is required: the Galactic flux normalization is quoted that solves Eq. (7.11) for $\beta = 0.5$, using the threshold test statistic values $t_\alpha = 1.57$ and $t_\alpha = 3.45$ for the KRA_γ and *Fermi*-LAT model, respectively. These values correspond to $P_0(t_\alpha) = 0.1$ and are calculated from the trials that enter Fig. 7.6. The uncertainties on the extra-galactic neutrino flux normalization result in the shaded bands around the test statistic, sensitivity, and discovery potential lines. The aforementioned threshold test statistic values are assumed. In general, the sensitivity decreases if an extra-galactic neutrino flux with a softer spectrum is assumed; more events of extra-galactic origin are expected at lower energies and thus the signal-to-background ratio gets smaller. However, one has to keep in mind that the uncertainties on the best-fit astrophysical neutrino flux obtained in [131] are still very large. The sensitivity to the *Fermi*-LAT model improves if the injected Galactic spectral index differs significantly from the injected extra-galactic spectral index.

7.4 Additional Tests based on the Goodness-of-Fit

In order to quantify how well the experimental data is described by the best-fit alternative hypothesis, which includes the contribution from cosmic-ray induced neutrino emission in the Galactic plane, the p-value

$$P_{\text{GOF}} \equiv \int_{\tilde{t}_{\text{obs}}}^{\infty} p(t; \hat{c}_{\text{gal}}, \dots) dt \quad (7.13)$$

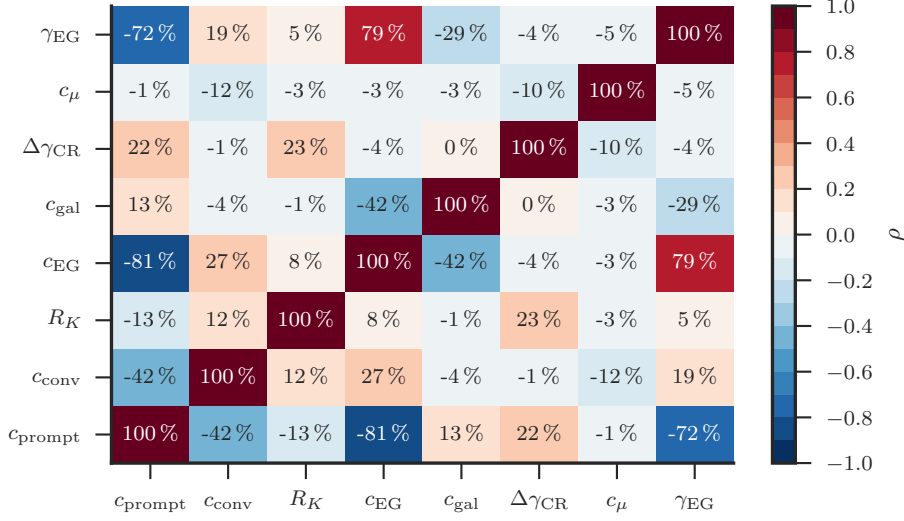


Figure 7.12: Expected correlation coefficient ρ between fit parameters under the alternative hypothesis for the KRA_γ model. An Asimov dataset is fitted with an injected Galactic neutrino flux normalization of $c_{\text{gal}} = 1$.

will be reported after unblinding, which is referred to as the *goodness-of-fit*. The test statistic \tilde{t} corresponds to two times the negative log-likelihood ratio with respect to the *saturated* Poisson model $\mathcal{L}|_{\mu_{\text{tot},i}=d_i, \forall i}$; see Eq. (7.1). The test statistic distribution $p(\tilde{t}; \hat{c}_{\text{gal}}, \dots)$ under the best-fit alternative hypothesis \hat{c}_{gal} is expected to follow a χ^2 -distribution with a ndf of number of bins minus number of fitted parameters [38]. Thus, a good description of the experimental data should yield a p-value of $P_{\text{GOF}} = 0.5$. As shown in Fig. 7.12, the fitted Galactic and extra-galactic neutrino flux normalizations are still expected to be quite strongly degenerated; a correlation factor of $\rho \approx -0.4$ is obtained when fitting a KRA_γ Asimov dataset. Therefore, it is also planned to compute a goodness-of-fit p-value with a prior on the extra-galactic neutrino flux included. The result of the profile likelihood scan in astrophysical neutrino flux normalization versus astrophysical spectral index of the through-going muon track analysis with eight years of data will be taken as the prior

function [51]. This p-value will be compared to the standard null-hypothesis, $c_{\text{gal}} = 0$, which does not include a prior on the extra-galactic neutrino flux. A more qualitative approach to the expected outcome of this comparison is shown in Fig. 7.13. An Asimov dataset that includes the KRA_γ prediction for a Galactic neutrino flux normalization of $c_{\text{gal}} = 1$ is fitted under the null-hypothesis and the agreement of the fit result with the Asimov dataset along the fit observables is illustrated. The minimizer tries to account for the additional Galactic events at medium energies by preferring a softer extra-galactic neutrino flux than injected; an extra-galactic spectral index of $\hat{\gamma}_{\text{gal}} \approx 2.30$ is fitted, while the injected one is $\gamma_{\text{gal}} = 2.19$. This leads to a disagreement between experimental data and expectation at higher energies. Unfortunately, this is the energy range where the least events are expected to be measured. The mismatch between the experimental data and the best-fit null-hypothesis along reconstructed sine declination is also expected to be not pronounced enough. The strongest mismatch is expected to arise along reconstructed right ascension. In conclusion, the goodness-of-fit p-values for the best-fit null and alternative hypotheses are not expected to differ significantly.

7.5 Unblinding Status

In December 2017, the IceCube Collaboration granted the unblinding of the presented analysis. Preliminary results were obtained based on the KRA_γ model: a mild over-fluctuation of the experimental data with respect to the expectation is observed. The interpretation of this over-fluctuation is non-trivial and requires more detailed studies on systematic uncertainties. These studies are still on-going. A publication of the final results is planned in the near future together with other analyses that are based on the MESE sample that is presented in this thesis.

Depending on the outcome of the on-going studies on systematic uncertainties, different conclusions could be drawn: either the over-fluctuation is caused by these systematic uncertainties; or the over-fluctuation persists and grows adding more statistics; then it can be interpreted as a deviation of the experimental data from the null-hypothesis, which includes only a single isotropic

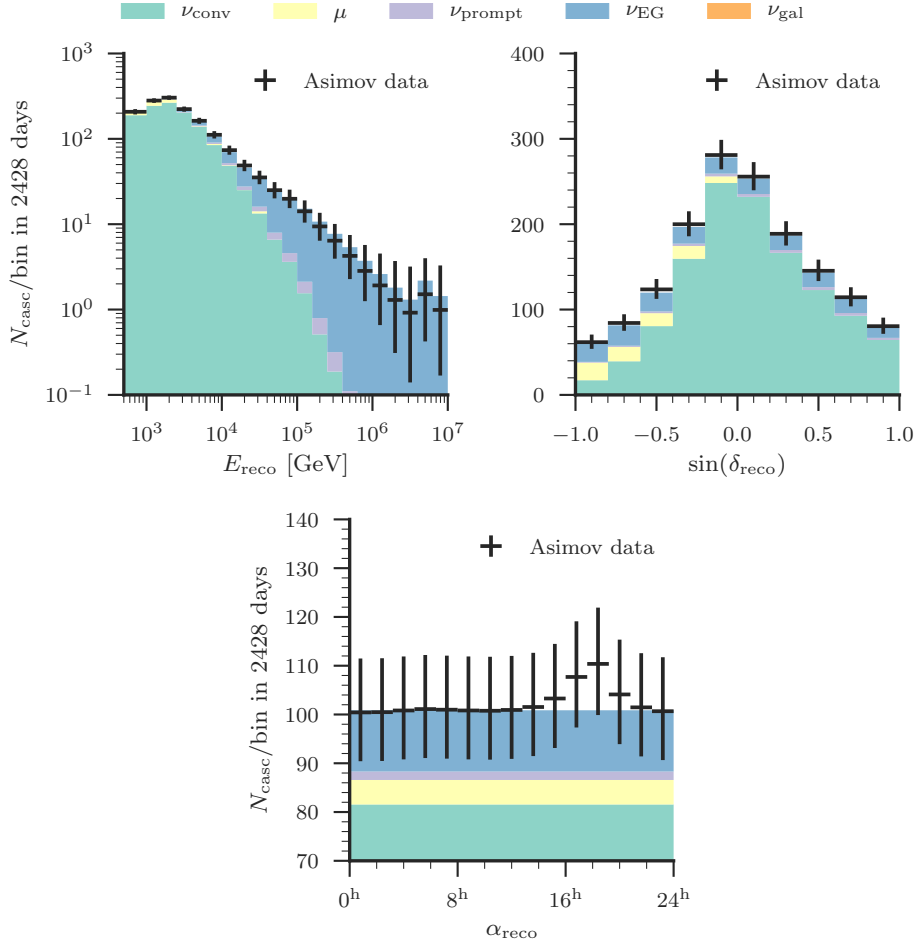


Figure 7.13: Expected agreement between experimental data and the best-fit null-hypothesis projected along reconstructed energy, sine declination, and right ascension, respectively. An Asimov dataset is fitted with an injected Galactic neutrino flux normalization of $c_{\text{gal}} = 1$. For the shown uncertainties, the Neyman construction is used, assuming a Poisson distribution with a mean that corresponds to the expected number of bin entries [38]. The best-fit MC lepton flux templates are stacked. Only cascade-like events are exemplary shown.

neutrino flux component of astrophysical origin. In the former scenario, a 90 % Neyman limit will be calculated for the KRA_γ model [38]. This limit corresponds to the flux normalization c_{gal} that solves Eq. (7.11) for $t_\alpha = t_{\text{obs}}$ and $\beta = 90\%$. If a value smaller than one is obtained, this analysis will constrain the KRA_γ model. This constraint can be translated into limits on the physics parameters that enter the KRA_γ model, but requires full access to the underlying simulation of cosmic-ray propagation with the DRAGON solver. In the latter scenario, the next step will be to quantify how well the alternative hypothesis, which contains the contribution from cosmic-ray induced neutrino emission in the Galactic plane, describes the experimental data based on the goodness-of-fit as outlined in Section 7.4.

In Fig. 7.14, some of the open questions are emphasized that are still under investigation. First, most searches for point-like neutrino sources in the sky with IceCube create pseudo-experiments under the null-hypothesis by scrambling the experimental data in right ascension; see Chapter 8. For this analysis, this procedure is not fully applicable, because it does not reproduce the expected energy and declination distributions under the null-hypothesis. However, it is still a useful crosscheck for the robustness of the p-value that is obtained from the standard MC-based approach, which is described in Section 7.3. As shown in Fig. 7.14, the test statistic distribution under the null-hypothesis, which is obtained from the scrambles, strongly deviates from the expected χ^2 -distribution if the H2 model is used for the likelihood fit. In case of the H3 model, the deviation is less pronounced and can be further decreased if the fit is performed with a KRA_γ -like template with an unbroken power-law energy spectrum that is assigned the same spectral index as the extra-galactic neutrino flux template. This effectively removes the energy information from the test statistic. For the H2 model, a significant deviation remains. Secondly, the baseline photon tables used for the directional and energy reconstructions do not account for the observed anisotropy of the South Pole ice; see Chapter 4. After the sensitivity study for this analysis was completed and unblinding was granted, the author's attention was directed to reprocessed experimental data and MC simulations with fairly new photon tables for the cascade reconstructions that have the anisotropy incorporated. As shown in

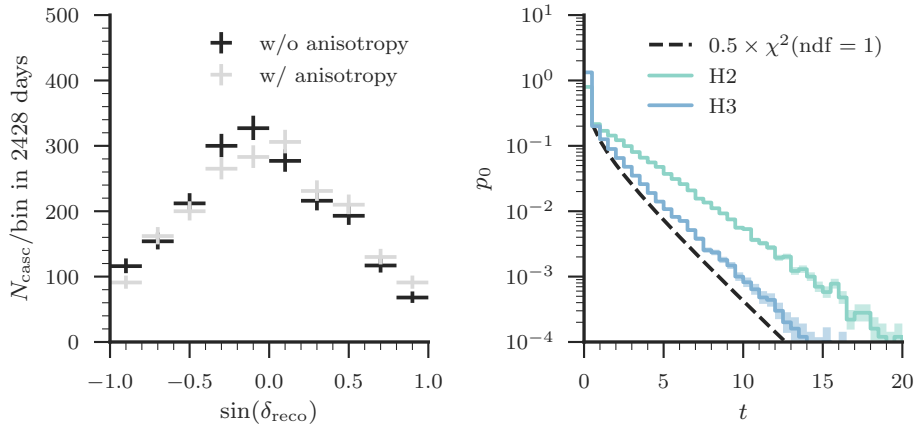


Figure 7.14: Left: sine declination distribution of the measured cascade-like events. The baseline photon tables for the directional and energy reconstructions do not account for the observed anisotropy of the South Pole ice discussed in Chapter 4. Here, it is compared to fairly new tables for the cascade reconstructions that have this effect incorporated. Right: test statistic distributions under the null-hypothesis for the hole ice models H2 and H3, compared to half a χ^2 -distribution with a ndf of one. The test statistic distributions are obtained by scrambling the experimental data in right ascension. The KRA_γ template is used.

Fig. 7.14, cascade-like events move from the southern to the northern sky if the new tables are used. Other than the hole ice model, both measured and simulated events are affected. This leads to a non-negligible decrease in the significance for excluding the null-hypothesis.

These findings show that this analysis is highly affected by the systematic uncertainties in the description of the ice. It should be pointed out that this is one of the first IceCube analyses at TeV energies and above that includes the hole ice model as a fit parameter. Uncertainties on the description of the hole ice are mostly considered in low-energy analyses with DeepCore, e.g. for the measurement of atmospheric neutrino oscillations [97]. The before-mentioned open issues will be addressed by replacing the MC datasets with new sim-

ulations that are created using the newest version 3.2 of the SPICE model and a better parametrization of the DOMs' angular sensitivity. Moreover, the optical properties of the bulk ice, namely effective scattering and absorption length, and the optical DOM efficiency will be incorporated into the likelihood fit as nuisance parameters. This work is still on-going and beyond the scope of this thesis.

8 Search for Neutrino Emission from 1ES 1959+650

In this chapter, the search for neutrino emission from 1ES 1959+650 during its flaring phase in spring 2016 is presented. This analysis is part of a broader IceCube follow-up campaign: it is performed together with a search for event clusters in time and a neutrino-gamma-ray correlation analysis, using gamma-ray light curves provided by FACT and MAGIC [132]. All three analyses are applied to the through-going muon track sample described in Chapter 6.

8.1 Analysis Method

The through-going muon track sample is split into an on and off-time subsample. The on-time window of 89 days is given by the duration of the flaring phase and shown in Fig. 3.6. The probability density to observe N events in the on-time window is given by

$$p(N; n_s, n_b) = \frac{(n_s + n_b)^N}{N!} \exp(-(n_s + n_b)), \quad (8.1)$$

where n_s and n_b are the number of signal and background events, respectively. The expected number $\langle n_b \rangle$ of background events is estimated from the event rate in the off-time window. The signal refers to the potential neutrino emission from 1ES 1959+650 during the flaring phase. The probability density is combined with the per-event likelihood

$$\mathcal{L}_i = \frac{n_s \mathcal{S}_i + \langle n_b \rangle \mathcal{B}_i}{n_s + \langle n_b \rangle} \quad (8.2)$$

to the likelihood function

$$\mathcal{L}(n_s) = p(N; n_s) \prod_i^N \mathcal{L}_i(n_s) \quad (8.3)$$

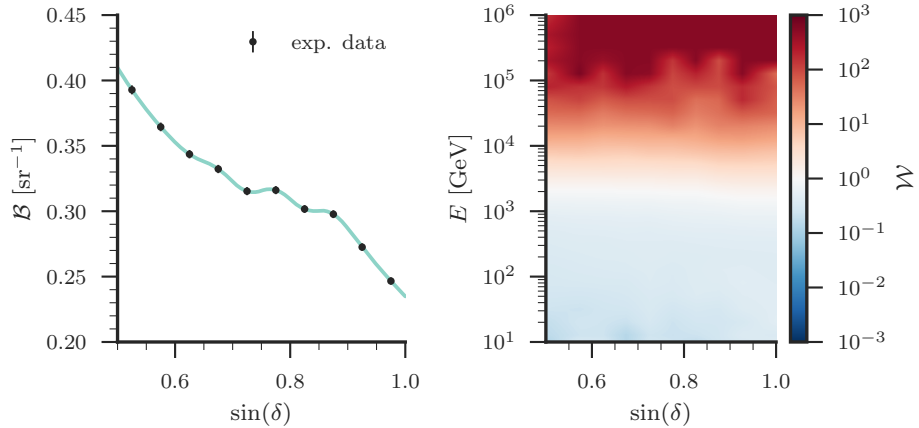


Figure 8.1: Spatial PDF (left) and example energy weighting function for a spectral index of $\gamma = 2$ (right).

where \mathcal{S}_i and \mathcal{B}_i are the per-event signal and background spatial probability densities, respectively [133]. The signal spatial PDF is approximated with a Gaussian distribution

$$\mathcal{S}(\hat{\mathbf{p}}, \sigma) = \frac{1}{2\pi\sigma^2} \exp\left(-\frac{\psi(\hat{\mathbf{p}}, \hat{\mathbf{p}}_s)^2}{2\sigma^2}\right), \quad (8.4)$$

which depends on the angular distance ψ_i between neutrino and source location, $\hat{\mathbf{p}}_i$ and $\hat{\mathbf{p}}_s$, in equatorial coordinates. The event's angular uncertainty is given by a single number σ_i ; see Section 8.2. The background spatial PDF is obtained from the experimental data in the off-time window:

$$\mathcal{B}(\delta) = \frac{1}{2\pi} \times p_{\text{exp}}(\delta), \quad (8.5)$$

where $p_{\text{exp}}(\delta)$ is the measured sine declination distribution. The factor 2π accounts for the flat detector acceptance in right ascension. The spatial background distribution is shown in Fig. 8.1. The test statistic

$$t \equiv 2 \log(\Lambda) \equiv 2 \log\left(\frac{\mathcal{L}(\hat{n}_s)}{\mathcal{L}(n_s = 0)}\right) \quad (8.6)$$

is defined, where \hat{n}_s is the signal strength that maximizes the likelihood function. The log-likelihood ratio is given by

$$\log(\Lambda) = -\hat{n}_s + \sum_i^N \log\left(\frac{\hat{n}_s}{\langle n_b \rangle} \frac{\mathcal{S}_i}{\mathcal{B}_i} \mathcal{W}_i + 1\right). \quad (8.7)$$

A signal over background weighting factor \mathcal{W}_i is introduced, which allows to include energy information: high-energy neutrinos are more likely of extra-terrestrial origin and thus their contribution to the likelihood is weighted stronger. The signal energy distribution for the energy weighting is obtained from MC simulations, weighted to an isotropic unbroken power-law flux. As for the spatial PDF, the background energy distribution is obtained from the experimental data in the off-time window. The weighting function depends on the spectral index γ . It is shown in Fig. 8.1 for a spectral index of $\gamma = 2$. The weighting function is pre-evaluated for a range of spectral indices and interpolated.

The likelihood function has been implemented into the SkyLab¹ framework for likelihood-based point source searches with neutrino telescopes by the author of this thesis [134]. SkyLab numerically minimizes the negative log-likelihood function $-\log(\Lambda)$ at a source location $\hat{\mathbf{p}}_s$ with respect to n_s and γ , using the L-BFGS-B algorithm. Moreover, methods are provided for scanning the likelihood function over the entire sky or around a potential source location, and to compute sensitivities, discovery potentials, and upper limits. For the implementation of Eq. (8.7) into SkyLab, the author of this thesis introduced a new abstract base class, both the existing and all future likelihood functions are derived from, and performed an extensive code cleanup. All changes were merged into the official SkyLab repository.

8.2 Angular Uncertainty Estimation

For the angular uncertainty estimation, the negative log-likelihood function of the directional reconstruction is evaluated on a grid of zenith and azimuth

¹<https://github.com/coenders/skylab>

angles around the minimum [135]. In each grid point, it is minimized with respect to the coordinates of the track’s support vector. A paraboloid is fitted to the obtained negative log-likelihood values based on an analytical χ^2 -minimization. The angular uncertainty is extracted from the covariance matrix. It can be represented as the lengths of the minor and major axes, σ_{minor} and σ_{major} , of the paraboloid’s 1σ error ellipse, and a rotation angle with respect to the azimuth angle axis. The quadratic mean

$$\sigma \equiv \sqrt{\frac{\sigma_{\text{minor}}^2 + \sigma_{\text{major}}^2}{2}} \quad (8.8)$$

is used for neutrino point source searches with IceCube. About 4% of the measured events have a failed paraboloid fit. They are assigned a fixed angular uncertainty of 1.54° , which is obtained from simulated events with a failed paraboloid fit, weighted to an isotropic unbroken power-law flux with a spectral index of $\gamma = 2$. The directional reconstruction does not account for various systematic uncertainties, e.g. the optical properties of the ice. This leads to an energy-dependent bias in the estimated angular uncertainties, as shown in Fig. 8.2. A *pull correction* is applied: the angular uncertainty pulls $p_i \equiv \log(\psi_i/\sigma_i)$ are defined as the logarithm of the ratio of the opening angle ψ_i between true and reconstructed neutrino direction over the reconstructed angular uncertainty σ_i . The bias in the median pull distribution along reconstructed energy E is parametrized with the polynomial

$$\begin{aligned} \bar{p}(E) = & 5.67 \times 10^{-4} \log^6(E) - 1.22 \times 10^{-2} \log^5(E) + 9.19 \times 10^{-2} \log^4(E) \\ & - 0.24 \log^3(E) - 0.19 \log^2(E) + 1.85 \log(E) - 1.98. \end{aligned} \quad (8.9)$$

The quadratic mean σ is expected to follow a bivariate distribution with a median of about 1.177. Hence, the pull-corrected angular uncertainties are given by

$$\tilde{\sigma}_i = \sigma_i \times \frac{\exp(\bar{p}(E_i))}{1.177}. \quad (8.10)$$

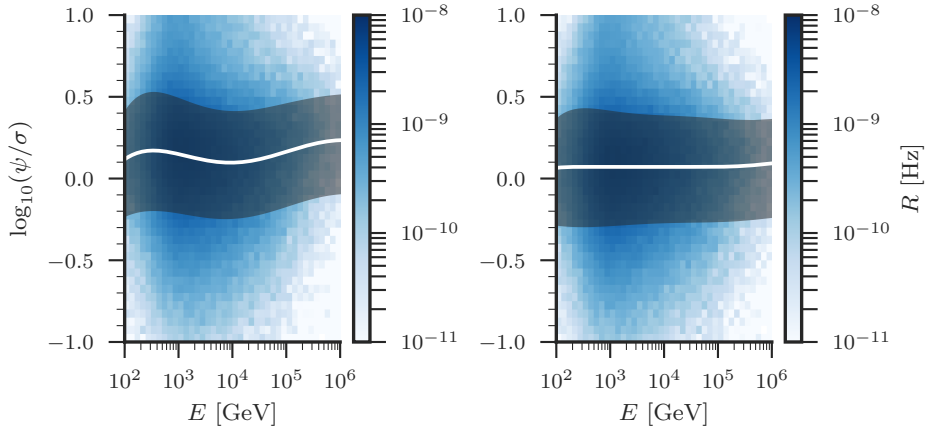


Figure 8.2: Angular uncertainty pull distribution along reconstructed energy with (left) and without (right) pull correction. The solid line shows the median pulls and the shaded area shows the 1σ range around the median. Only events with reconstructed declinations larger than 30° are taken into account. The MC simulation is weighted to an isotropic unbroken power-law flux with a spectral index of $\gamma = 2$.

All events with a pull-corrected angular uncertainty of larger than 5° are removed, because the approximated signal spatial PDF is only valid for small angular uncertainties. Less than 0.8% of the measured events are lost due to this restriction.

8.3 Sensitivity and Discovery Potential

The negative log-likelihood function given by Eq. (8.7) is numerically minimized with respect to the signal strength n_s and the spectral index γ . Only positive n_s values are allowed and the spectral index is varied between one and four. The test statistic distributions are obtained by drawing n_b events with declinations larger than 30° from the experimental data in the off-time window, where n_b is Poisson-distributed with a mean of $\langle n_b \rangle \approx 6803$. The drawn events are scrambled in right ascension. Signal is injected by drawing

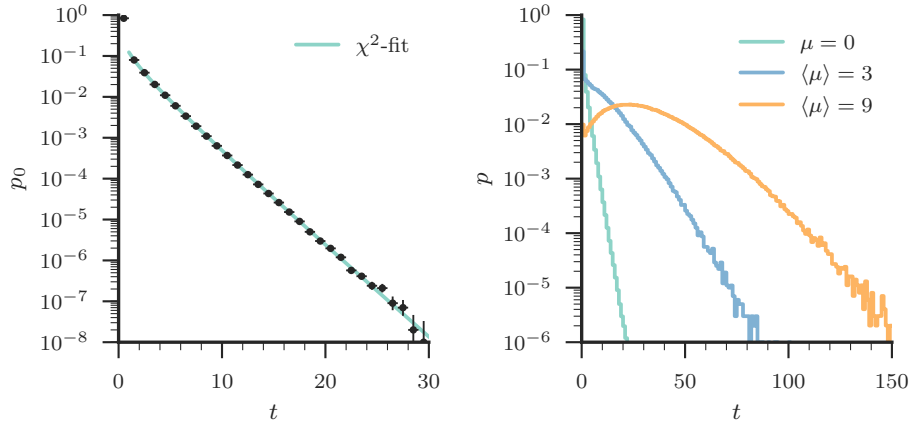


Figure 8.3: Right: Test statistic distribution for different mean numbers $\langle \mu \rangle$ of injected signal events. The injected source spectrum is $\gamma_s = 2$. Left: the test statistic values larger than zero under the null-hypothesis are fitted with a χ^2 -distribution.

μ simulated events with true sine declinations between ± 0.01 around the sine declination of 1ES 1959+650 and rotating their true direction onto the source location. The number μ of injected signal events is Poisson-distributed. The signal events are drawn based on the effective area in this declination band, convolved with an unbroken power-law energy spectrum with a spectral index of γ_s . Fig. 8.3 shows the test statistic distribution $p(t; \langle \mu \rangle, \gamma_s)$ for different mean numbers $\langle \mu \rangle$ of injected signal events. Under the null-hypothesis, $p_0(t) = p(t, \mu = 0)$, the distribution of test statistic values larger than zero is well-described by a χ^2 -distribution with a scale of 0.4789 ± 0.0005 and a ndf of 1.107 ± 0.001 . With increasing source strength, the test statistic distribution gets shifted to higher test statistic values. The sensitivity and discovery potential are quantified as explained in Chapter 7. The threshold test statistic values $t_\alpha = 0$ and $t_\alpha \approx 25.7$ are directly extracted from the test statistic distribution under the null-hypothesis instead of using the fitted χ^2 -distribution. The latter value corresponds to a p-value of about 2.87×10^{-7} (5σ). The obtained $\langle \mu \rangle$ values are converted into fluences based on the effective area in the

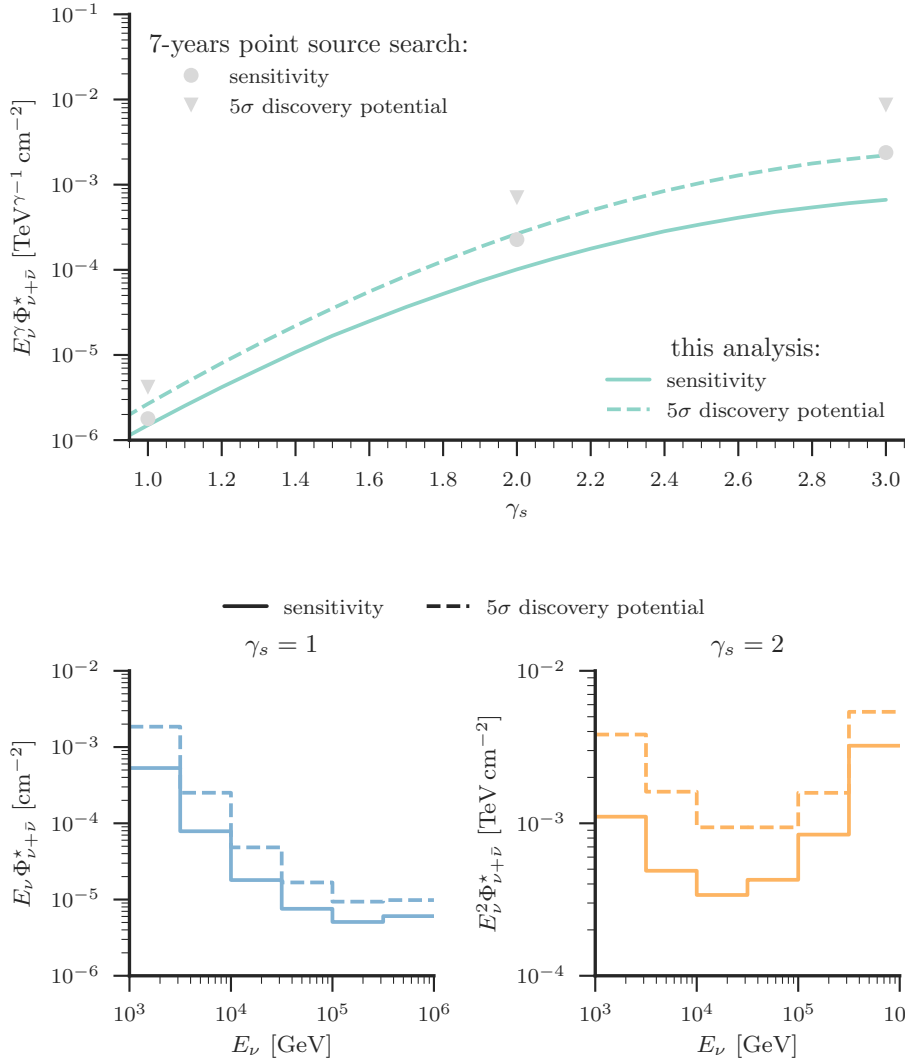


Figure 8.4: Sensitivity and discovery potential neutrino plus anti-neutrino fluence for the spring 2016 flaring phase of 1ES 1959+650; top: for various injected source spectral indices and compared to the steady point source search with seven years of IceCube data [54]; and bottom: differential in true neutrino energy.

γ_s	$\langle\mu\rangle_{\text{sens}}$	$\langle\mu\rangle_{\text{disc}}$	$E^\gamma\Phi_{\text{sens}}^*$	$E^\gamma\Phi_{\text{disc}}^*$
1	2.4	4.3	1.5×10^{-6}	2.7×10^{-6}
2	3.2	8.4	1.0×10^{-4}	2.7×10^{-4}
3	5.5	18.5	6.6×10^{-4}	2.2×10^{-3}
unit: $\text{TeV}^{\gamma-1} \text{cm}^{-2}$				

Table 8.1: Sensitivity and discovery potential.

sine declination band with a width of 0.02 centered around the sine declination of 1ES 1959+650. The sensitivity and discovery potential neutrino plus anti-neutrino fluences are shown in Fig. 8.4 and Table 8.1. The improvement with respect to the steady point search with seven years of IceCube data varies between factors of about 1.2 and 4 and increases for softer injection spectra. The differential fluences are obtained by injecting only signal events with true neutrino energies from a certain energy range, given by the bin edges shown in Fig. 8.4. As pointed out before, this analysis is part of a broader IceCube campaign: a model-independent search for event clusters in time and a model-dependent neutrino-gamma-ray correlation analysis were performed by other IceCube collaborators. For the latter, gamma-ray light curves are provided by FACT and MAGIC, which are used as the neutrino arrival time PDF in the corresponding likelihood fit [132]. As presented in [132] and shown in Fig. 8.5, this analysis starts to be more sensitive than the search for event clusters in time once the time window for this search is larger than 30 days. As expected, the model-independent analyses are less sensitive than the neutrino-gamma-ray correlation analysis, as long as the same light curve is used for the signal injection and the likelihood model. Hence, all three follow-up analyses are complementary.

8.4 Unblinding Results

No deviation from the null-hypothesis is observed; the fitted test statistic value is $t_{\text{obs}} = 0$. As shown in Fig. 8.6, only three events are compatible with the location of 1ES 1959+650 within 1σ . Their angular uncertainties

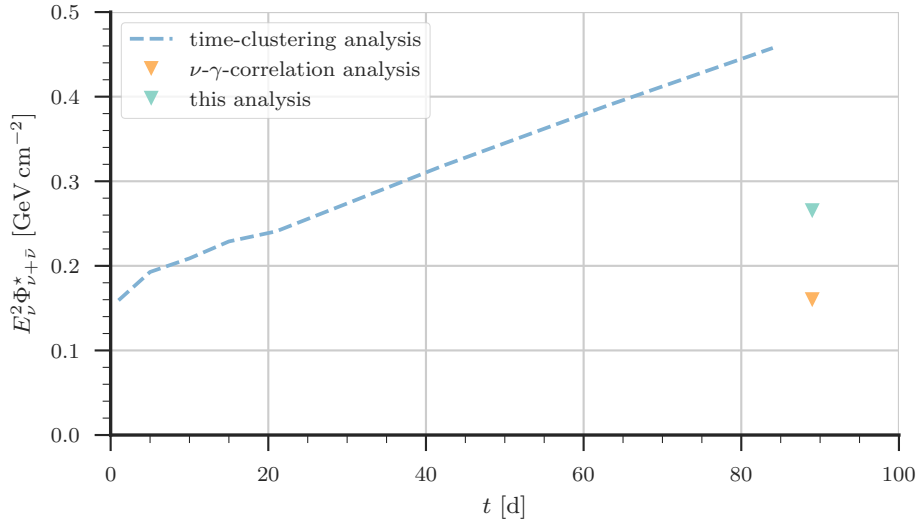


Figure 8.5: Comparison of the discovery potential of this analysis to the other two analyses of the IceCube follow-up campaign, which were performed by other IceCube collaborators [132]. Here, a source spectral index of $\gamma_s = 2$ is assumed. The time t gives the length of the on-time windows in days that are used for injection of signal events. The discovery potential of the neutrino-gamma-ray correlation analysis is determined by using the same time PDF for both the signal injection and the likelihood fit.

are larger than 2° and their reconstructed energies are rather low. Moreover, their arrival times do not seem to coincide with stronger gamma-ray flares from 1ES 1959+650. Because of the null-observation, the 90% upper limit on the neutrino plus anti-neutrino fluence corresponds to the sensitivity curve shown in Fig. 8.4; see Eq. (7.11). As presented in [132], the neutrino-gamma-ray correlation analysis yields also a test statistic value of $t_{\text{obs}} = 0$. The most significant cluster of events in time is 3.3 hours long around the most-energetic event in the on-time window. The cluster consists of two events and a p-value of 37% is obtained, which is still compatible with the null-hypothesis. In conclusion, no evidence for neutrino emission from 1ES 1959+650 during its flaring phase in spring 2016 is found.

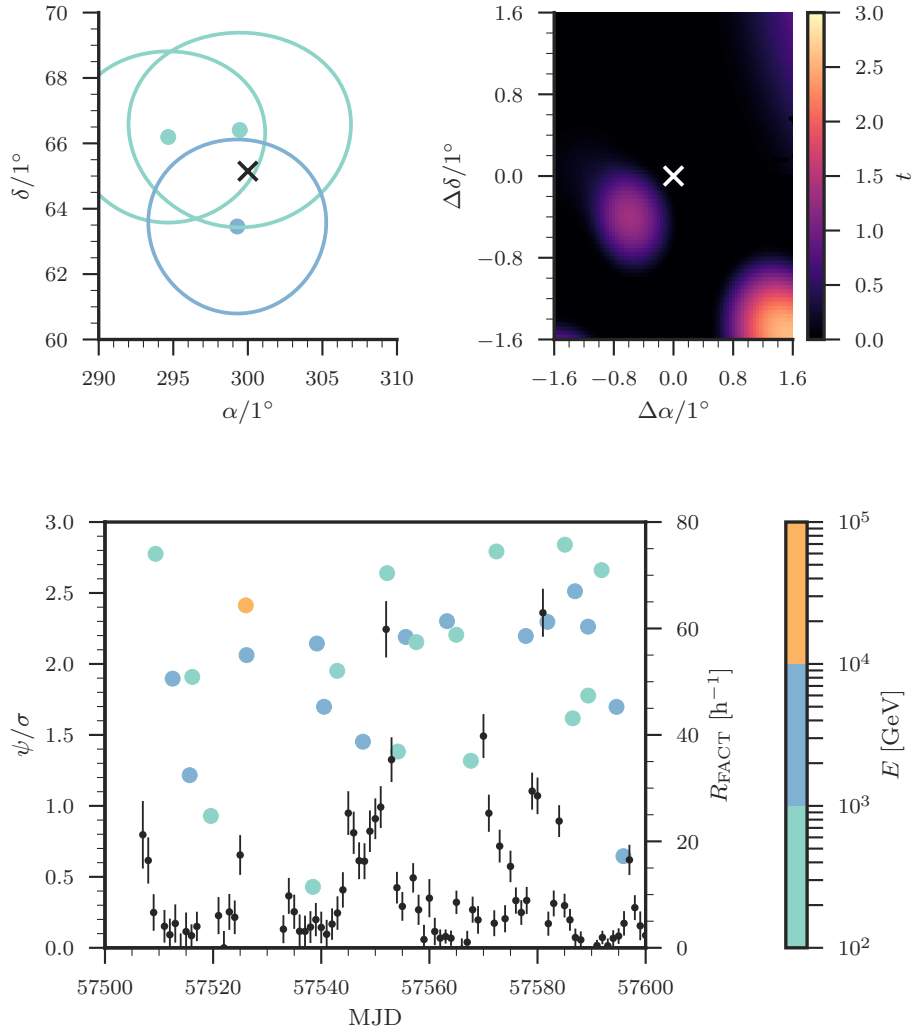


Figure 8.6: Top: test statistic scan around the location of 1ES 1959+650 (right). Overlaid are the locations of all measured events that are compatible with the source location within 1σ (left). Bottom: arrival times of all measured events that are compatible with the source location within 3σ , overlaid with the excess rate measured with the FACT telescope. The events' reconstructed energies are color-coded.

9 Conclusion

The search for a deviation from isotropy in the arrival direction of astrophysical neutrinos measured with the IceCube neutrino detector is one of the most fascinating challenges in the next couple of years in the very active field of neutrino astronomy. In this thesis, two analyses are presented to search for Galactic and extra-galactic neutrino emission with IceCube.

For the first analysis, templates for cosmic-ray induced neutrino emission in the Galactic plane are used. Neutrino emission in the Galactic plane is one of the most promising candidates for an anisotropic diffuse astrophysical neutrino flux. The null-hypothesis of a single isotropic unbroken power-law neutrino flux of extra-terrestrial origin is tested against the two-component hypothesis, which includes the contribution from Galactic neutrinos. A forward-folding likelihood fit using templates is applied to seven years of MESE data. Sensitivities and discovery potentials are presented for two different Galactic neutrino flux models. The benchmark model is based on the π^0 -component of the *Fermi*-LAT diffuse gamma-ray model. In comparison, the KRA_γ model is tested, which includes anisotropic diffusion of cosmic rays in the Galaxy. Stronger neutrino emission is predicted in the inner Galaxy than for the *Fermi*-LAT model. A comparison of this analysis to the published IceCube sensitivity for the KRA_γ model with a high-energy cutoff at 50 PeV shows an expected improvement of about a factor two, if an isotropic neutrino flux of extra-galactic origin with a hard spectral index of $\gamma_{\text{EG}} = 2.19$ and a prompt atmospheric neutrino flux of 1.06 times ERS are assumed. The region of strong neutrino emission in the inner Galaxy predicted by the KRA_γ model lies in the southern sky and is not accessible by the through-going muon track sample the published IceCube result is based on. The high-energy cutoff at 50 PeV is very optimistic and most likely already excluded by indirect cosmic-ray experiments. Although not explicitly used, this analysis is also expected to constrain the

KRA $_{\gamma}$ model with a more realistic high-energy cutoff of 5 PeV. This is not the case for the Galactic plane analysis based on through-going muon tracks at the current state. A further increase in sensitivity could be achieved when combining this analysis with the results from the ANTARES neutrino telescope [136]. The analysis presented in this thesis has been unblinded in December 2017; a publication of the results is planned in the near future. Moreover, a combination of this analysis with the through-going muon track analysis is considered. The latter better constrains the conventional and prompt atmospheric neutrino fluxes and is very sensitive to the extra-galactic neutrino flux. The expected degeneracy between the Galactic and extra-galactic neutrino flux for MESE-alone will be decreased and the sensitivity to Galactic diffuse neutrino emission should increase.

The second analysis that is presented in the thesis is dedicated to extra-galactic neutrino emission. The HBL 1ES 1959+650 showed a very strong activity in high-energy gamma rays in spring 2016, which lasted for about three months. This source is very prominent in the neutrino astronomy community because of an orphan gamma-ray flare observed in 2002. Three neutrinos were detected with the AMANDA neutrino telescope in coincidence with this flare. Because the experimental data was already unblinded, no p-value was reported. The source was in quiescent state until the flaring phase in 2016. Hence, a new chance was given to search for neutrino emission from 1ES 1959+650 while the source is in an active state. No evidence for neutrino emission is found, neither with the presented time-integrated search method nor with the other two analyses that are part of the IceCube follow-up campaign. The non-observation of neutrino emission from 1ES 1959+650 allows to constrain the lepto-hadronic models that predict a correlation between high-energy gamma-ray and neutrino emission, e.g. [137]. This work is still ongoing. Furthermore, a more automated approach of such follow-up analyses in the context of IceCube's realtime alert program will help to create larger datasets of multi-messenger observations in the future [138].

Acknowledgments

The work presented in the thesis would not have been possible without the support of many people I would like to thank at this point.

First of all, I would like to thank my supervisor, Elisa Resconi, for giving me the opportunity to work in the fascinating field of neutrino astronomy with IceCube and to be part of this amazing working group here at the Technical University of Munich. Thank you for encouraging me to focus on my interest in developing software for IceCube and to dedicate part of my working time to software-related service work for the *strike team*.

I would like to thank Jochen Greiner for agreeing to be the second reviewer of this thesis, and Alejandro Ibarra for being the chair of the review committee. Special thanks go to my coworkers, who became friends over the last three and a half years. Without the discussions in the *Coffee* and the after-work activities, my life as a PhD student would have been a lot less fun.

In particular, I would like to thank Andrea, Christian, Martin, Matthias, Stefan, and Stephan for the extensive and in some cases last-minute proofreading of my thesis.

The financial support of the DAAD gave me the opportunity to stay abroad at the University of Wisconsin-Madison in 2015. Those were amazing and very productive six weeks.

Last but not least, I would like to thank my family and friends for all their support and love; especially my girlfriend, Susanna. Thank you for always being there when I was struggling with work and for making me smile again.

A Expected Number of Events

In the following tables, the expected numbers of cascade and track-like events in seven years of MESE data are listed for all lepton flux models introduced in Chapter 7; see Table 7.1. The event numbers are separately given for the northern and the southern sky. Table A.1 and Table A.2 show the expectations for the H2 and H3 hole ice neutrino MC datasets, respectively. The extragalactic neutrino flux is weighted to the best-fit differential muon plus anti-muon neutrino flux presented in Chapter 3, assuming a neutrino flavor ratio of 1:1:1. A global flux normalization of $c_{\text{prompt}} = 1.06$ is used for the prompt atmospheric neutrino flux model. The Galactic neutrino flux corresponds to the KRA_γ model with a high-energy cutoff at 50 PeV.

N_{events}	Cascade-like	Track-like
down-going, $\sin(\delta_{\text{reco}}) \leq -0.2$		
μ	67	16
ν_{conv}	296	67
ν_{prompt}	19	1
ν_{EG}	60	4
ν_{gal}	28	2
up-going, $\sin(\delta_{\text{reco}}) > -0.2$		
μ	8	29
ν_{conv}	925	7689
ν_{prompt}	51	54
ν_{EG}	67	40
ν_{gal}	15	11

Table A.1: Expected number of events for the H2 model.

N_{events}	Cascade-like	Track-like
down-going, $\sin(\delta_{\text{reco}}) \leq -0.2$		
μ	67	16
ν_{conv}	383	79
ν_{prompt}	22	1
ν_{EG}	64	4
ν_{gal}	30	2
up-going, $\sin(\delta_{\text{reco}}) > -0.2$		
μ	8	29
ν_{conv}	854	7910
ν_{prompt}	49	55
ν_{EG}	63	40
ν_{gal}	14	11

Table A.2: Expected number of events for the H3 model.

B POCAM Simulation

As described in Chapter 4, the author of this thesis developed the first simulation of an early version of the POCAM design, based on Geant4 [113, 139]:

A light-diffusing sphere is placed inside the spherical borosilicate glass housing of a standard IceCube DOM; see Fig. 4.1. Both volumes are filled with air. The spherical glass housing is simulated with an outer radius of 16.5 cm and a thickness of 1.25 cm [93]. The radius of the light-diffusing sphere is adjustable and its thickness is idealized to be 1 mm; the baseline radius is 12 cm. IceCube’s standard 405 nm LED is attached to the inner layer of the light-diffusing sphere and facing the opposite direction. The LED output is simulated with a Gaussian wavelength, a uniform cosine-law angular, and a rectangular timing distribution; wavelength standard deviation, opening angle, and pulse width are adjusted to 10 nm, 10° , and 10 ns, respectively. The focused light output of the LED is diffused after several reflections on the inner layer of the light-diffusing sphere and released into the surrounding ice after passing the outer glass housing. Absorption in both the light-diffusing sphere and the glass housing as well as shadowing by the waistband/harness and the penetrator are taken into account; see Chapter 4. All photon quantities are stored with respect to a reference detection sphere with a radius of 20 cm. Polytetrafluoroethylene (PTFE) with a reflectivity of about 99%¹ is used as the material for the light-diffusing sphere. Values for the glass housing’s absorption length are taken from IceCube laboratory measurements; its refractive index is adjusted to 1.48.

With this simulation, two different methods for releasing the photons out of the light-diffusing sphere were studied: a multi-port setup and a semi-transparent setup. The goal was to optimize the homogeneity and the timing of the POCAM light emission. For the multi-port setup, several equidistantly

¹Value is provided by manufactures: SphereOptics Zenith Polymer[®].

Configuration		
C1	$R = 12 \text{ cm}$	$\alpha = 1^\circ, n = 768$
C2	$R = 3 \text{ cm}$	$\alpha = 1^\circ, n = 768$
C3	$R = 12 \text{ cm}$	$P_r = 0.96, P_t = 0.025$

Table B.1: Different POCAM configurations; multi-port setups with port opening angle α and number of ports n . Semi-transparent setup with reflection and transmission probabilities P_r and P_t , respectively.

distributed ports (holes), photons can escape through, are placed on the light-diffusing sphere, based on a HEALPix grid. Each port is shaped as a spherical sector with an opening angle α . For the second method, the light-diffusing sphere is made semi-transparent by defining probabilities for a photon to be either diffusely reflected, diffusely transmitted, or absorbed every time its path coincides with the sphere: P_r , P_t , and $P_a = 1 - P_r - P_t$, respectively². The version of Geant4 used for this study does not support diffuse transmission natively; it has been established by the author of this thesis by slightly modifying the method for diffuse reflection: the direction of the outgoing photon is inverted after it is reflected on the inner layer of the light-diffusing sphere.

Three different POCAM configurations are presented in this thesis, which are listed in Table B.1. Fig. B.1 shows the directional and time distributions of photons emitted from the POCAM into the surrounding ice. The directional distributions are shown in spherical coordinates. Exponential distributions are fitted to the shown emission time profiles for $t > 20 \text{ ns}$. The best-fit decay times are 26.4 ns, 8.1 ns, and 13.1 ns for the POCAM configurations C1, C2, and C3, respectively; statistical uncertainties are on the order of 10^{-7} ns . A comparison of the three presented POCAM configurations shows that a smaller light-diffusing sphere performs better in terms of homogeneous and fast light emission with respect to the baseline radius of 12 cm. The semi-transparent configuration C3 shows a similar homogeneity than the baseline multi-port configuration C1, but the light emission is faster.

²Values are provided by manufactures: SphereOptics Zenith Polymer[®].

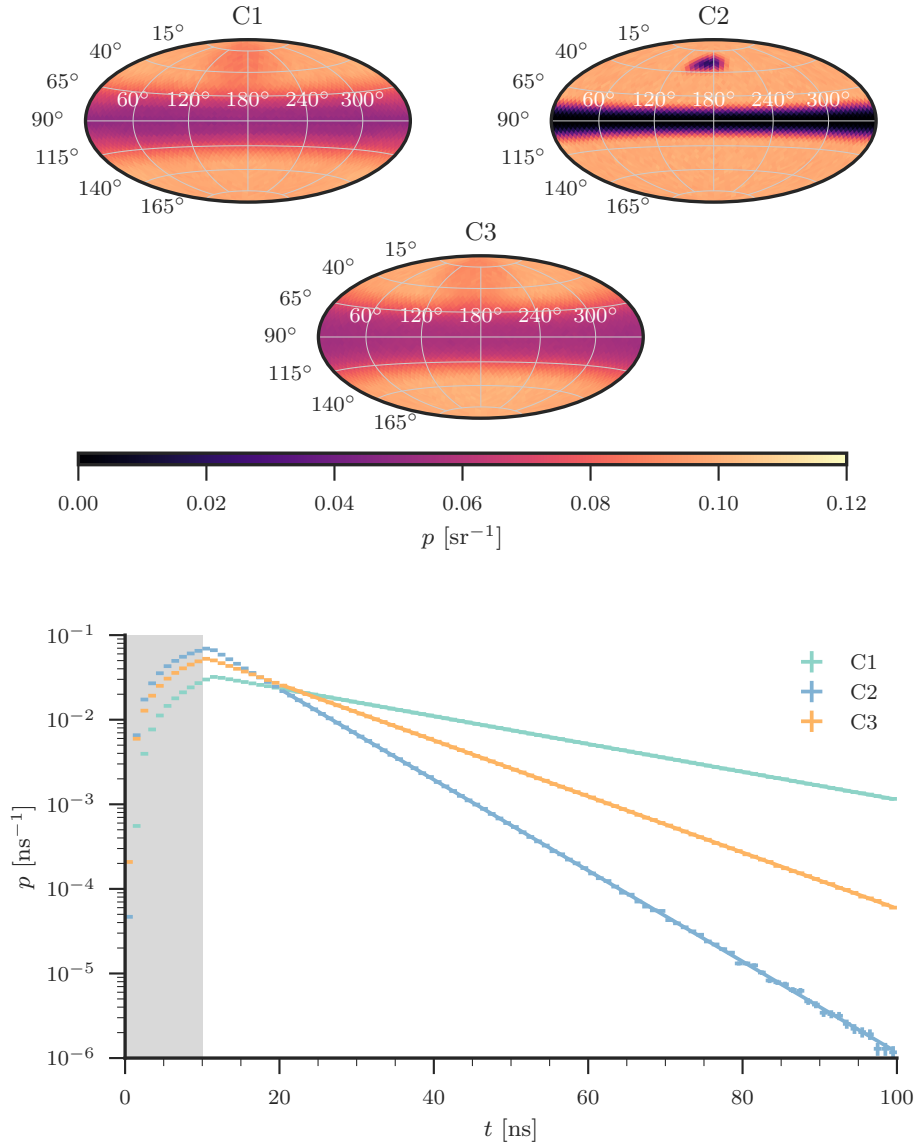


Figure B.1: Directional (top) and time (bottom) distributions of photons emitted from the POCAM. The LED and penetrator positions are at $\phi = 0^\circ$, $\theta = 90^\circ$ and $\phi = 180^\circ$, $\theta = 30^\circ$, respectively. The harness is between $\theta = 79^\circ$ and $\theta = 101^\circ$. The gray-shaded area refers to the rectangular LED time profile. Exponential distributions are fitted for $t > 20$ ns and shown as solid lines.

Based on the findings of this simulation study, a smaller semi-transparent PTFE sphere with a radius of 2.5 cm has been chosen for the first prototype POCAM, which has been tested in the Baikal-GVD neutrino detector [112].

Glossary

1ES 1959+650 HBL at a declination of $\delta \approx +65^\circ 8' 55.0''$ and a right ascension of $\alpha \approx 19^{\text{h}} 59^{\text{m}} 59.8^{\text{s}}$ in the J2000.0 epoch 1–3, 27–29, 59, 87, 92–96, 98

Asimov dataset An Asimov dataset allows to estimate expected median test statistic values without the need to create pseudo-experiments. It is created by not applying Poisson fluctuations to the expected numbers of neutrino events per bin. 78–83

ATWD Analog Transient Waveform Digitizer 38

BDT boosted decision trees 59

BL Lac BL Lacertae 27, 28, 108

CC charged current 32–34, 36, 37, 52, 57, 59, 65

COG center of gravity; charge-weighted average position of hit DOMs 44, 59

CORSIKA COsmic Ray SIMulations for KAscade 10, 59, 66

DeepCore denser instrumented sub-array in the center of IceCube 31, 32, 53–55, 58, 109

DOM digital optical module 31, 32, 34–36, 38, 40, 41, 43–47, 53–56, 58, 86, 103, 107, 109–111

effective area Given a differential neutrino flux model $\Phi_{\nu+\bar{\nu}}$ and the effective area A_{eff} , the expected number $n_{\nu+\bar{\nu}}$ of neutrino plus anti-neutrino

events can be calculated as

$$n_{\nu+\bar{\nu}} = t_{\text{live}} \int_{\varphi_{\min}}^{\varphi_{\max}} \int_{\vartheta_{\min}}^{\vartheta_{\max}} \int_{E_{\min}}^{E_{\max}} A_{\text{eff}} \Phi_{\nu+\bar{\nu}} dE d\vartheta d\varphi, \quad (\text{B.1})$$

where t_{live} is the time span the detector took data. The effective area contains effects like neutrino absorption in the Earth, the neutrino cross sections with ice, the selection efficiency, and so on. 51, 52, 59, 92

EHE extremely high-energy events 40, 51, 57

ERS prompt atmospheric neutrino flux model 18, 20, 62, 64, 67, 97

FADC fast analog-to-digital converter 38

Fermi-LAT *Fermi* Large Area Telescope 22–26, 64, 69, 74–80, 97

Geant4 toolkit for the simulation of the passage of particles through matter 103, 104

GR Glashow resonance 33, 57

Gulliver software project for likelihood-based reconstructions within IceTray 43, 49, 50

H2 hole ice model with an effective scattering length of 50 cm 35, 36, 72, 76, 77, 84, 85, 101, 102

H3 hole ice model with an effective scattering length of 30 cm 35, 36, 72, 76, 84, 85, 101, 102

H3a three-population primary cosmic-ray model; a mixed composition is assumed for the third population 9, 10, 17, 18, 62

H4a three-population primary cosmic-ray model; a protons-only composition is assumed for the third population 6, 9, 10, 66

HBL high-energy peaked BL Lac 28, 98, 107

HEALPix algorithm do divide a sphere into equally sized pixels that are arranged along equidistant rings in colatitude 55, 64, 69, 104

HESE high-energy starting events 19, 20, 27, 51, 53, 54, 57

HKKMS06 conventional atmospheric neutrino flux model 18, 62, 64

HLC hard local coincidence 38, 53, 55, 57, 109, 111

hole ice refrozen ice column around the string 35, 36, 41, 72, 77, 85, 101, 108

homogenized total charge sum of charges of all HLC pulses detected on non-DeepCore DOMs that do not contribute more than 50 % of the total charge 53–56, 62

IC79 IceCube in its 79-string configuration 32, 51, 54

IC86 completed IceCube detector; if followed by a year, it specifies a detector run season, e.g. IC86 2011 32, 52, 59, 62, 109

IceTray IceCube software framework 43, 49, 108

KRA conventional cosmic-ray propagation model with a diffusion coefficient that follows a Kraichnan spectrum 26, 27, 77, 109

KRA_γ KRA model tuned on gamma-ray data 25–27, 64, 67, 74–76, 78–82, 84, 85, 97, 98, 101

L-BFGS-B numerical minimization algorithm with gradient support 64, 89

line fit first-guess directional reconstruction for track-like events 40, 43, 58

MC Monte Carlo 9, 21, 46, 47, 51, 66, 76, 78, 83–85, 89, 91, 101, 110, 111

MCEq Matrix Cascade Equation; numerical solver of the cascade equation for atmospheric leptons 17, 18

MESE medium-energy starting events 21, 26, 46–48, 51, 52, 58, 62, 63, 65, 82, 97, 98, 101

Millipede software toolkit for energy reconstructions in IceCube 47

MJD Modified Julian Date 29

MPE multi-photoelectron 46, 47, 58, 111

Muon Filter online filtering optimized for muon tracks 40, 58

Muon Level 3 pre-selection optimized for muon tracks 57, 58

MuonGun software toolkit for efficiently simulating atmospheric muons in IceCube 64, 66

NC neutral current 32–34, 36, 37, 52, 59

ndf degree of freedom 73–75, 81, 85, 92

NuGen Neutrino Generator 65

optical DOM efficiency effective detection efficiency of the DOM 41, 86

PDF probability density function 24, 45, 88, 89, 91, 94, 95

photon tables spline-interpolated tabulated time residual probability densities, which are obtained from photon propagation MC simulations 47, 84, 85

PMT photomultiplier tube 32, 35, 36, 38, 41, 46

POCAM Precision Optical CALibration Module; proposed calibration source for IceCube-Gen2 42, 103–106

PTFE polytetrafluoroethylene 103, 106

p-value quantifies how compatible an observed test statistic value is with a hypothesis 73, 77, 80–82, 84, 92, 95, 98

SED spectral energy distribution 27–29

SIBYLL hadronic event generator; the newer versions 2.3 and 2.3c include the production of charmed hadrons, which is missing in previous versions 10, 17, 66

SkyLab software framework for likelihood-based point source searches with neutrino telescopes 89

SLC soft local coincidence 38, 55

SMT simple multiplicity trigger 38, 111

SMT8 SMT requiring at least eight HLC hits within a sliding time window of 5 μ s 39

SPE single-photoelectron 44, 58

SPICE South Pole ice 35, 36, 41, 47, 86

spline-MPE directional reconstruction for track-like events, based on the MPE likelihood, using spline-interpolated tabulated time residual probability densities that are obtained from photon propagation MC 47, 56, 57, 59

SSC synchrotron self-Compton 28, 29

string cables the DOMs are attached to; the completed IceCube detector consists of 86 strings with 60 DOMs each 31, 32, 36, 38, 40, 53, 54, 56, 109, 111

time residual time difference between observed and expected photon arrival time in the DOM; the expectation refers to an unscattered Cherenkov photon 45, 55, 110, 111

TOI tensor of inertia; first-guess directional reconstruction for cascade-like events 40, 44

VHE very high energy 28, 29

Bibliography

- [1] F. W. Stecker. “Diffuse Fluxes of Cosmic High-Energy Neutrinos.” In: *The Astrophysical Journal* 228 (1979), pp. 919–927. DOI: 10.1086/156919.
- [2] D. Gaggero et al. “The gamma-ray and neutrino sky: A consistent picture of Fermi-LAT, Milagro, and IceCube results.” In: *The Astrophysical Journal* 815.2 (2015), p. L25. DOI: 10.1088/2041-8205/815/2/L25. arXiv: 1504.00227.
- [3] V. L. Ginzburg and S. I. Syrovatskii. *The Origin of Cosmic Rays*. Macmillan, 1964.
- [4] T. K. Gaisser, R. Engel, and E. Resconi. *Cosmic Rays and Particle Physics*. Cambridge University Press, 2016.
- [5] M. Aguilar et al. “Precision Measurement of the Proton Flux in Primary Cosmic Rays from Rigidity 1 GV to 1.8 TV with the Alpha Magnetic Spectrometer on the International Space Station.” In: *Physical Review Letters* 114 (2015), p. 171103. DOI: 10.1103/PhysRevLett.114.171103.
- [6] Y. S. Yoon et al. “Proton and Helium Spectra from the CREAM-III Flight.” In: *The Astrophysical Journal* 839.1 (2017), p. 5. DOI: 10.3847/1538-4357/aa68e4. arXiv: 1704.02512.
- [7] M. G. Aartsen et al. “Measurement of the cosmic ray energy spectrum with IceTop-73.” In: *Physical Review D* 88.4 (2013), p. 042004. DOI: 10.1103/PhysRevD.88.042004. arXiv: 1307.3795.
- [8] The Pierre Auger Collaboration. “The cosmic ray energy spectrum measured using the Pierre Auger Observatory.” In: *Proceedings of the 35th International Cosmic Ray Conference*. Vol. ICRC2017. Proceedings of Science, 2017, p. 486. arXiv: 1708.06592.

- [9] R. Alfaro et al. “All-particle cosmic ray energy spectrum measured by the HAWC experiment from 10 to 500 TeV.” In: *Physical Review D* 96.12 (2017), p. 122001. DOI: 10.1103/PhysRevD.96.122001. arXiv: 1710.00890.
- [10] M. Amenomori et al. “The all-particle spectrum of primary cosmic rays in the wide energy range from 10^{14} eV to 10^{17} eV observed with the Tibet-III air-shower array.” In: *The Astrophysical Journal* 678 (2008), pp. 1165–1179. DOI: 10.1086/529514. arXiv: 0801.1803.
- [11] S. Ter-Antonyan. “Sharp knee phenomenon of primary cosmic ray energy spectrum.” In: *Physical Review D* 89.12 (2014), p. 123003. DOI: 10.1103/PhysRevD.89.123003. arXiv: 1405.5472.
- [12] T. Antoni et al. “KASCADE measurements of energy spectra for elemental groups of cosmic rays: Results and open problems.” In: *Astroparticle Physics* 24 (2005), pp. 1–25. DOI: 10.1016/j.astropartphys.2005.04.001. arXiv: astro-ph/0505413.
- [13] W. D. Apel et al. “The spectrum of high-energy cosmic rays measured with KASCADE-Grande.” In: *The Astrophysical J.* 36 (2012), pp. 183–194. DOI: 10.1016/j.astropartphys.2012.05.023. arXiv: 1206.3834.
- [14] T. Abu-Zayyad et al. “Measurement of the cosmic ray energy spectrum and composition from 10^{17} eV to $10^{18.3}$ eV using a hybrid fluorescence technique.” In: *The Astrophysical Journal* 557 (2001), pp. 686–699. DOI: 10.1086/322240. arXiv: astro-ph/0010652.
- [15] R. U. Abbasi et al. “First observation of the Greisen-Zatsepin-Kuzmin suppression.” In: *Physical Review Letters* 100 (2008), p. 101101. DOI: 10.1103/PhysRevLett.100.101101. arXiv: astro-ph/0703099.
- [16] Y. Tsunesada et al. “Energy Spectrum of Ultra-High-Energy Cosmic Rays Measured by The Telescope Array.” In: *Proceedings of the 35th International Cosmic Ray Conference*. Vol. ICRC2017. Proceedings of Science, 2017, p. 535.

- [17] T. K. Gaisser. “Spectrum of cosmic-ray nucleons, kaon production, and the atmospheric muon charge ratio.” In: *Astroparticle Physics* 35 (2012), pp. 801–806. DOI: 10.1016/j.astropartphys.2012.02.010. arXiv: 1111.6675.
- [18] B. Peters. “Primary cosmic radiation and extensive air showers.” In: *Il Nuovo Cimento (1955–1965)* 22.4 (1961), pp. 800–819. DOI: 10.1007/BF02783106.
- [19] A. Aab et al. “Observation of a Large-scale Anisotropy in the Arrival Directions of Cosmic Rays above 8×10^{18} eV.” In: *Science* 357.6537 (2017), pp. 1266–1270. DOI: 10.1126/science.aan4338. arXiv: 1709.07321.
- [20] K. Greisen. “End to the Cosmic-Ray Spectrum?” In: *Physical Review Letters* 16 (17 1966), pp. 748–750. DOI: 10.1103/PhysRevLett.16.748.
- [21] G. T. Zatsepin and V. A. Kuzmin. “Upper limit of the spectrum of cosmic rays.” In: *JETP Letters* 4 (1966), pp. 78–80.
- [22] A. M. Hillas. “The Origin of Ultra-High-Energy Cosmic Rays.” In: *Annual Review of Astronomy and Astrophysics* 22.1 (1984), pp. 425–444. DOI: 10.1146/annurev.aa.22.090184.002233.
- [23] O. Adriani et al. “PAMELA Measurements of Cosmic-Ray Proton and Helium Spectra.” In: *Science* 332 (2011), pp. 69–72. DOI: 10.1126/science.1199172. arXiv: 1103.4055.
- [24] M. Aguilar et al. “Precision Measurement of the Helium Flux in Primary Cosmic Rays of Rigidities 1.9 GV to 3 TV with the Alpha Magnetic Spectrometer on the International Space Station.” In: *Physical Review Letters* 115.21 (2015), p. 211101. DOI: 10.1103/PhysRevLett.115.211101.
- [25] A. D. Panov et al. “Energy spectra of abundant nuclei of primary cosmic rays from the data of ATIC-2 experiment: Final results.” In: *Bulletin of the Russian Academy of Sciences: Physics* 73 (2009), pp. 564–567. DOI: 10.3103/S1062873809050098. arXiv: 1101.3246.

- [26] J. J. Engelmann et al. “Charge composition and energy spectra of cosmic-ray nuclei for elements from Be to Ni - Results from HEAO-3-C2.” In: *Astronomy and Astrophysics* 233 (1990), pp. 96–111.
- [27] S. P. Swordy et al. “Relative abundances of secondary and primary cosmic rays at high energies.” In: *The Astrophysical Journal* 349 (1990), pp. 625–633. DOI: 10.1086/168349.
- [28] D. Mueller et al. “Energy spectra and composition of primary cosmic rays.” In: *The Astrophysical Journal* 374 (1991), pp. 356–365. DOI: 10.1086/170125.
- [29] F. Gahbauer et al. “A New Measurement of the Intensities of the Heavy Primary Cosmic-Ray Nuclei around 1 TeV amu⁻¹.” In: *The Astrophysical Journal* 607 (2004), pp. 333–341. DOI: 10.1086/383304.
- [30] M. Ave et al. “Composition of Primary Cosmic-Ray Nuclei at High Energies.” In: *The Astrophysical Journal* 678 (2008), p. 262. DOI: 10.1086/529424. arXiv: 0801.0582.
- [31] A. Obermeier et al. “Energy Spectra of Primary and Secondary Cosmic-Ray Nuclei Measured with TRACER.” In: *The Astrophysical Journal* 742 (2011), p. 14. DOI: 10.1088/0004-637X/742/1/14. arXiv: 1108.4838.
- [32] H. S. Ahn et al. “Energy Spectra of Cosmic-ray Nuclei at High Energies.” In: *The Astrophysical Journal* 707 (2009), pp. 593–603. DOI: 10.1088/0004-637X/707/1/593. arXiv: 0911.1889.
- [33] D. Maurin, F. Melot, and R. Taillet. “A database of charged cosmic rays.” In: *Astronomy and Astrophysics* 569 (2014), A32. DOI: 10.1051/0004-6361/201321344. arXiv: 1302.5525.
- [34] H. S. Ahn et al. “Discrepant hardening observed in cosmic-ray elemental spectra.” In: *The Astrophysical Journal* 714 (2010), pp. L89–L93. DOI: 10.1088/2041-8205/714/1/L89. arXiv: 1004.1123.

- [35] A. M. Hillas. “Cosmic Rays: Recent Progress and some Current Questions.” In: *Conference on Cosmology, Galaxy Formation and Astro-Particle Physics on the Pathway to the SKA*. 2006. arXiv: astro-ph/0607109.
- [36] D. Heck et al. “CORSIKA: A Monte Carlo code to simulate extensive air showers.” In: *FZKA-6019* (1998).
- [37] F. Riehn et al. “The hadronic interaction model SIBYLL 2.3c and Feynman scaling.” In: *Proceedings of the 35th International Cosmic Ray Conference*. Vol. ICRC2017. Proceedings of Science, 2017, p. 301. arXiv: 1709.07227.
- [38] C. Patrignani et al. “Review of Particle Physics.” In: *Chinese Physics C40.10* (2016), p. 100001. DOI: 10.1088/1674-1137/40/10/100001.
- [39] A. Fedynitch et al. “Calculation of conventional and prompt lepton fluxes at very high energy.” In: *EPJ Web of Conferences 99* (2015), p. 08001. DOI: 10.1051/epjconf/20159908001. arXiv: 1503.00544.
- [40] J. M. Picone et al. “NRLMSISE-00 empirical model of the atmosphere: Statistical comparisons and scientific issues.” In: *J. of Geophysical Research (Space Phys.) 107* (2002), p. 1468. DOI: 10.1029/2002JA009430.
- [41] M. Honda et al. “Calculation of atmospheric neutrino flux using the interaction model calibrated with atmospheric muon data.” In: *Physical Review D75* (2007), p. 043006. DOI: 10.1103/PhysRevD.75.043006. arXiv: astro-ph/0611418.
- [42] R. Enberg, M. H. Reno, and I. Sarcevic. “Prompt neutrino fluxes from atmospheric charm.” In: *Physical Review D78* (2008), p. 043005. DOI: 10.1103/PhysRevD.78.043005. arXiv: 0806.0418.
- [43] T. K. Gaisser. “Cosmic Ray Energy Spectrum from Measurements of Air Showers.” In: *Frontiers of Physics (Beijing) 8* (2013), pp. 748–758. DOI: 10.1007/s11467-013-0319-7. arXiv: 1303.3565.
- [44] J. R. Hoerandel. “On the knee in the energy spectrum of cosmic rays.” In: *Astroparticle Physics 19* (2003), pp. 193–220. DOI: 10.1016/S0927-6505(02)00198-6. arXiv: astro-ph/0210453.

- [45] S. Ostapchenko. “Monte Carlo treatment of hadronic interactions in enhanced Pomeron scheme: I. QGSJET-II model.” In: *Physical Review D* 83 (2011), p. 014018. DOI: 10.1103/PhysRevD.83.014018. arXiv: 1010.1869.
- [46] S. Roesler, R. Engel, and J. Ranft. “The Monte Carlo event generator DPMJET-III.” In: *Advanced Monte Carlo for radiation physics, particle transport simulation and applications*. 2001, pp. 1033–1038. DOI: 10.1007/978-3-642-18211-2_166. arXiv: hep-ph/0012252.
- [47] M. G. Aartsen et al. “Evidence for High-Energy Extraterrestrial Neutrinos at the IceCube Detector.” In: *Science* 342 (2013), p. 1242856. DOI: 10.1126/science.1242856. arXiv: 1311.5238.
- [48] M. G. Aartsen et al. “Observation of High-Energy Astrophysical Neutrinos in Three Years of IceCube Data.” In: *Physical Review Letters* 113 (2014), p. 101101. DOI: 10.1103/PhysRevLett.113.101101. arXiv: 1405.5303.
- [49] The IceCube Collaboration. “Observation of Astrophysical Neutrinos in Six Years of IceCube Data.” In: *Proceedings of the 35th International Cosmic Ray Conference*. Vol. ICRC2017. Proceedings of Science, 2017, p. 981. arXiv: 1710.01191.
- [50] M. G. Aartsen et al. “Observation and Characterization of a Cosmic Muon Neutrino Flux from the Northern Hemisphere using six years of IceCube data.” In: *The Astrophysical Journal* 833.1 (2016), p. 3. DOI: 10.3847/0004-637X/833/1/3. arXiv: 1607.08006.
- [51] The IceCube Collaboration. “A Measurement of the Diffuse Astrophysical Muon Neutrino Flux Using Eight Years of IceCube Data.” In: *Proceedings of the 35th International Cosmic Ray Conf.* Vol. ICRC2017. Proceedings of Science, 2017, p. 1005. arXiv: 1710.01191.
- [52] M. G. Aartsen et al. “Atmospheric and astrophysical neutrinos above 1 TeV interacting in IceCube.” In: *Physical Rev.* D91.2 (2015), p. 022001. DOI: 10.1103/PhysRevD.91.022001. arXiv: 1410.1749.

- [53] M. G. Aartsen et al. “Search for astrophysical sources of neutrinos using cascade events in IceCube.” In: *The Astrophysical Journal* 846.2 (2017), p. 136. DOI: 10.3847/1538-4357/aa8508. arXiv: 1705.02383.
- [54] M. G. Aartsen et al. “All-sky Search for Time-integrated Neutrino Emission from Astrophysical Sources with 7 yr of IceCube Data.” In: *The Astrophysical Journal* 835.2 (2017), p. 151. DOI: 10.3847/1538-4357/835/2/151. arXiv: 1609.04981.
- [55] M. G. Aartsen et al. “Constraints on Galactic Neutrino Emission with Seven Years of IceCube Data.” In: *The Astrophysical Journal* 849.1 (2017), p. 67. DOI: 10.3847/1538-4357/aa8dfb. arXiv: 1707.03416.
- [56] W. B. Atwood et al. “The Large Area Telescope on the Fermi Gamma-ray Space Telescope Mission.” In: *The Astrophysical Journal* 697 (2009), pp. 1071–1102. DOI: 10.1088/0004-637X/697/2/1071. arXiv: 0902.1089.
- [57] M. Fornasa and M. A. Sánchez-Conde. “The nature of the Diffuse Gamma-Ray Background.” In: *Physics Reports* 598 (2015), pp. 1–58. DOI: 10.1016/j.physrep.2015.09.002. arXiv: 1502.02866.
- [58] A. W. Strong, I. V. Moskalenko, and V. S. Ptuskin. “Cosmic-ray propagation and interactions in the Galaxy.” In: *Annual Review of Nuclear and Particle Science* 57 (2007), pp. 285–327. DOI: 10.1146/annurev.nucl.57.090506.123011. arXiv: astro-ph/0701517.
- [59] S. Veilleux, G. Cecil, and J. Bland-Hawthorn. “Galactic winds.” In: *Annual Review of Astronomy and Astrophysics* 43 (2005), pp. 769–826. DOI: 10.1146/annurev.astro.43.072103.150610. arXiv: astro-ph/0504435.
- [60] S. Recchia, P. Blasi, and G. Morlino. “Cosmic ray driven Galactic winds.” In: *Monthly Notices of the Royal Astronomical Society* 462.4 (2016), pp. 4227–4239. DOI: 10.1093/mnras/stw1966. arXiv: 1603.06746.

- [61] M. Ackermann et al. “Fermi-LAT Observations of the Diffuse Gamma-Ray Emission: Implications for Cosmic Rays and the Interstellar Medium.” In: *The Astrophysical Journal* 750 (2012), p. 3. DOI: 10.1088/0004-637X/750/1/3. arXiv: 1202.4039.
- [62] A. W. Strong and I. V. Moskalenko. “Propagation of cosmic-ray nucleons in the galaxy.” In: *The Astrophysical Journal* 509 (1998), pp. 212–228. DOI: 10.1086/306470. arXiv: astro-ph/9807150.
- [63] E. S. Seo and V. S. Ptuskin. “Stochastic reacceleration of cosmic rays in the interstellar medium.” In: *The Astrophysical Journal* 431 (1994), pp. 705–714. DOI: 10.1086/174520.
- [64] M. K. Verma. “Statistical theory of magnetohydrodynamic turbulence: Recent results.” In: *Physics Reports* 401 (2004), pp. 229–380. DOI: 10.1016/j.physrep.2004.07.007. arXiv: nlin/0404043.
- [65] G. L. Case and D. Bhattacharya. “A new sigma-d relation and its application to the galactic supernova remnant distribution.” In: *The Astrophysical Journal* 504 (1998), p. 761. DOI: 10.1086/306089. arXiv: astro-ph/9807162.
- [66] T. Kamae et al. “Parameterization of Gamma, e^{+/-} and Neutrino Spectra Produced by p-p Interaction in Astronomical Environment.” In: *The Astrophysical Journal* 647 (2006), pp. 692–708. DOI: 10.1086/513602, 10.1086/505189. arXiv: astro-ph/0605581.
- [67] D. Gaggero et al. “Gamma-ray sky points to radial gradients in cosmic-ray transport.” In: *Physical Review D* 91.8 (2015), p. 083012. DOI: 10.1103/PhysRevD.91.083012. arXiv: 1411.7623.
- [68] C. Evoli et al. “Cosmic-Ray Nuclei, Antiprotons and Gamma-rays in the Galaxy: a New Diffusion Model.” In: *Journal of Cosmology and Astroparticle Physics* 0810 (2008), p. 018. DOI: 10.1088/1475-7516/2008/10/018, 10.1088/1475-7516/2016/04/E01. arXiv: 0807.4730.
- [69] C. Evoli et al. “Antiprotons from dark matter annihilation in the Galaxy: astrophysical uncertainties.” In: *Phys. Rev. D* 85 (2012), p. 123511. DOI: 10.1103/PhysRevD.85.123511. arXiv: 1108.0664.

- [70] S. R. Kelner, F. A. Aharonian, and V. V. Bugayov. “Energy spectra of gamma-rays, electrons and neutrinos produced at proton-proton interactions in the very high energy regime.” In: *Physical Review D* 74 (2006), p. 034018. DOI: 10.1103/PhysRevD.74.034018, 10.1103/PhysRevD.79.039901. arXiv: astro-ph/0606058.
- [71] V. Cavasinni, D. Grasso, and L. Maccione. “TeV Neutrinos from Supernova Remnants embedded in Giant Molecular Clouds.” In: *Astroparticle Physics* 26 (2006), pp. 41–49. DOI: 10.1016/j.astropartphys.2006.04.009. arXiv: astro-ph/0604004.
- [72] A. A. Abdo et al. “A Measurement of the Spatial Distribution of Diffuse TeV Gamma Ray Emission from the Galactic Plane with Milagro.” In: *The Astrophysical Journal* 688 (2008), pp. 1078–1083. DOI: 10.1086/592213. arXiv: 0805.0417.
- [73] C. M. Urry and P. Padovani. “Unified schemes for radio-loud active galactic nuclei.” In: *Publications of the Astronomical Society of the Pacific* 107 (1995), p. 803. DOI: 10.1086/133630. arXiv: astro-ph/9506063.
- [74] A. J. Beasley et al. “The VLBA Calibrator Survey-VCS1.” In: *The Astrophysical Journal Supplement Series* 141 (2002), pp. 13–22. DOI: 10.1086/339806. arXiv: astro-ph/0201414.
- [75] J. F. Schachter et al. “Ten new BL Lacertae objects discovered by an efficient X-ray/radio/optical technique.” In: *The Astrophysical Journal* 412 (1993), pp. 541–549. DOI: 10.1086/172942.
- [76] T. Nishiyama et al. “Detection of a new TeV gamma-ray source of BL Lac object 1ES 1959+650.” In: *Proceedings of the 26th International Cosmic Ray Conference*. AIP Conference Proceedings, 2000, pp. 370–373.
- [77] M. K. Daniel et al. “Spectrum of very high energy gamma-rays from the blazar 1ES1959+650 during flaring activity in 2002.” In: *The Astrophysical Journal* 621 (2005), p. 181. DOI: 10.1086/427406. arXiv: astro-ph/0503085.

- [78] P. Padovani and P. Giommi. “The Connection between x-ray and radio-selected BL Lacertae objects.” In: *The Astrophysical J.* 444 (1995), p. 567. DOI: 10.1086/175631. arXiv: astro-ph/9412073.
- [79] P. Giommi et al. “Simultaneous Planck, Swift, and Fermi observations of X-ray and gamma-ray selected blazars.” In: *Astronomy and Astrophysics* 541 (2012), A160. DOI: 10.1051/0004-6361/201117825. arXiv: 1108.1114.
- [80] L. Maraschi, G. Ghisellini, and A. Celotti. “A jet model for the gamma-ray emitting blazar 3C 279.” In: *The Astrophysical Journal* 397 (1992), pp. L5–L9. DOI: 10.1086/186531.
- [81] M. Petropoulou et al. “Photohadronic origin of γ -ray BL Lac emission: implications for IceCube neutrinos.” In: *Monthly Notices of the Royal Astronomical Society* 448.3 (2015), pp. 2412–2429. DOI: 10.1093/mnras/stv179. arXiv: 1501.07115.
- [82] S. Buson et al. “Fermi-LAT, FACT, MAGIC and VERITAS detection of increasing gamma-ray activity from the high-energy peaked BL Lac object 1ES 1959+650.” In: *The Astronomer’s Telegram* 9010 (Apr. 2016).
- [83] A. Biland. “FACT measures increased gamma-ray flux from the high-energy peaked BL Lac object 1ES 1959+650 since five nights.” In: *The Astronomer’s Telegram* 9139 (June 2016).
- [84] A. Biland et al. “Further increase of gamma-ray emission from the HBL 1ES 1959+650.” In: *The Astronomer’s Telegram* 9148 (June 2016).
- [85] A. Biland and R. Mirzoyan. “FACT and MAGIC measure an increased gamma-ray flux from the HBL 1ES 1959+650.” In: *The Astronomer’s Telegram* 9203 (July 2016).
- [86] A. Biland. “FACT measures new maximum flux from the HBL 1ES 1959+650 at TeV energies.” In: *The Astronomer’s Telegram* 9239 (July 2016).

- [87] H. Krawczynski et al. “Multiwavelength observations of strong flares from the TeV - blazar 1ES 1959+650.” In: *The Astrophysical Journal* 601 (2004), pp. 151–164. DOI: 10.1086/380393. arXiv: astro-ph/0310158.
- [88] F. Halzen and D. Hooper. “High energy neutrinos from the TeV blazar 1ES 1959+650.” In: *Astroparticle Physics* 23 (2005), pp. 537–542. DOI: 10.1016/j.astropartphys.2005.03.007. arXiv: astro-ph/0502449.
- [89] H. Anderhub et al. “Design and Operation of FACT – The First G-APD Cherenkov Telescope.” In: *Journal of Instrumentation* 8 (2013), P06008. DOI: 10.1088/1748-0221/8/06/P06008. arXiv: 1304.1710.
- [90] The IceCube Collaboration. *IceCube Digital Optical Module*. Jan. 2018. URL: https://gallery.icecube.wisc.edu/internal/v/graphics/dom/DOMNoHarnessWhiteback_lg.jpg.html?g2_imageViewsIndex=2.
- [91] A. Achterberg et al. “First Year Performance of The IceCube Neutrino Telescope.” In: *Astroparticle Physics* 26 (2006), pp. 155–173. DOI: 10.1016/j.astropartphys.2006.06.007. arXiv: astro-ph/0604450.
- [92] R. Abbasi et al. “IceTop: The surface component of IceCube.” In: *Nuclear Instruments and Methods in Physics Research A* 700 (2013), pp. 188–220. DOI: 10.1016/j.nima.2012.10.067. arXiv: 1207.6326.
- [93] M. G. Aartsen et al. “The IceCube Neutrino Observatory: Instrumentation and Online Systems.” In: *Journal of Instrumentation* 12.03 (2017), P03012. DOI: 10.1088/1748-0221/12/03/P03012. arXiv: 1612.05093.
- [94] T. Benson et al. “IceCube Enhanced Hot Water Drill functional description.” In: *Annals of Glaciology* 55.68 (2014), pp. 105–114. DOI: 10.3189/2014AoG68A032.
- [95] R. Abbasi et al. “Calibration and Characterization of the IceCube Photomultiplier Tube.” In: *Nuclear Instruments and Methods in Physics Research A* 618 (2010), pp. 139–152. DOI: 10.1016/j.nima.2010.03.102. arXiv: 1002.2442.

- [96] R. Abbasi et al. “The Design and Performance of IceCube DeepCore.” In: *Astroparticle Physics* 35 (2012), pp. 615–624. DOI: 10.1016/j.astropartphys.2012.01.004. arXiv: 1109.6096.
- [97] M. G. Aartsen et al. “Measurement of Atmospheric Neutrino Oscillations at 6–56 GeV with IceCube DeepCore.” In: *Physical Review Letters* (2017). arXiv: 1707.07081. Submitted.
- [98] J. A. Formaggio and G. P. Zeller. “From eV to EeV: Neutrino Cross Sections Across Energy Scales.” In: *Reviews of Modern Physics* 84 (2012), pp. 1307–1341. DOI: 10.1103/RevModPhys.84.1307. arXiv: 1305.7513.
- [99] S. L. Glashow. “Resonant Scattering of Antineutrinos.” In: *Physical Review* 118 (1960), pp. 316–317. DOI: 10.1103/PhysRev.118.316.
- [100] A. Cooper-Sarkar, P. Mertsch, and S. Sarkar. “The high energy neutrino cross-section in the Standard Model and its uncertainty.” In: *Journal of High Energy Physics* 08 (2011), p. 042. DOI: 10.1007/JHEP08(2011)042. arXiv: 1106.3723.
- [101] R. Gandhi et al. “Ultrahigh-energy neutrino interactions.” In: *Astroparticle Physics* 5 (1996), pp. 81–110. DOI: 10.1016/0927-6505(96)00008-4. arXiv: hep-ph/9512364.
- [102] E. Bugaev et al. “Propagation of tau neutrinos and tau leptons through the earth and their detection in underwater/ice neutrino telescopes.” In: *Astroparticle Physics* 21 (2004), pp. 491–509. DOI: 10.1016/j.astropartphys.2004.03.002. arXiv: hep-ph/0312295.
- [103] I. M. Frank and I. E. Tamm. “Coherent visible radiation of fast electrons passing through matter.” In: *Comptes Rendus Acad. Sci. URSS* 14.3 (1937), pp. 109–114. DOI: 10.1007/978-3-642-74626-0_2.
- [104] M. G. Aartsen et al. “Measurement of South Pole ice transparency with the IceCube LED calibration system.” In: *Nuclear Instruments and Methods in Physics Research A* 711 (2013), pp. 73–89. DOI: 10.1016/j.nima.2013.01.054. arXiv: 1301.5361.

- [105] The IceCube Col. “Evidence of optical anisotropy of the South Pole ice.” In: *Proceedings of the 33rd International Cosmic Ray Conference*. Vol. 44. 5. Brazilian Journal of Physics, 2014, p. 0580.
- [106] L. G. Henyey and J. L. Greenstein. “Diffuse radiation in the Galaxy.” In: *The Astrophysical Journal* 93 (1941), pp. 70–83. DOI: 10.1086/144246.
- [107] P. Liu. “A new phase function approximating to Mie scattering for radiative transport equations.” In: *Physics in Medicine and Biology* 39.6 (1994), p. 1025. DOI: 10.1088/0031-9155/39/6/008.
- [108] M. G. Aartsen et al. “Energy Reconstruction Methods in the IceCube Neutrino Telescope.” In: *Journal of Instrumentation* 9 (2014), P03009. DOI: 10.1088/1748-0221/9/03/P03009. arXiv: 1311.4767.
- [109] M. G. Aartsen et al. “Observation of the cosmic-ray shadow of the Moon with IceCube.” In: *Phys. Rev. D* 89.10 (2014), p. 102004. DOI: 10.1103/PhysRevD.89.102004. arXiv: 1305.6811.
- [110] M. Ackermann et al. “Optical properties of deep glacial ice at the South Pole.” In: *Journal of Geophysical Research: Atmospheres* 111.D13 (2006), p. D13203. DOI: 10.1029/2005JD006687.
- [111] M. G. Aartsen et al. “IceCube-Gen2: A Vision for the Future of Neutrino Astronomy in Antarctica.” In: *Proceedings, Frontier Research in Astrophysics - II*. Vol. FRAPWS2016. Proceedings of Science, 2017, p. 004. arXiv: 1412.5106.
- [112] The IceCube-Gen2 Collaboration. “The Precision Optical CALibration Module for IceCube-Gen2: First Prototype.” In: *Proceedings of the 35th International Cosmic Ray Conference*. Vol. ICRC2017. Proceedings of Science, 2017, p. 934. arXiv: 1710.01207.
- [113] The IceCube-Gen2 Col. “A Precision Optical Calibration Module for IceCube-Gen2.” In: *Proceedings of the 34th International Cosmic Ray Conference*. Vol. ICRC2015. Proceedings of Science, 2015, p. 1133. arXiv: 1510.05228.

- [114] M. G. Aartsen et al. “Improvement in Fast Particle Track Reconstruction with Robust Statistics.” In: *Nuclear Instruments and Methods in Physics Research A* 736 (2014), pp. 143–149. DOI: 10.1016/j.nima.2013.10.074. arXiv: 1308.5501.
- [115] J. Ahrens et al. “Muon track reconstruction and data selection techniques in AMANDA.” In: *Nuclear Instruments and Methods in Physics Research A* 524 (2004), pp. 169–194. DOI: 10.1016/j.nima.2004.01.065. arXiv: astro-ph/0407044.
- [116] N. van Eijndhoven, O. Fadiran, and G. Japaridze. “Implementation of a Gauss convoluted Pandel PDF for track reconstruction in Neutrino Telescopes.” In: *Astroparticle Physics* 28 (2007), pp. 456–462. DOI: 10.1016/j.astropartphys.2007.09.001. arXiv: 0704.1706.
- [117] J. Lundberg et al. “Light tracking for glaciers and oceans: Scattering and absorption in heterogeneous media with Photonics.” In: *Nuclear Instruments and Methods in Physics Research A* 581 (2007), pp. 619–631. DOI: 10.1016/j.nima.2007.07.143. arXiv: astro-ph/0702108.
- [118] N. Whitehorn, J. van Santen, and S. Lafebre. “Penalized Splines for Smooth Representation of High-dimensional Monte Carlo Datasets.” In: *Computer Physics Communications* 184 (2013), pp. 2214–2220. DOI: 10.1016/j.cpc.2013.04.008. arXiv: 1301.2184.
- [119] R. Abbasi et al. “An improved method for measuring muon energy using the truncated mean of dE/dx .” In: *Nucl. Instrum. Meth.* A703 (2013), pp. 190–198. DOI: 10.1016/j.nima.2012.11.081. arXiv: 1208.3430.
- [120] J. van Santen. “Neutrino Interactions in IceCube above 1 TeV.” Dissertation. UW-Madison, 2014. URL: <http://search.proquest.com/docview/1637727437/abstract/CE0FBEBF172B24F9APQ/1>.
- [121] L. Rädcl. “Measurement of High-Energy Muon Neutrinos with the Ice-Cube Neutrino Observatory.” Dissertation. RWTH Aachen University, 2017. DOI: 10.18154/RWTH-2017-10054.

- [122] S. Schönert et al. “Vetoing atmospheric neutrinos in a high energy neutrino telescope.” In: *Physical Review D* 79 (2009), p. 043009. DOI: 10.1103/PhysRevD.79.043009. arXiv: 0812.4308.
- [123] T. K. Gaisser et al. “Generalized self-veto probability for atmospheric neutrinos.” In: *Physical Review D* 90.2 (2014), p. 023009. DOI: 10.1103/PhysRevD.90.023009. arXiv: 1405.0525.
- [124] The IceCube Collaboration. “All-flavor Multi-Channel Analysis of the Astrophysical Neutrino Spectrum with IceCube.” In: *Proceedings of the 35th International Cosmic Ray Conference*. Vol. ICRC2017. Proceedings of Science, 2017, p. 976. arXiv: 1710.01207.
- [125] K. M. Gorski et al. “HEALPix - A Framework for high resolution discretization, and fast analysis of data distributed on the sphere.” In: *The Astrophysical Journal* 622 (2005), pp. 759–771. DOI: 10.1086/427976. arXiv: astro-ph/0409513.
- [126] The IceCube Collaboration. “Improved methods for solar Dark Matter searches with the IceCube neutrino telescope.” In: *Proceedings of the 34th International Cosmic Ray Conference*. Vol. ICRC2015. Proceedings of Science, 2015, p. 1099. arXiv: 1510.05226.
- [127] F. Pedregosa et al. “Scikit-learn: Machine Learning in Python.” In: *Journal of Machine Learning Research* 12 (2011), pp. 2825–2830.
- [128] Richard H. B. et al. “A Limited Memory Algorithm for Bound Constrained Optimization.” In: *SIAM Journal on Scientific Computing* 16.5 (1995), pp. 1190–1208. DOI: 10.1137/0916069.
- [129] A. Gazizov and M. P. Kowalski. “ANIS: High energy neutrino generator for neutrino telescopes.” In: *Computer Physics Communications* 172 (2005), pp. 203–213. DOI: 10.1016/j.cpc.2005.03.113. arXiv: astro-ph/0406439.
- [130] G. Cowan et al. “Asymptotic formulae for likelihood-based tests of new physics.” In: *The European Physical Journal C* 71 (2011), p. 1554. DOI: 10.1140/epjc/s10052-011-1554-0, 10.1140/epjc/s10052-013-2501-z. arXiv: 1007.1727.

- [131] M. G. Aartsen et al. “A combined maximum-likelihood analysis of the high-energy astrophysical neutrino flux measured with IceCube.” In: *The Astrophysical Journal* 809.1 (2015), p. 98. DOI: 10.1088/0004-637X/809/1/98. arXiv: 1507.03991.
- [132] The IceCube, FACT, and MAGIC Collaborations. “IceCube Search for Neutrinos from 1ES 1959+650: Completing the Picture.” In: *Proceedings of the 35th International Cosmic Ray Conference*. Vol. ICRC2017. Proceedings of Science, 2017, p. 969. arXiv: 1710.01179.
- [133] M. G. Aartsen et al. “Search for Prompt Neutrino Emission from Gamma-Ray Bursts with IceCube.” In: *The Astrophysical Journal* 805.1 (2015), p. L5. DOI: 10.1088/2041-8205/805/1/L5. arXiv: 1412.6510.
- [134] S. Coenders. “High-energy cosmic ray accelerators: searches with IceCube neutrinos.” Dissertation. Technische Universität München, 2016. URL: <https://mediatum.ub.tum.de/1327578>.
- [135] T. Neunhoffer. “Estimating the angular resolution of tracks in neutrino telescopes based on a likelihood analysis.” In: *Astroparticle Physics* 25 (2006), pp. 220–225. DOI: 10.1016/j.astropartphys.2006.01.002. arXiv: astro-ph/0403367.
- [136] A. Albert et al. “New constraints on all flavor Galactic diffuse neutrino emission with the ANTARES telescope.” In: *Physical Review D* 96.6 (2017), p. 062001. DOI: 10.1103/PhysRevD.96.062001. arXiv: 1705.00497.
- [137] C. Righi, F. Tavecchio, and D. Guetta. “High-energy emitting BL Lacs and high-energy neutrinos - Prospects for the direct association with IceCube and KM3NeT.” In: *Astronomy and Astrophysics* 598 (2017), A36. DOI: 10.1051/0004-6361/201629412. arXiv: 1607.08061.
- [138] M. G. Aartsen et al. “The IceCube Realtime Alert System.” In: *Astropart. Phys.* 92 (2017), pp. 30–41. DOI: 10.1016/j.astropartphys.2017.05.002. arXiv: 1612.06028.

- [139] S. Agostinelli et al. “GEANT4: A Simulation toolkit.” In: *Nuclear Instruments and Methods in Physics Research A* 506 (2003), pp. 250–303.
DOI: 10.1016/S0168-9002(03)01368-8.